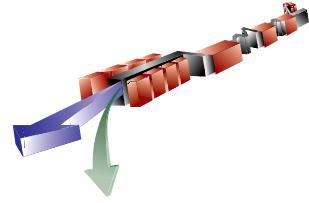


8

Undulator



TECHNICAL SYNOPSIS

The LCLS Undulator is made up of 33 individual undulator segments. Each undulator segment will be a permanent-magnet planar hybrid device with a period length of 30 mm and a fixed gap of nominally 6 mm. The actual gap will be adjusted as necessary to yield an effective K of 3.71. Each undulator segment is 3.42 m long, with 226 poles per jaw. The poles will be made of vanadium permendur and the magnets of a grade of NdFeB with a high intrinsic coercivity for better resistance to radiation-induced demagnetization. The electron beam will be focused by a separated function FODO lattice, using permanent-magnet quadrupoles placed between the undulator segments. These focusing or defocusing lenses will share the drift spaces between the undulator segments with electron beam position monitors and steering magnets. The drift space after every third undulator segment will be longer to provide space for x-ray diagnostics. Although the standard short drift space will be 187 mm long and the standard long one 421 mm long, the lengths of the first three drift spaces will be modified slightly to reduce the overall saturation length. The electron beam trajectory is required to be straight to within a few microns over a distance of ~ 10 m to achieve adequate overlap of the electron and photon beams. It is shown that this specification, although presently beyond state-of-the-art mechanically, can be achieved with beam-based techniques.

A detailed magnetic design for the undulator segments is given, and a mechanical scheme for holding the magnets and poles with the necessary rigidity is presented. Provision has been made for magnetic tuning of the undulator segments by allowing small, few-period long adjustments to the magnetic gap, and by providing for side shims. In addition, adjustment of the gap at the ends of the undulator segments will be possible on a sub-micron level in order to adjust the phasing between the undulator segments. Tolerances have been developed that will set the magnetic tuning requirements for the individual undulator segments.

The smoothness requirement for the inside surface of the vacuum chamber is analyzed, and found to be achievable. Ions produced by passing electron or x-ray beams can have a deleterious effect on the electron bunch, but, at the design vacuum level, the effect of the ion production is not significant.

Diagnostics for the electron beam will include beam position monitors and Cherenkov detectors after each undulator segment, optical transition radiation imaging after every 3rd undulator segment, and wire scanners and current monitors at the ends of the undulator line.

8.1 Overview

8.1.1 Introduction

In a single pass FEL (free electron laser) operating in the SASE (self-amplified spontaneous emission) regime, exponential gain of the coherent radiation intensity and saturation after about twenty power gain lengths are predicted by theory (see **Chapter 4**). An FEL operating at saturation will have a more stable radiation output. Therefore, a goal in the design of the undulator line is to allow saturation to be reached while minimizing the required undulator length. Minimizing the undulator length helped guide many of the parameter choices for the undulator line and was also used in allocating error tolerances. Sufficient diagnostics must be included between undulator segments to effectively and conveniently monitor the electron and x-ray beams along the length of the undulator line. These diagnostics will be used as an aid in electron beam tuning, to identify problems, to monitor the intensity gain in the x-ray beam, and to confirm that saturation has been achieved.

The basis for choice of parameters for the undulator line is explained in **Section 8.2**. A tolerance budget for trajectory straightness through the undulator segments, phase errors, and positioning errors is also given in that section. **Section 8.3** gives requirements for the magnetic measurement of the undulator segments. Considerations to be used in the measurement and sorting of the magnet blocks for the undulator segments are given in **Section 8.4**. Considerations in the choice of the grade of NdFeB magnets are explained in **Section 8.5.1**, and a magnetic design is given in **Section 8.5.2**, along with results from the magnetic modeling calculations. Some considerations of the end tuning for the undulator segments are given in **Section 8.5.3**. **Section 8.6** shows the mechanical design for the undulator segments, including the scheme for holding the magnets and poles (see **Section 8.6.1**), the provisions included for magnetic tuning, both through the main part of the undulator segment and through the ends (see **Section 8.6.2**), the supports for the undulator segments that also provide for overall position adjustment (see **Section 8.6.3**), and the impact of temperature changes on the undulator segments (see **Section 8.6.4**). The design for the permanent magnet quadrupoles is given in **Section 8.7**. The effect of missteering of the electron beam so that it strikes the vacuum chamber and subsequently the undulator segments, and the possibility of using collimators are considered in **Section 8.8.1**, along with possibilities for reducing the roughness of the inside of the vacuum chamber. A description of the vacuum system is in **Section 8.8.2**, pumping and outgassing considerations are given in **Section 8.8.3**, and thermal considerations are in **Section 8.8.4**. **Section 8.9** discusses wakefield sources in the undulator vacuum chamber. **Section 8.9.5** considers the effect of the roughness of the inside surface of the vacuum chamber on the wakefields and concludes that the smoothness requirements can be met. **Section 8.10** considers the means by which ions could be produced and the effect that those ions could have on the beam, concluding that the necessary vacuum is readily achievable. The electron beam diagnostics include pickup electrode beam position monitors, Cherenkov detectors, optical transition radiation imagers, wire scanners, and current monitors, as described in **Section 8.11**. **Section 8.12** describes the beam-based alignment scheme, including

the results of simulations. Finally, **Section 8.13** describes the x-ray diagnostics that will be located after every third undulator segment.

8.1.2 Undulator Line Design Summary

The Linac Coherent Light Source (LCLS) undulator line will consist of 33 undulator segments separated by breaks of various lengths. The undulator segments are 3.4-m-long permanent-magnet planar hybrid arrays with a period of 30 mm and a magnetic gap of 6 mm. The maximum outside dimension of the vacuum chamber is 5.6 mm. Focusing quadrupoles, in a FODO lattice, and electron beam diagnostics will be located in the breaks between undulator segments. Every third break will be longer in order to also accommodate x-ray diagnostics. Thus, taking the alternating focusing and defocusing quadrupoles into account, the ‘super-period’ length before the undulator line repeats itself is six undulator segments. The first three break lengths will be different from those in the main part of the undulator line, however, because small modifications there help reduce the overall undulator length needed for saturation.

Other options for the undulator segments were considered, such as bifilar helical electromagnetic devices using either superconducting DC coils or warm pulsed coils. These were rejected because they were shown to be costly, complicated, difficult to hold to mechanical tolerances, and difficult to provide with steering corrections. Also, access to the beam pipe would be impaired because it would be completely surrounded by the undulator segments. A significant amount of R&D would be required to make a superconducting magnet design work. In contrast, planar hybrid technology is well established, and the requirements for the undulator segments, while demanding, have been met in existing devices. These arguments led to the choice of the planar hybrid design.

The electron beam beta function and the undulator period were selected to minimize the saturation length. The FEL simulation code RON [1, 2] has been used to optimize parameters such as the length of the undulator segments and the break lengths between them. Tolerances for individual undulator segments have also been determined.

The quadrupole focusing magnets are made using permanent magnets. No provision is planned for adjusting the strength of the quadrupole, so magnetic tuning and adjustment of the integrated quadrupole gradient will be done during the manufacture of the quadrupole, before it is installed. The strength of the quadrupoles will not be adjusted over the proposed operating range of the LCLS electron beam energy. Instead, the beam parameters at the entrance to the undulator line will be adjusted for proper matching.

In addition to focusing, the quadrupole magnets between the undulator segments serve two other functions: they will be used in the initial alignment to establish a straight-line trajectory and they will be moved mechanically on vertical and horizontal slides to correct the trajectory to approximate a straight line.

8.2 Theory and Tolerances for the Undulator

8.2.1 Design of Undulator Segments

8.2.1.1 Basic Considerations

One possibility for creating an x-ray FEL is to use the SASE scheme. This scheme involves only two elements: an undulator and the electron beam propagating through the undulator. The electron beam is unstable in that it bunches at the wavelength of the fundamental harmonic of the spontaneous undulator radiation. When the bunching is small, the system is linear, so the Fourier harmonics of the beam current at this frequency grow exponentially with distance traveled through the undulator. The power gain length is the characteristic length where the squared magnitude of the fundamental Fourier harmonic increases by a factor of e . At some distance from the beginning of the undulator, the electron beam has become significantly bunched and there is no further growth; this distance is the saturation length. The coherent undulator radiation produced by the bunched beam is the output of the FEL. An advantage of this FEL scheme is the absence of mirrors, which are a serious problem for x-ray wavelengths. A disadvantage is that the radiation spectrum is relatively wide. From the point of view of building such a device, the main problems are obtaining a high-current low-emittance low-energy-spread electron beam to keep the saturation length within reasonable limits (i.e., not much over 100 meters) and to meet the tight tolerances for field errors, misalignments and steering errors of the undulator.

Typically the saturation length is about 20 times the power gain length. For an FEL that is barely (or not) long enough to saturate, nearly all the output light comes from the end of the undulator line. Most of the line, therefore, is devoted to bunching the electron beam by linearly amplifying the initial electron density fluctuations. Therefore, the goal in optimizing this part of the undulator line is to minimize the power gain length.

8.2.2 Optimal Period and Focusing

The main parameters of the LCLS project are listed in **Table 8.1** and in **Appendix A**. In **Figure 8.1** and **Figure 8.2** the dependence of the saturation length on the undulator period and matched beta function for the planar permanent magnet undulator is shown. This dependence was obtained using the formulas of Halbach [3] and **Ref.** [4] and takes into account both the energy spread due to quantum excitation and the undulator "filling factor" (the fraction of the undulator occupied by undulator segments rather than by the breaks between them).

Table 8.1 Parameters of the LCLS project.

Parameter	Value
Radiation wavelength	1.5 Å
Beam energy	14.35 GeV
Normalized slice emittance	1.2 mm-mrad
Beam peak current	3.4 kA
Slice energy spread (standard deviation)	1.4 MeV
Focusing	FODO
Undulator period	30 mm
Undulator parameter K	3.71
Undulator effective peak on-axis field	1.3250 Tesla
Nominal magnetic gap	6 mm
Undulator segment length	3.420 m
Break length (short)	0.187 m
Break length (long)	0.421 m
Supercell length (6 undulator segments)	22.110 m
Number of undulator segments	33

Figure 8.1 and **Figure 8.2** show that the design values of 3 cm for the undulator period and 18 m for the beta function are close to optimal at the 14.35 GeV energy-end of the operational range. For lower energy spread and emittance, the optimal undulator period decreases.

The calculation above assumes a planar permanent magnet undulator. Calculations were also done for a superconducting helical undulator. For a period of 2.4 cm, a field of 1.3 T, and with other parameters the same as for the planar permanent magnet option, the saturation length is about 50 m. Although this saturation length is shorter than for a planar undulator, there remain some as yet untested aspects to the mechanical design of a superconducting helical device. Since planar permanent magnet undulator segments are an established technology, they will be used for the LCLS project.

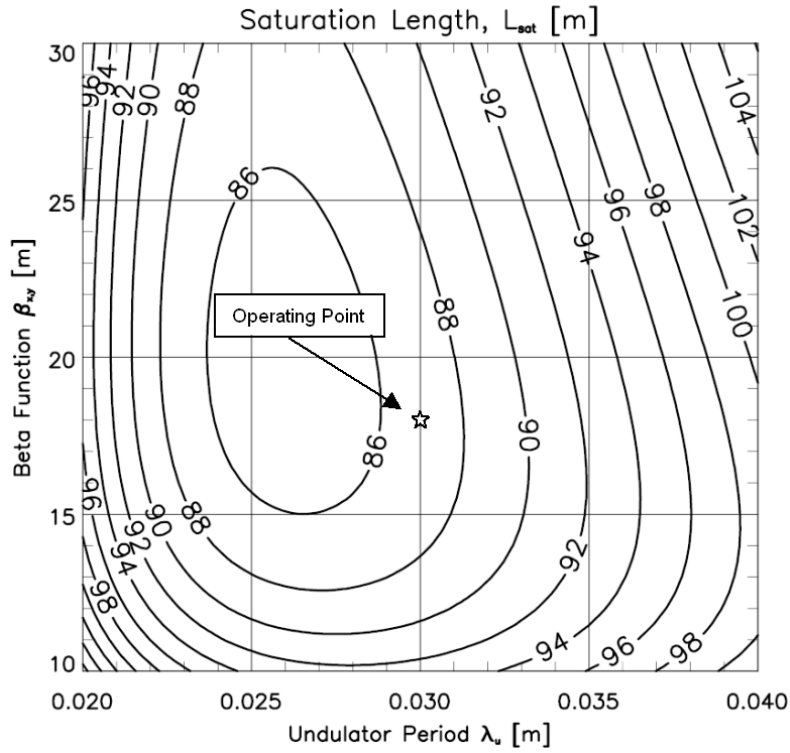


Figure 8.1 Contours of constant saturation length. While the wavelength of the light produced is always 1.5 Å, the magnetic field strength in the undulator is adjusted with the undulator period length according to Halbach's formula [3], and the energy of the electron beam is changed as needed to preserve the wavelength of the light. All numbers are in meters.

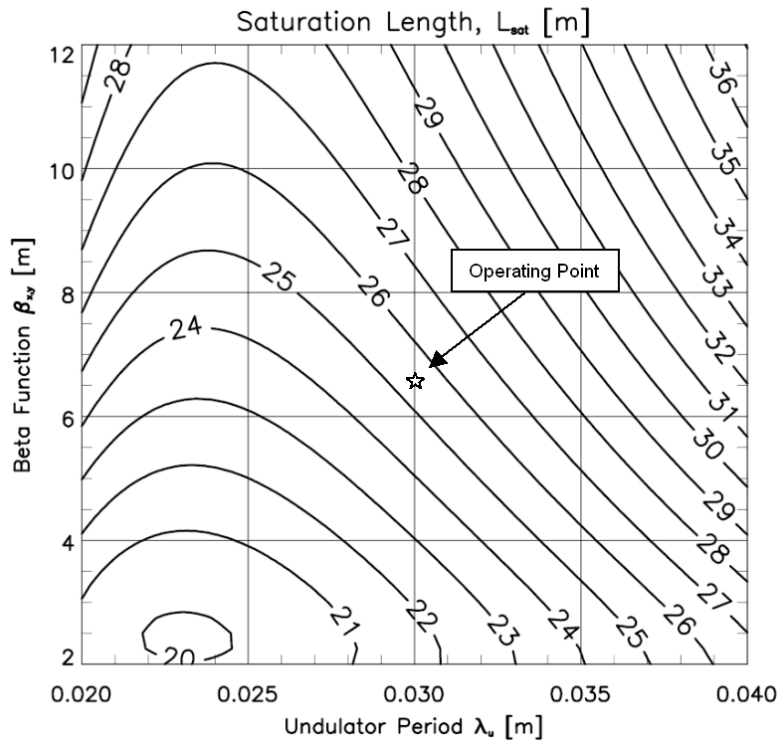


Figure 8.2 Same as Figure 8.1 expect that the wavelength is 15 Å.

8.2.3 Irregularities and Imperfections

The linear theory of high gain is well developed now (see, for example, [5]). Nevertheless, the design of a real magnetic system for a short-wavelength high-gain FEL requires consideration of an inhomogeneous magnetic system with focusing quadrupoles inserted into the breaks between undulator segments. Field, steering, and alignment errors must be considered. The linear time-independent code RON [1,2] was written for the optimization of such magnetic systems. It has been cross-checked with 3D codes such as GINGER and GENESIS and was used successfully for the design optimization of the Argonne FEL [6]. This code has now also been used for the optimization of the LCLS undulator line.

The simplest way to provide proper focusing is to use a FODO lattice, and this choice has been made for the LCLS project. The magnetic system of the undulator will consist of undulator segments with breaks between the segments where quadrupoles and beam position monitors will be installed. After every third undulator segment, the break will be longer so that photon diagnostics can be installed as well. This layout is geometrically similar to the existing APS FEL except that the photon diagnostics are only after every third undulator segment. Another lattice based on quadrupole triplets between undulator segments was considered and rejected because of very tight tolerances for the relative alignment of the three-quadrupole centers.

The following parameter choices were made, based on the results of RON [1,2] calculations:

- The optimal undulator segment length was found to be near 3.4 m. For shorter lengths, the "filling factor" is less, making the effective power gain length longer. (This assumes that the break length is kept at about 0.2 m, which is required for the quadrupoles.) For longer lengths, the power gain length at a beam energy of 4.5 GeV increases due to the larger variation of the beta function within the undulator. The longer lengths are also more difficult mechanically, given the demanding tolerances.
- The optimal average value for the beta function was found to be 18 m. The focal lengths of the quadrupoles are chosen accordingly.
- The break lengths between undulator segments were optimized by calculating the corrections to the "resonance" break length due to the effect of finite emittance and diffraction.
- An option that included magnetic bunchers between the undulator segments was considered and optimized. No significant improvement was found, so no magnetic bunchers are included in the undulator line design.
- The effect of the residual trajectory errors after simulated beam-based alignment [7] was calculated for the optimized undulator. The increase of the saturation length was found to be less than 5 m.

- The effect of the spread of deflection parameters K in different undulator segments was simulated. This way the corresponding tolerances were found.

8.2.4 Tolerances for Undulator Segments

The aim of our optimization is to minimize the power gain length and consequently the saturation length. There are tens of significant parameters in the system, and a deviation in any of these parameters will increase the power gain length. A tolerance budget was worked out for the various parameters so that the overall power gain length increase does not exceed 3%, which corresponds to a 4-m increase in saturation length. Tolerances were set assuming simultaneous worst cases for all parameters. The overall tolerances for the undulator line were used to determine tolerances for a single undulator segment.

The following requirements for the undulator segment field errors were developed. (The derivation is described in the next section.)

- The trajectory walk-off from a straight line must not exceed 2 microns in one segment. The beam-based alignment technique will minimize deviations in the transverse beam coordinates near the beam position monitors (BPMs) between the undulator segments, so the trajectory walk-offs $x(z)$ and $y(z)$ with zero initial (at the upstream BPM) and final (at the downstream BPM) coordinates have to be specified:

$$x(z) = \frac{1}{\gamma} \int_0^z I_{1x}(z') dz', \quad y(z) = \frac{1}{\gamma} \int_0^z I_{1y}(z') dz', \quad (8.1)$$

$$I_{1x}(z) = \frac{e}{mc^2} \left[\int_0^z B_x(z') dz' - \frac{1}{L} \int_0^L \int_0^{z'} B_x(z'') dz'' dz' \right] \quad (8.2)$$

$$I_{1y}(z) = \frac{e}{mc^2} \left[\int_0^z B_y(z') dz' - \frac{1}{L} \int_0^L \int_0^{z'} B_y(z'') dz'' dz' \right] \quad (8.3)$$

where γ is the relativistic factor, e and m are electron charge and mass, c is the velocity of light, B_x and B_y are the measured transverse components of magnetic field, and L is the cell length (the distance between BPMs). The 2-micron deviations in both the x and y directions give an increase in the power gain length of less than 0.2%, and can be achieved with present magnetic measurement and tuning techniques.

- The reduction in spectral intensity of the zero-angle radiation must not exceed 4%. The spectral intensity of the zero-angle radiation is

$$\frac{e^2 k^2 |A|^2}{2\pi c \gamma^2} \quad (8.4)$$

where k is the fundamental harmonic wavevector of the undulator radiation, and

$$A = \int_0^L I_{1y}(z) e^{-i \frac{k}{2\gamma^2} \left[z + \int_0^z I_{1x}^2(z') dz' + \int_0^z I_{1y}^2(z') dz' \right]} dz \quad (8.5)$$

The “reduction” is as compared with an ideal undulator, but in practice the comparison can be with the best undulator, i.e., the one which gives the highest value of $|A|$. A 4% intensity reduction corresponds to an increase in the power gain length by 1.1%.

- The calculated electron phase deviation from the design value must be less than 10° in one segment. This phase is simply the electron-wave slippage:

$$\varphi = \frac{k}{2\gamma^2} \left[L + \int_0^L I_{1x}^2(z) dz + \int_0^L I_{1y}^2(z) dz \right] \quad (8.6)$$

and the “design value” is an integer multiple of 2π . A 10° phase error causes an increase in power gain length of 1.7%.

- The undulator median plane must be defined (and after that aligned) with an accuracy better than 50 microns vertically. If the beam is off-axis vertically by 50 microns, the beam will see a stronger undulator field, resulting in about 10° of additional phase slippage.

Implicit in these tolerances is the need for the magnetic field strength to be uniform along the length of the undulator line. If the magnetic field in one undulator segment is wrong by $\Delta B/B = 1.5 \times 10^{-4}$, the resulting phase error will be 10° . This tolerance agrees with the result from independent simulations performed using the code RON [2] to vary the strength of one undulator segment. Then the change in the overall gain became significant when segment-to-segment variations reached $\Delta B/B = 1.3 \times 10^{-4}$. This translates into an error in the magnetic field strength of 1.7 G, or an error in the undulator segment magnetic gap by 1.2 μm .

8.2.5 Derivation of the Tolerances for the X-Ray FEL

The following is based on a simple picture of acceleration (or deceleration) of the electron by the given radiation eigenmode.

8.2.5.1 Derivation of Basic Equations

According to the Floquet theorem, the wave field eigenmode in the periodic amplifying system can be represented as:

$$E_x = \Re \left[u(x, y, z) e^{pz} e^{ik(z-ct)} \right] \quad (8.7)$$

where $u(x, y, z+L) = u(x, y, z)$, L is the system period, k is the design value of the undulator radiation fundamental harmonic wavevector, and p is the complex growth rate. Then the electron longitudinal motion equations are:

$$\begin{aligned}\frac{dE}{dz} &= eE_x \frac{dx}{dz} \\ \frac{dt}{dz} &= \frac{1}{v_z}\end{aligned}\tag{8.8}$$

where e and $E = \gamma mc^2$ are the electron charge and energy, t is the moment of time when the electron passes the longitudinal coordinate z , and the electron velocity v_z can be expressed through the electron energy and angles:

$$\frac{1}{v_z} \approx \frac{1}{c} \left[1 + \frac{1}{2\gamma^2} + \frac{1}{2} \left(\frac{dx}{dz} \right)^2 + \frac{1}{2} \left(\frac{dy}{dz} \right)^2 \right]\tag{8.9}$$

The angles $dx/dz = \alpha$ and dy/dz can be calculated from the measured magnetic field \mathbf{B} using the trajectory equations:

$$\begin{aligned}\frac{d}{dz} \left(\frac{dx}{dz} \right) &= -\frac{e}{\gamma mc^2} B_y(z) \\ \frac{d}{dz} \left(\frac{dy}{dz} \right) &= \frac{e}{\gamma mc^2} B_x(z)\end{aligned}\tag{8.10}$$

The LCLS undulator line includes beam position monitors and angle steering at the section ends. For ideal steering, the trajectory displacement at the segment ends is zero for the equilibrium (beam centroid) trajectory. Therefore, for the undulator specification, the solution of **Eq. (8.10)** with $x(0) = x(L) = y(0) = y(L) = 0$ is chosen. It is convenient to introduce the corresponding ‘‘corrected’’ dimensionless first field integrals $I_{1x} = -\gamma dx/dz$ and $I_{1y} = \gamma dy/dz$:

$$I_{1x}(z) = \frac{e}{mc^2} \left[\int_0^z B_x(z') dz' - \frac{1}{L} \int_0^z \int_0^{z'} B_x(z'') dz'' dz' \right]\tag{8.11}$$

$$I_{1y}(z) = \frac{e}{mc^2} \left[\int_0^z B_y(z') dz' - \frac{1}{L} \int_0^z \int_0^{z'} B_y(z'') dz'' dz' \right]\tag{8.12}$$

The maximum particle energy variation

$$\Delta E = e \int_0^z E_x [x, y, z', t(z')] \frac{dx}{dz}(z') dz' \quad (8.13)$$

is proportional to

$$|F| = \left| \int_0^z I_{1x}(z') e^{-i\kappa \left[z' + \int_0^{z'} I_{1x}^2(z'') dz'' + \int_0^{z'} I_{1y}^2(z'') dz'' \right]} u[x(z'), y(z'), z'] e^{pz'} dz' \right| \quad (8.14)$$

where $\kappa = k/(2\gamma^2)$. For the LCLS the breaks between undulator segments are relatively short and produce a phase shift of an integer multiple of the x-ray wavelength. Therefore it is close to the homogeneous undulator case, described analytically in Ref. [8]. Then the fundamental eigenmode is close to the Gaussian beam with almost flat wavefronts

$$u \propto e^{-\frac{x^2+y^2}{2\sigma_r^2}} \quad (8.15)$$

The relative reduction of the maximum energy gain caused by different field imperfections is calculated using **Eq. (8.14)** and F is expanded near the “ideal” state, by different kinds of “imperfections”.

8.2.5.2 Trajectory Straightness

Using **Eq. (8.15)** at $z = NL$ at the end of the N^{th} undulator segment, one can expand F in x and y :

$$|F| \approx \left\{ \int_0^{NL} I_{1x}(z) e^{-i\kappa \left[z + \int_0^z I_{1x}^2(z') dz' + \int_0^z I_{1y}^2(z') dz' \right]} e^{pz} dz \right\}_0 - \quad (8.16)$$

$$\frac{1}{2\sigma_r^2} \int_0^{NL} I_{1x}(z) e^{-i\kappa \left[z + \int_0^z I_{1x}^2(z') dz' + \int_0^z I_{1y}^2(z') dz' \right]} e^{pz} [x^2(z) + y^2(z)] dz$$

For the “ideal” case (the curly brackets in **Eq. (8.16)**), the slow part of the expression under the integral is almost constant. Therefore, **Eq. (8.16)** leads to

$$\frac{F - F_0}{F_0} \approx -\frac{\langle x^2 \rangle + \langle y^2 \rangle}{2\sigma_r^2}, \quad (8.17)$$

where the averaging takes place over the length NL , and can be replaced by averaging over each undulator segment, i.e.,

$$\begin{aligned}\langle x^2 \rangle &= \frac{1}{L\gamma^2} \int_0^L \left[\int_0^z I_{1x}(z') dz' \right]^2 dz, \\ \langle y^2 \rangle &= \frac{1}{L\gamma^2} \int_0^L \left[\int_0^z I_{1y}(z') dz' \right]^2 dz.\end{aligned}\tag{8.18}$$

8.2.5.3 Phase Errors

Now suppose that $\langle x \rangle = y = 0$ (so $u = 1$) and F can be represented as the sum of contributions of N undulator segments:

$$F = \int_0^{NL} I_{1x}(z) e^{-ik \left[z + \int_0^z I_{1x}^2(z') dz' + \int_0^z I_{1y}^2(z') dz' \right]} e^{pz} dz \approx \sum_{m=1}^N A_m e^{-i \sum_{s=1}^{m-1} \varphi_s} e^{pL \left(m - \frac{1}{2} \right)},\tag{8.19}$$

where

$$A_m = \int_0^L I_{1x}(z) e^{-ik \left[z + \int_0^z I_{1x}^2(z') dz' + \int_0^z I_{1y}^2(z') dz' \right]} dz,\tag{8.20}$$

$$\varphi_m = \kappa \left[L + \int_0^L I_{1x}^2(z) dz + \int_0^L I_{1y}^2(z) dz \right],\tag{8.21}$$

and the first field integrals in Eqs. 8.2-14 and 8.2-15 are calculated for the undulator segment number m . A is the dimensionless amplitude of the spontaneous undulator radiation in the forward direction for one undulator segment. For the ‘‘ideal’’ case all $A_m = A_0$ are equal and $\varphi_m - Im(pL) = 2\pi q$ (q is an integer). Then

$$F_0 = A_0 \frac{e^{\Re(pLN)} - 1}{e^{\Re(pL)} - 1} e^{\frac{1}{2} pL}.\tag{8.22}$$

For ideal phasing, $\varphi_m = 2\pi q - Im(pL)$ (one can do it by the proper adjustment of the field at the undulator segment ends), and **Eq. (8.19)** gives:

$$\begin{aligned}
 |F|^2 &= \sum_{m=1}^N \sum_{n=1}^N A_m A_n^* e^{\Re(p)(m+n-1)L} \\
 &\approx \sum_{m=1}^N \sum_{n=1}^N \left[|A_0|^2 + A_0 (A_n^* - A_0^*) + A_0^* (A_m - A_0) \right] e^{\Re(p)(m+n-1)L} \\
 &\approx |F_0|^2 + 2|A_0|^2 \operatorname{Re} \left[\frac{e^{\Re(pLN)} - 1}{e^{\Re(pL)} - 1} \sum_{n=1}^N \frac{A_n - A_0}{A_0} e^{\Re(p)Ln} \right] \\
 &= |F_0|^2 \left(1 + 2 \left\langle \Re \left(\frac{A_m - A_0}{A_0} \right) \right\rangle \right).
 \end{aligned} \tag{8.23}$$

For $A_m = A_0$ but non-ideal phases,

$$\begin{aligned}
 |F|^2 &= |A_0|^2 \sum_{m=1}^N \sum_{n=1}^N e^{-i \sum_{s=1}^{m-1} \varphi_s + i \sum_{s=1}^{n-1} \varphi_s} e^{\Re(p)(m+n-1)L} \\
 &\approx |F_0|^2 - |A_0|^2 \sum_{m=1}^N \sum_{n=1}^{m-1} \left(\sum_{s=n}^{m-1} \varphi_s \right)^2 e^{\Re(p)(m+n-1)L}
 \end{aligned} \tag{8.24}$$

For the average case of uncorrelated undulator phase advances, one can estimate the sum in **Eq. (8.24)** as:

$$|F|^2 \approx |F_0|^2 \left[1 - \frac{1}{2 \sinh(\Re(pL))} \langle \varphi_m^2 \rangle \right]. \tag{8.25}$$

But, for the worst case it gives:

$$\left(|F|^2 \right)_{\min} \approx |F_0|^2 \left[1 - \frac{1}{2 \sinh(\Re(pL)) \tanh(\Re(pL)/2)} (\varphi_m^2)_{\max} \right]. \tag{8.26}$$

Let φ_m be distributed homogeneously over the interval $(-\varphi_{m|\max}, \varphi_{m|\max})$. Then $\langle \varphi_m^2 \rangle = (\varphi_{m|\max})^2/3$, and, with 92% probability

$$\left(|\varphi_{m|\max}|^2 \right) / \left[2 \sinh(\Re(pL)) \right] \tag{8.27}$$

is the upper limit for the correction in **Eq. (8.24)**.

8.2.5.4 Resulting Power Gain Length Increase.

Gathering the results of Eqs. (8.17), (8.23), and (8.24),

$$\frac{|F| - |F_0|}{|F_0|} > -\frac{\langle x^2 \rangle + \langle y^2 \rangle}{2\sigma_r^2} + \left\langle \Re \left(\frac{A_m - A_0}{A_0} \right) \right\rangle - \frac{L_g}{2L} |\varphi_m|_{\max}^2, \quad (8.28)$$

where $L_g = 1/[2\text{Re}(p)]$ is the power gain length.

This reduction of the wave-electron interaction efficiency can be expressed as an effective reduction of the undulator parameter K for the ideal magnetic system:

$$\frac{K - K_0}{K_0} > -\frac{\langle x^2 \rangle + \langle y^2 \rangle}{2\sigma_r^2} + \left\langle \Re \frac{A_m - A_0}{A_0} \right\rangle - \frac{L_g}{2L} |\varphi_m|_{\max}^2. \quad (8.29)$$

Now one can use analytical theory [8] or computer code to calculate the corresponding increase of the power gain length. For the LCLS magnetic system, a 3% increase in power gain length corresponds to a 5.4% reduction in K . Taking $\sigma_r^2 \approx \epsilon\beta$ [8], one can make the tolerance budget.

8.3 Undulator Measurement and Tuning

8.3.1 Requirements for the LCLS

The main tolerance requirements for alignment and field quality within a section of the undulator line that includes an undulator segment and a quadrupole are given in **Table 8.2**.

Table 8.2 Alignment tolerances for undulator segment

Alignment Tolerance	Value
Horizontal and vertical trajectory excursion	2 μm
“Radiation amplitude” deviation (see Eq., (8.5))	2 %
Phase slip between two undulator segments	10 degrees
Vertical positioning error	50 μm

These tolerances correspond to approximately 3 % growth of the power gain length. They are demanding, but achievable. They have already been met by the undulator segments that were tuned magnetically for installation in the APS FEL. Those undulator segments have a period length of 33 mm, close enough to the 30 mm period length of the LCLS undulator segments that the tuning techniques developed for the APS undulator segments should transfer directly.

8.3.2 APS Magnetic Measurement Facility

In order to meet these requirements, the APS magnetic measurement facility is equipped with a 6-m-long granite bench for Hall probe and moving coil measurements and a flipping coil system for first and second field integral measurements.

The magnetic measurement capabilities are as follows: Hall probe measurements can measure the field strength (i.e. effective K-value) within an accuracy of 10^{-4} with proper averaging. Measurements of the first and second field integrals with a flipping coil system are reproducible with accuracies of 5 G-cm and 1000 G-cm², corresponding to 0.1 μ rad and 0.2 μ m, respectively, for an electron beam energy of 14.3 GeV. Measurements of phase slippage over the length of the device are reproducible to 0.5 degrees in phase.

Therefore, the present state-of-the-art measurement methods meet the accuracy requirements of the LCLS undulator line. For some measurements and adjustments, however, special attention is required to achieve the required accuracy. For example, horizontal field measurements in the presence of a strong vertical field are extremely difficult due to the planar Hall effect. The Hall voltage is given in the following equation:

$$V_h = V_0 + R_h B_y I_e - P B_t^2 I_e \sin(2\phi) \quad (8.30)$$

The last term represents the planar Hall effect, where ϕ is the angle between the component of the magnetic field that lies in the plane of the Hall probe and the direction of the current in the plane of the Hall probe. If there is a field component parallel to the probe plane, some additional Hall voltage may appear depending on the direction of the field component in the measurement. This planar Hall voltage is usually very small, but can become significant when B_t is much larger than B_y . Thus, measurements of the transverse component of the undulator field are made more complicated by the planar Hall effect.

Two different Hall probes have been tested for their ability to measure the transverse field. Measurements with each probe were compared to integrated measurements made with a stretched coil. The tests showed that it was impossible to match the reference data for both first and second field integrals simultaneously using the Bell probe. This could be due to imperfect alignment of the poles in the beam direction, but if it is, it would be because the probe had more demanding alignment requirements than the undulator application. In contrast, the Sentron probe measurements could be made to match the reference data after careful alignment of probe and undulator segment in the vertical direction. One cannot rely on Hall probe measurements alone, however, because each probe has a different sensitivity to angle and position errors. Calibration by some other means is always needed.

The other crucial adjustments are the phase tuning within an undulator segment and the adjustment of the phasing between undulator segments. Phase tuning within an undulator segment can be done by shimming or by mechanical local adjustments to the undulator gap. Phasing between undulator segments is affected by the physical separation between undulator segments

and by the phasing through the adjacent end sections of the two undulator segments. The physical break length is of course set when the undulator line is constructed. The phasing through the end sections can be adjusted by applying phase shims near the ends of the undulator segment or by introducing a small gap change at the end of the undulator segment. The latter technique has the advantage that the phasing can be adjusted during the actual operation of the FEL, using the FEL output as feedback. It would allow phase error accumulation to be avoided through the whole beamline.

8.3.3 Requirements for Measurement Facility on LCLS Site

The existing measurement facility at APS has adequate resolution and reproducibility for the measurement and tuning of undulator segments for the LCLS project. However, the shipment of tuned undulator segments from Argonne to SLAC may affect the magnetic quality of the undulator segments so they no longer meet the demanding magnetic field quality and stability requirements. For example, a gap change of just over a micrometer may introduce 10° phase slippage. To meet these demanding magnetic requirements, very rigid and reliable construction of the device is necessary. Also, the final tuning of phase slippage should be done by phase tuning at the ends of undulator segments after delivery of the devices to the LCLS site. It is necessary to have the same undulator measurement systems at SLAC as at APS. (A Helmholtz-coil system to measure individual magnet blocks is probably not necessary, however.) In addition, a pulsed wire system for finding the center of a quadrupole within the required tolerance ($< 50 \mu\text{m}$) will be acquired.

8.4 Measurement and Sorting of Magnet Blocks

8.4.1 Characterization of Magnet Blocks with Helmholtz Coils

The requirements for the LCLS undulator are demanding. To help ensure that these requirements can be met, tight tolerances must be imposed on the magnetic properties of the permanent magnet blocks to be used in the undulator segments. In addition to requiring that the magnets be strong (a remanence B_r of 1.2 T is specified for the NdFeB permanent magnet blocks), they are also required to be uniform. Each individual magnet block is required to have a total magnetic moment that is within $\pm 1\%$ of the average total moment, where the average is taken over the entire population of magnet blocks. The direction of the total magnetic moment vector is also required to lie within 2° of the mechanical axis of the magnet block.

These requirements are checked by measurements made using a system of Helmholtz coils. The vendor measures the magnet blocks when they are manufactured, and the blocks must be measured again by the manufacturer of the undulator magnetic structure. Those measurements are then used in sorting algorithms in order to minimize the effect of errors.

The Helmholtz coil measurement system uses a servomotor to rotate the magnet that is held at the center between a pair of coils. A fast 16-bit ADC board is used to measure the signal from the coils on the fly as the magnet is rotated. Typically 2000 points per turn are recorded. A digital integration in software gives the flux of the magnet block at each point during the rotation.

This gives the orientation of the magnetic moment in one plane; to determine the angle in the perpendicular plane requires that the magnet block be turned by 90° and the measurement repeated. This by 90° repositioning are done manually. The data file for each magnet block is analyzed to determine the total magnetic moment and its projections along the mechanical axes of the block.

A set of 500 magnets has been received for use in building a prototype LCLS undulator segment. Their field uniformity exceeds the specification. The vendor's Helmholtz coil measurements for those blocks show that the total moment on each magnet block lies within $\pm 0.5\%$ of the average total moment of all the blocks. The magnet blocks have effectively no transverse (x) component to their magnetic moment. They have a systematic vertical (y) component to the magnetic moment, however, and the angle of magnetization is $1.0 \pm 0.3^\circ$ from the mechanical axis of the magnet. The magnets are symmetric so that they can be installed in the prototype in either of two orientations, i.e., with the vertical component of the magnetic moment up or down. This will allow the direction of the vertical magnetic moment to be chosen when the magnetic structure is assembled.

Some of the magnets have also been measured with the APS Helmholtz coil system. These measurements show excellent agreement with the vendor's measurements. The rms difference was $\pm 0.06\%$ for the first 35 magnet blocks to be measured.

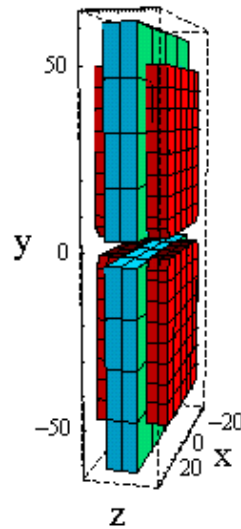


Figure 8.3 Schematic drawing of the half-period measurement fixture. A pole (shown in red) is on either side of the central magnet (shown in blue), on both top and bottom.

8.4.2 Characterization of Magnet Blocks with Half-Period Fixture

The LCLS magnets were measured using a specially designed fixture based on the half-period-model of the device. This fixture consists of 4 poles and two magnets as shown in **Figure 8.3**.

The magnet installed in the bottom part of the fixture remains in place and only the top magnet is changed. A 2-axis Hall probe and a moving coil were used to measure the field integral. Hall probe measurements of the vertical field integral for each of the magnets, are shown in **Figure 8.4**. The direction of the vertical component of the magnet moment makes a systematic difference for nearly all of the magnet blocks. The magnet in the bottom of the fixture has positive M_y . When magnets of opposite sign of M_y are paired, the integrated field is smaller, and, in fact, is very close to the earth's field contribution of -15 G-cm. This difference can also be seen in **Figure 8.5**, where the field integral measurements were repeated with the vertical moment of the top magnet reversed for some of the magnet blocks. The vertical moment of the magnet block makes a difference in the field integral that is nearly systematic, but a few of the magnet blocks give a different result. It probably results from a different distribution of magnet moment within the block, and cannot be determined by the Helmholtz coil measurements of the total moment.

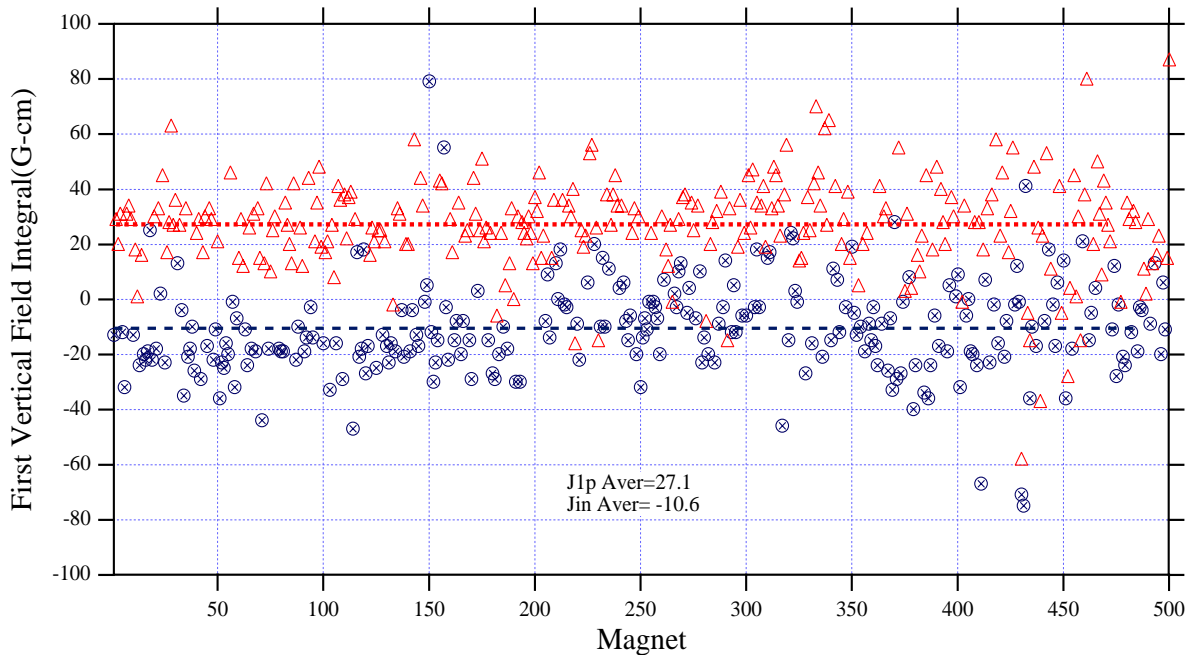


Figure 8.4 Integral of the vertical field through the half-period fixture, for different top magnets. The red triangles are for magnets with positive M_y (the same as the bottom magnet); the blue circles are for negative M_y (opposite from the bottom magnet). The lines show the average value for the similarly shaped points

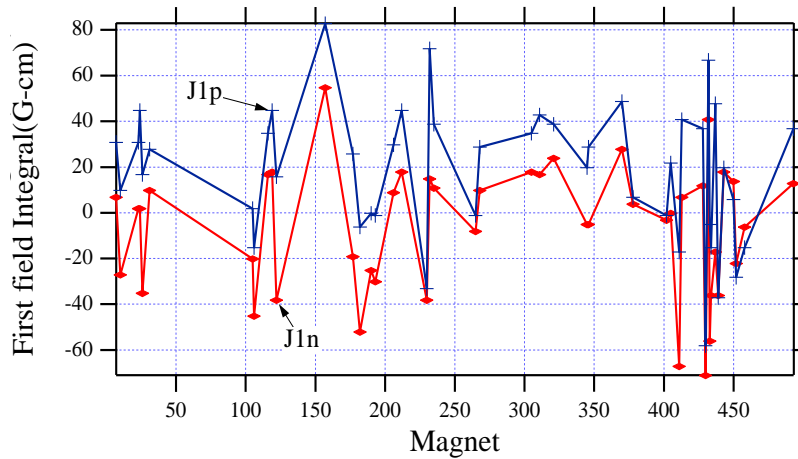


Figure 8.5 First vertical field integral through the half-period fixture when the same magnet block is oriented with its vertical moment positive (blue +) and negative (red -) for a few of the magnets. The positive orientation usually gives a higher integral, but not always.

Another characteristic of the assembled magnetic structure that cannot be predicted from the Helmholtz coil measurements is the phase variation. This can be seen in **Figure 8.6**. The vertical component of the field in the fixture has been measured for both orientations of the vertical moment of the magnet block (the direction of the main component of the block's moment is the same). The difference between these two measurements is plotted. The plot also includes the result of a calculation that assumes a uniform distribution of magnetization. The difference seen between the measurement and calculation can affect the contribution to the phase error from the magnet block.

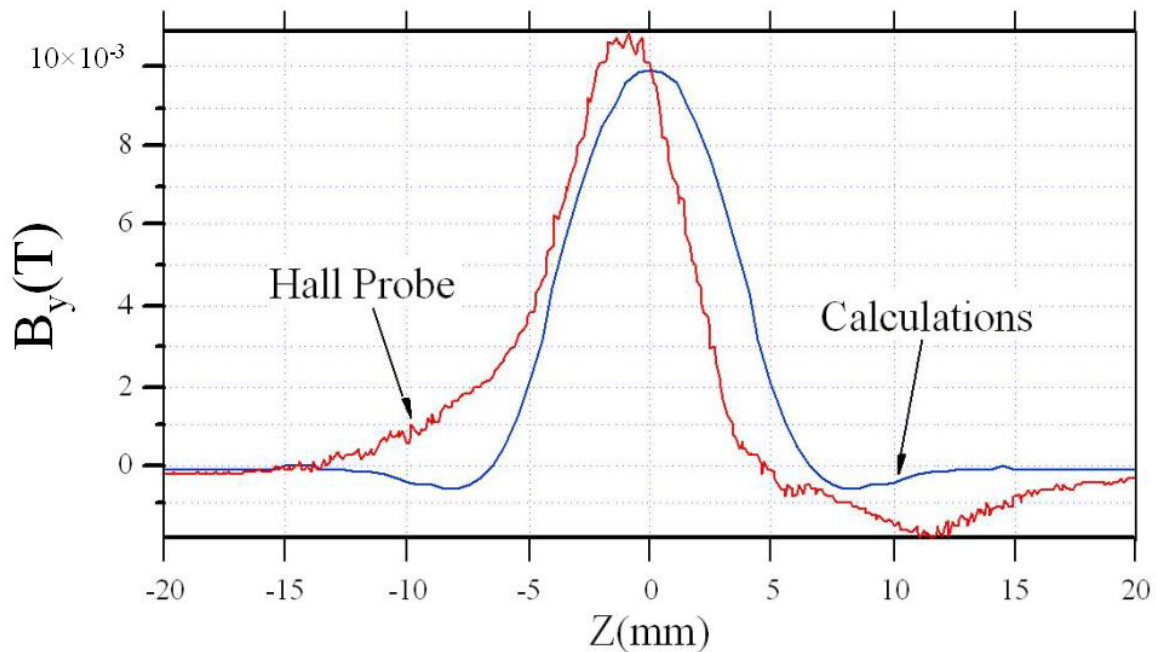


Figure 8.6 Difference in vertical on-axis field when a magnet block is rotated to change the vertical component of the field, plotted vs. z . The measured effect may differ from the calculation if the distribution of the vertical magnetization in the magnet block is not uniform; this can affect the phase errors.

8.4.3 LCLS Prototype Undulator Segment

A prototype undulator segment for the LCLS is under construction. Measurements of the magnet blocks using both the Helmholtz coils and the half-period fixture will be used to sort and orient the magnet blocks for installation in the magnetic structure. The best criteria to use are still being investigated.

8.5 Magnetic Design for the Undulator

A standard planar hybrid undulator, with a period of 30 mm and an effective K of 3.71 (effective B of 1.3250 Tesla) has been designed for the LCLS. The magnetic gap of each undulator segment will be set to whatever is needed to achieve the field strength; it is expected to be near 6 mm.

8.5.1 Choice of Magnet Material

The possibility of radiation damage to the magnets and ways of reducing the risk of radiation damage to the magnets is one of the first things to consider in the design of an undulator magnetic structure. Radiation exposure has been found to be a danger to undulator magnets. At the European Synchrotron Radiation Facility (ESRF), an insertion device was damaged when its magnets were demagnetized locally, adjacent to the electron beam [9,10]. At the Advanced Photon Source (APS), the magnets in the insertion devices in one sector were found to be slightly demagnetized after a run in which the dose to that sector was unusually high. The dose was beyond the range of measurement of the dosimeters being used, and the dosimetry techniques are being modified for the future. In order to avoid (or delay) future damage, more attention is being paid to maintaining a high injection efficiency and consideration is being given to other possibilities for reducing the dose to the insertion devices in that sector. Research is ongoing to investigate what levels and types of radiation exposure are hazardous to magnets. Although much is still unknown about this, a reasonable assessment can be made about the potential risks to LCLS undulator magnets based on what is known. The conclusion is that the possibility of radiation damage to the undulator magnets cannot be ignored. Initial operating experience with the APS FEL showed that the dose received by the undulator magnetic structures is comparable to the dose received by the undulator segments installed in the APS storage ring. In addition, the radiation exposure of the LCLS magnets is potentially more damaging than the radiation exposure of storage ring magnets, because of the higher energy of the LCLS electron beam. Magnets can tolerate high levels of low-energy radiation (hundreds of mega-rads of 1-MeV Co radiation) without demagnetizing, but higher energy radiation may cause demagnetization at lower doses [11]. Thus, the 14.35-GeV electron beam of the LCLS is more capable of producing potentially damaging radiation than the 7-GeV beam of the APS or the 6 GeV beam of ESRF.

The magnetic design of the undulator structure will also affect the radiation hardness of the undulator magnetic material. This is because the likelihood of radiation-induced demagnetization has been found to increase when the demagnetizing field experienced by the magnet block is stronger [12]. Part of the analysis that is done during the magnetic design process is to examine

the localized demagnetizing field experienced by different parts of the magnet blocks, over the full range of intended gaps. A normal goal of the design process is to maximize the on-axis field of the undulator segment at the smallest gap while ensuring that the demagnetizing field seen by the magnets is not excessive at small gaps, nor at any larger gaps – after all, the undulator segment must be assembled one jaw at a time (corresponding to a very large gap) before the jaws are brought close together. The maximum allowable demagnetizing field is determined by the grade of the magnet material being used and what that grade of material can tolerate without permanent demagnetization. Additional margin in the maximum allowable field should be included for temperature effects, because permanent demagnetization will occur at a weaker demagnetizing field if the magnet is at a higher temperature, and neither an air-conditioning failure nor transport in an enclosed truck on a hot day should put undulator segments at risk. Temperature dependence information is available from the magnet manufacturer in the form of B-H curves at different temperatures. Similarly, additional margin should be allowed for radiation exposure because exposure is more likely to result in demagnetization if the demagnetization field seen by the magnet is closer to the field at which permanent demagnetization occurs in the absence of radiation.

One way of reducing the demagnetization risk of the magnets is in the choice of the grade of magnet material. Different grades of NdFeB magnet material were considered and material (N39SH) meeting LCLS needs is commercially available. The remanence of this material is 1.23 to 1.29 Tesla and the intrinsic coercivity iH_c is a minimum of 21 kOe. This grade of magnet has a high remanent field but it was mainly chosen because of its particularly high intrinsic coercivity. The high coercivity correlates with a better resistance of the magnet material to radiation-induced demagnetization, and with this grade of magnet the high coercivity can be obtained without sacrificing magnetic remanence as compared to the older N38H grade of NdFeB that has been used in many insertion devices, including most of those at the APS.

Table 8.3 Predicted values for the undulator magnetic model.

Parameter	Value
Period length	30 mm
Gap	6 mm
Peak field on axis ¹	1.390 Tesla
Effective field on axis ²	1.348 Tesla
Effective K	3.776
Force per pole	258 N

¹ The peak field is the maximum measured field amplitude.

² The measured field amplitude is not exactly sinusoidal. The effective field is the amplitude of an equivalent sinusoidal field that would produce the same first harmonic energy as the measured field.

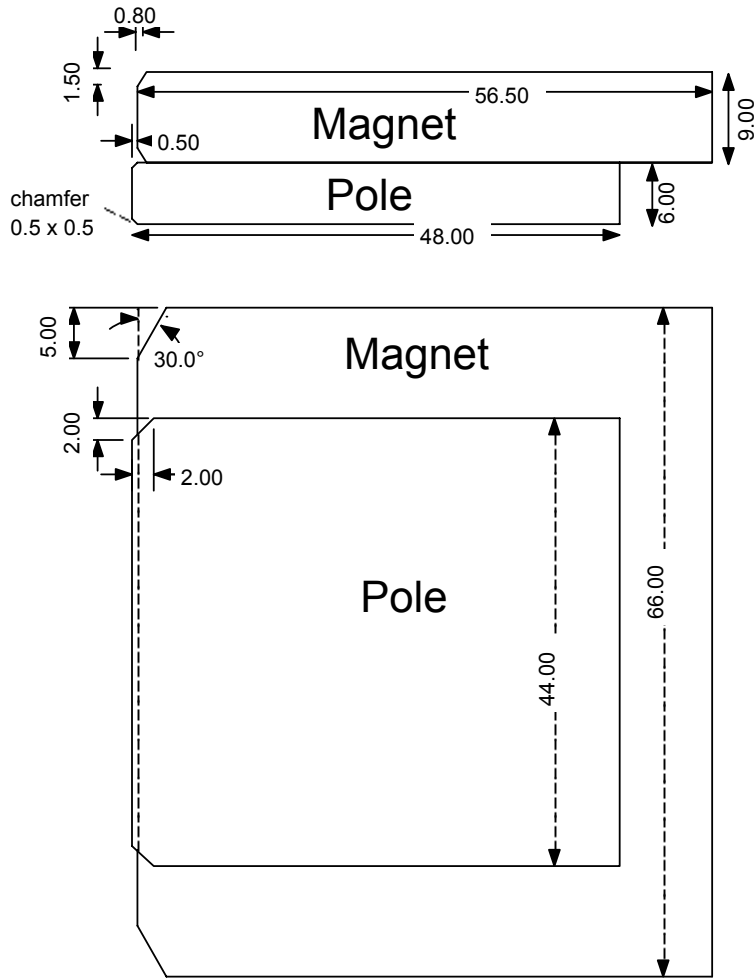


Figure 8.7 Magnetic design for the undulator magnetic structure. Minor changes to this can be made for mechanical convenience without affecting magnetic performance.

8.5.2 Undulator Magnetic Model

The magnetic design of an undulator segment is shown in **Figure 8.7**. The design was developed using the magnetic calculation codes Opera-2D and Opera-3D, by Vector Fields. In the calculations, a remanent field of 1.2 Tesla is used for the magnet material. This is slightly lower than advertised by the vendor, but it has worked well for modeling APS undulator segments in the past. The B-H curve that is used for the vanadium permendur of the pole is one that also has worked well previously. The magnetic characteristics of the model as predicted using the 3-dimensional code are shown in **Table 8.3**. Note that there is a small margin as compared to the specification of $K_{\text{eff}}=3.71$ at 6 mm gap. (The gap of the device will be adjusted during magnetic tuning to make the final K_{eff} be the design value of 3.71.)

8.5.2.1 Two-Dimensional Model

In the magnetic design process, two-dimensional modeling is used for the initial scoping of the problem. The relative thicknesses (parallel to the beam direction) of the magnet and pole are determined, along with the heights of the magnet and pole. The details of the chamfering at the tips of the magnet and pole are also determined. These parameters are set so that the effective magnetic field on axis is a maximum, while ensuring that the demagnetizing field on the magnet does not become excessive. In the 2D model, the demagnetizing field is worst at open gap. **Figure 8.8** shows the demagnetizing field throughout the magnet. The worst is predicted to be 12.713 kOe, in the region of the magnet chamfer. This is about 1.11 times the magnet coercivity bH_c of 11.4 kOe. The typical magnet specification that has been used in the past required that the magnet not demagnetize below $1.2 \times H_c$, so this allows ample margin. The margin is even greater for the high-coercivity magnet grade that will be used.

The other feature of the magnetic model that is checked in the 2D calculations is the value of μ in the magnet at closed gap. **Figure 8.9** shows the calculated value of the permeability μ in the pole where it is 90 or below, i.e., where the pole is nearing saturation, for a gap of 6 mm. The μ in the pole is shown to be 90 or higher everywhere except in the chamfered corner, and the minimum μ that extends across the pole is 90. Although there may be some small redistribution of the flux due to the saturation near the pole chamfer, the central region of the pole still serves well as a flux conduit.

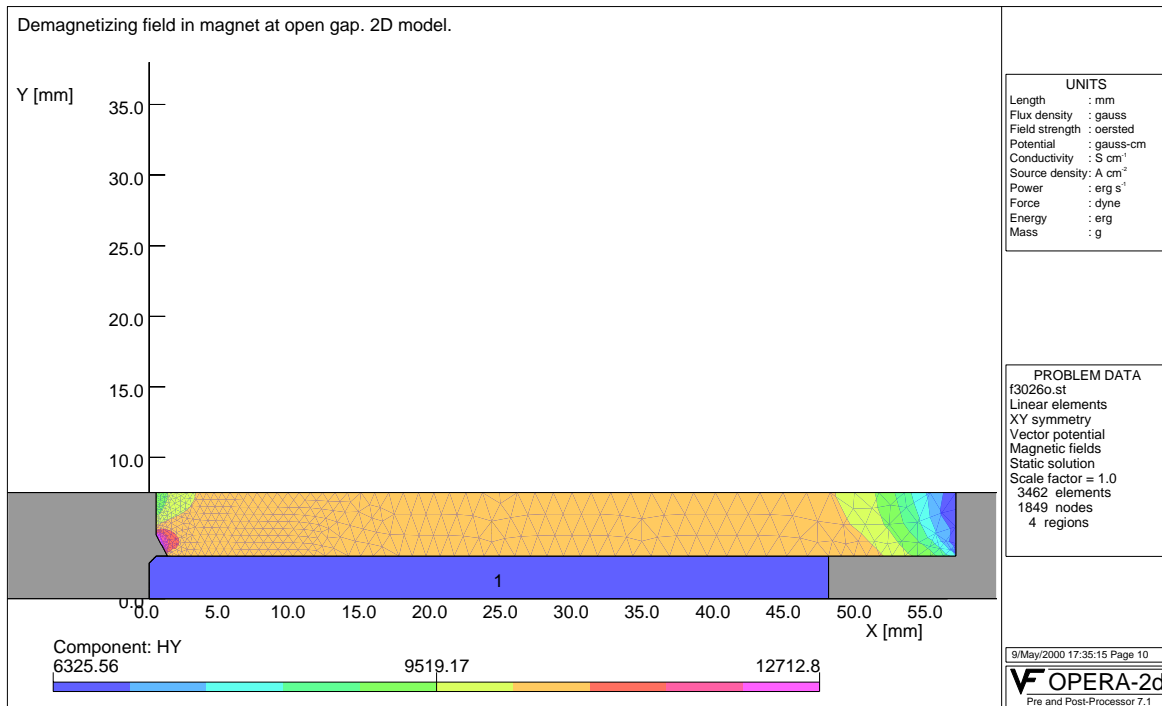


Figure 8.8 A quarter-period model of the magnet structure showing the demagnetizing field in the magnet, in the 2-D model, at open gap. The particle beam would travel up the page on the left, in what is labeled here as the 'y' direction. The half-pole is on the bottom here, and the half-magnet on top.

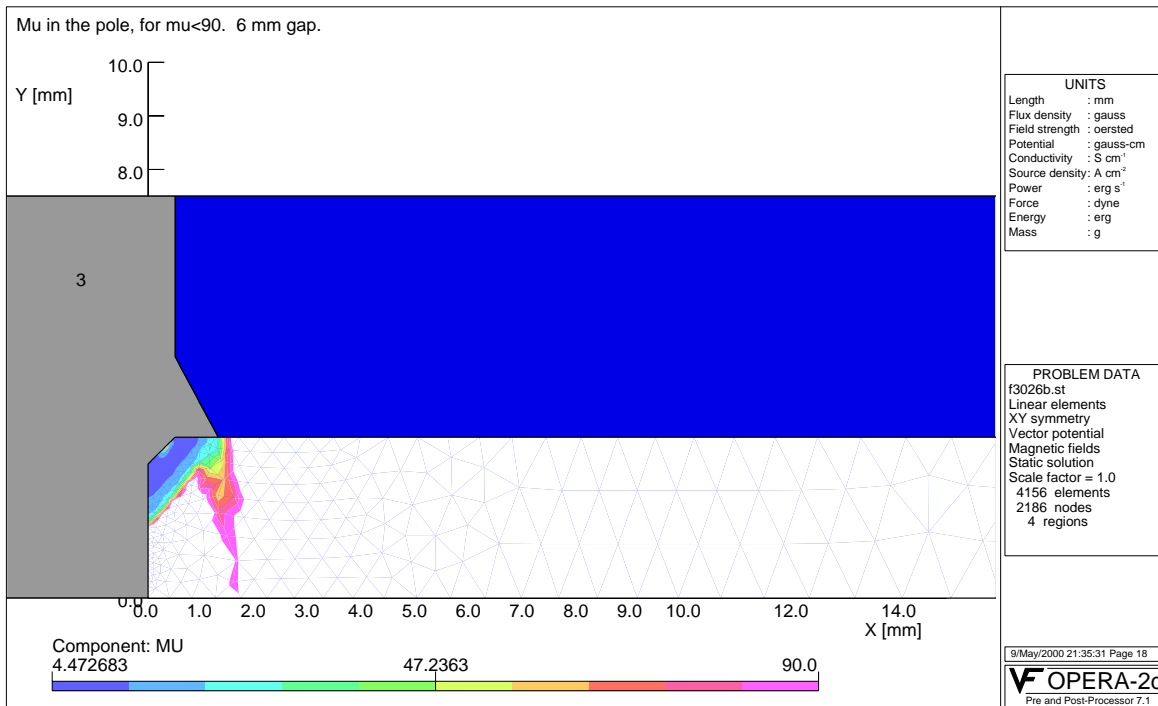


Figure 8.9 Partial quarter-period model of the magnetic structure, showing the areas of the pole where μ is below 90 at minimum gap (6 mm). In the white areas, μ is above 90. Although the pole is saturating in the region near the chamfer, as shown by the low μ , most of the pole, even at the tip, is comfortably far from saturation.

8.5.2.2 Three-Dimensional Model

The undulator magnetic design is also examined using three-dimensional calculations, particularly to determine the peak field on axis and to examine the distribution of the demagnetizing field within the magnet. **Figure 8.10** shows the calculated demagnetizing field in the magnet in a plane immediately adjacent to the pole, at the nominal gap of 6 mm. The magnet extends farther transversely than the pole; the demagnetizing field is worst at the transverse edge of the pole and next to the gap. It is also of interest to view the demagnetizing field in the plane perpendicular to this, at the edge of the pole where, in this view, the field is strongest. This is shown in **Figure 8.11**. The strongest demagnetizing field is about 1.53 Tesla, leaving a good margin to the 21 kOe intrinsic coercivity of the N39SH magnet material grade. The peak demagnetizing field calculated at open gap in the 3D model is about the same as at minimum gap.

Another characteristic of the model that is checked is the transverse uniformity of the on-axis field. The pole can easily be wide enough that the transverse alignment of the undulator is not critical. **Figure 8.12** shows the transverse roll off in the peak on-axis field. An error of $\Delta B/B = 1.3 \times 10^{-4}$ is reached at a transverse position of ± 2.9 mm.

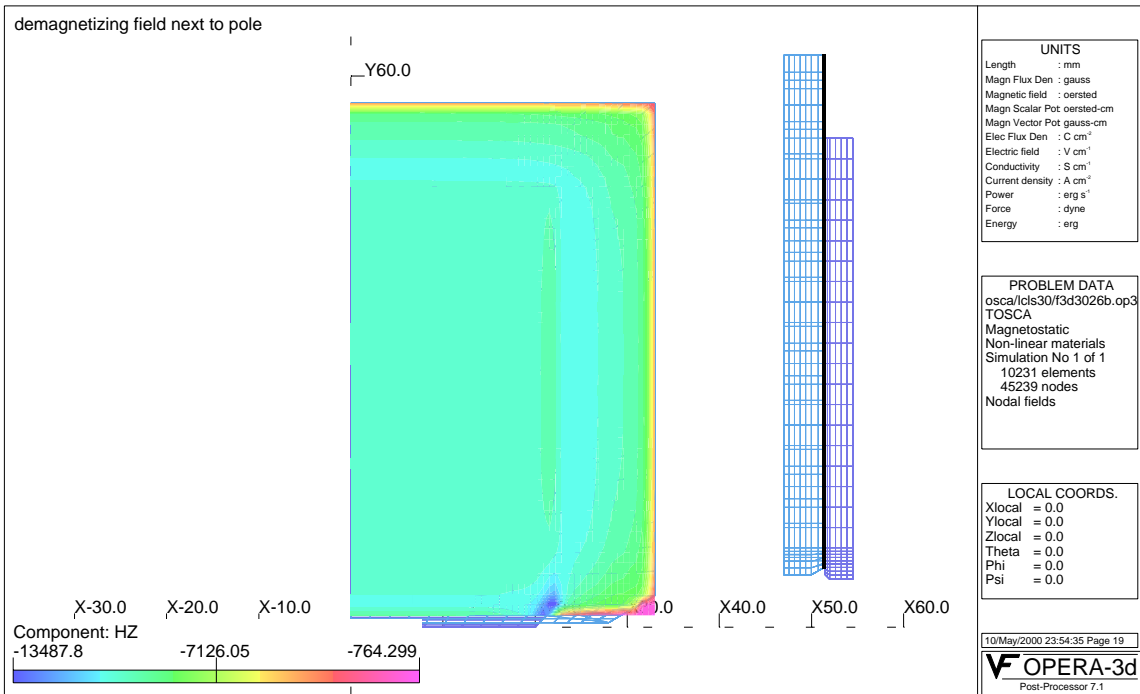


Figure 8.10 Three-dimensional model calculation showing the demagnetizing field in the magnet at minimum gap, in a plane immediately adjacent to the pole. The inset at right is a side view of the model; the black line shows the plane where the demagnetizing field was calculated.

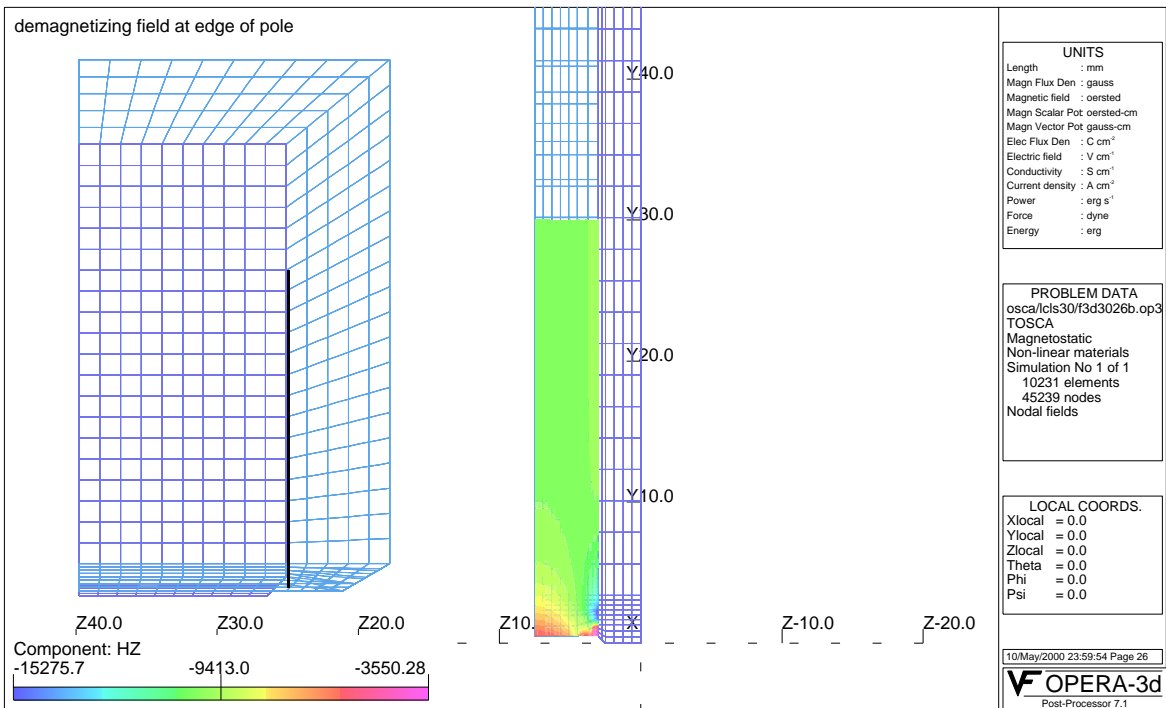


Figure 8.11 Side view of the demagnetizing field in the magnet. The black line in the inset at left (not to scale) shows the plane at the edge of the pole where the demagnetizing field was calculated. The worst demagnetizing field is adjacent to the pole and just above

the chamfer.

Once the magnetic gap of the undulator is determined, the maximum size for the vacuum chamber is also set. The difference between undulator gap and vacuum chamber outside dimension must include allowances for mechanical variations of 0.20 mm, an allowance for the difference between the magnetic model calculation and reality of 0.12 mm (this is based on the measured variation in the APS standard undulator segments A), and an allowance for uncertainty in the magnet material remanent field of 0.08 mm. This adds up to a total of 0.40 mm. Thus, if the nominal magnetic gap of the undulator is to be 6 mm, the maximum external dimension of the vacuum chamber is 5.6 mm. Although building a prototype undulator segment may allow some relaxation in this difference, it will not be large.

Some options were considered for ways to increase the minimum gap of the undulator. The magnets and poles could be wedged, but this only increased the field by about 3%. It would allow an increase in the gap by about 0.3 mm, but wedging the magnets and poles is an expensive alternative. The small increase in undulator gap was not deemed to be worthwhile. Wedging the magnet would also mean that the magnet blocks would not be symmetric top-to-bottom. If the magnet blocks are symmetric, the option exists to turn them over if, for instance, reversing the vertical component of the block's magnetic moment would improve the overall undulator magnetic field.

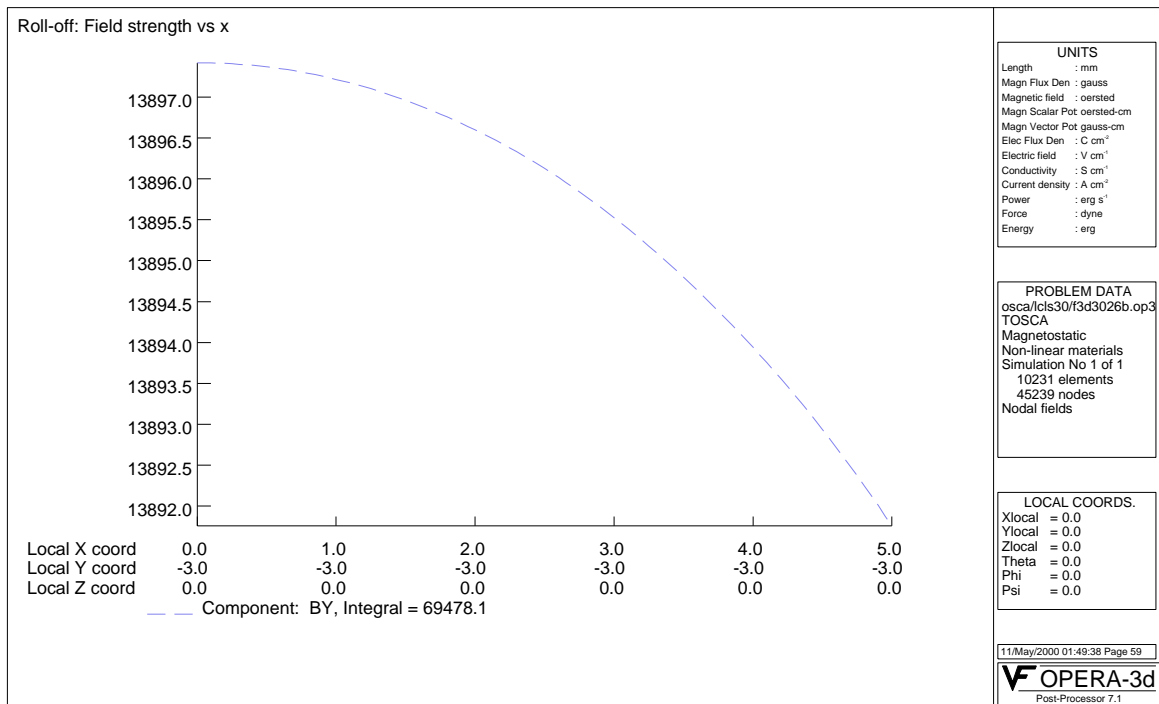


Figure 8.12 On-axis field strength under the pole vs. transverse position. A difference in field strength by $\Delta B/B = 1.3 \times 10^{-4}$ occurs at transverse positions of ± 2.9 mm.

8.5.3 Undulator Segment Ends

It is critical that the trajectory of the electrons be straight through the undulator line. The undulator will be tuned magnetically to keep the trajectory straight through the undulator. Attention must be paid to the design of the ends, as well as their implementation, in order to avoid a trajectory kick or offset. Ideally, the undulator segments will have neither kick nor offset. This can be achieved in the design by making the strengths of the end poles in the sequence $1/4$, $-3/4$, 1 , -1 , ... because that end configuration gives zero angle and zero displacement to the beam trajectory. In the first approximation, this is accomplished by making the last magnet only half as strong as the rest of the magnets. The magnet will be made weaker by baking it to increasingly higher temperatures, until the desired strength is reached.

There will also be a magnetic shield at each end of the undulator segment to limit how far the end field extends. This shield will be in place when the undulator segment is tuned, so its effect will be included in the magnetic measurements.

Proper phasing between undulator segments also demands proper tuning of the undulator segment ends. The magnetic phasing must match the physical distance between undulator segments. End phase tuning techniques were developed for the APS FEL that could tune the phasing by $\pm 38^\circ$; these techniques will be applied to the LCLS undulator segments. It is, of course, preferable to start with a mechanical break distance that matches the phasing achieved with no tuning of the undulator segment ends. The original calculations for different break distances assumed that the ends of the undulator segments have sharp magnetic cutoffs. In reality, of course, the ends aren't sharp, so those break distances need to be adjusted before final dimensioned plans are made. The necessary correction has been estimated by scaling from the 3.3-cm undulator segments of the APS FEL. The correction changes the regular short and long break lengths from 231 and 463 mm, respectively, for sharp segment ends, to 187 and 421 mm. This is not a negligible correction, especially when accumulated over many undulator segments. The proper corrections for the real undulator will be determined once the prototype undulator segment is assembled and measured.

8.6 Mechanical Design

8.6.1 Design of Magnetic Structure

The 3.4 meter long LCLS undulator segment has a fixed 6-mm pole gap. The design approach, developed for the LCLS, will allow extremely precise tolerances to be achieved. These tolerances are mandatory for the proper operation of this device. A cross-section of the undulator segment housing and pole structure is detailed in **Figure 8.13**. **Figure 8.14** is an enlarged cross-sectional view of the magnets and their holders. The tolerances for the device are listed in **Table 8.4**.

Table 8.4 LCLS undulator segment tolerance specification (X is the undulation plane, Y is the vertical plane and Z is along the beam direction)

Parameter	Tolerance
Pole gap tolerance	± 0.006 mm
Neighbor pole gap difference (selective assembly)	± 0.003 mm
Period variations: between neighboring poles	± 0.050 mm
accumulated error	± 0.050 mm
Pole thickness	$- 0.05$ mm
Pole transverse displacement (top and bottom)	± 0.20 mm
Pole displacement in "Z" direction (top and bottom)	± 0.10 mm
Pole face parallelism (top and bottom)	< 0.1 mm
(angle may open outside only)	< 1.75 mrad
Pole gap rotation around "Z" Axes over the whole length	< 5.25 mrad
Undulator segment sag due to its weight in the vertical (y) direction	< 0.002 mm
Undulator gap adjustment (possible)	± 0.005 mm
(adjustment resolution)	0.001 mm
Undulator segment end motion (top and bottom)	0.080 mm *
(end motion resolution)	< 0.001 mm
Supporting pillar alignment:	
"X" direction	± 2.0 mm
"Y" direction	± 0.5 mm
"Z" direction	± 2.0 mm
Pitch, roll, & yaw of the pillars	0.75 mrad
Undulator segment vertical and horizontal remote alignment:	± 3.0 mm
Travel range	< 0.002 mm *
Resolution	
Drive system installation accuracy on top of the pillars:	
"X" position accuracy	± 0.5 mm
"Y" position accuracy	± 0.05 mm
"Z" position accuracy	± 1.0 mm

* actual requirements shall be determined during prototyping phase.

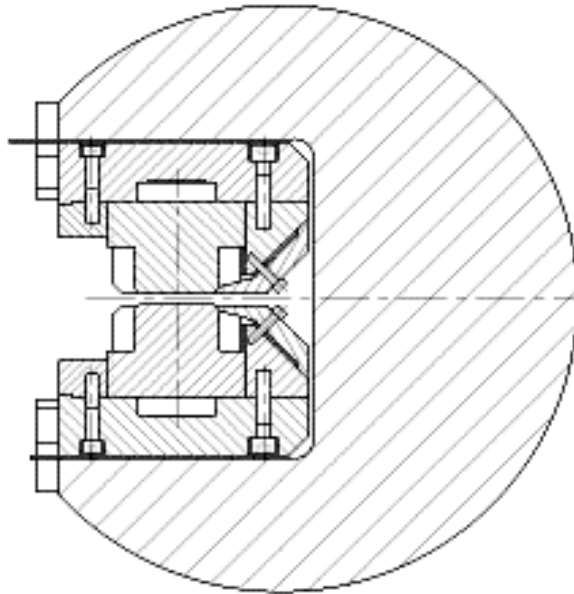


Figure 8.13 Cross-section of the undulator segment and strongback

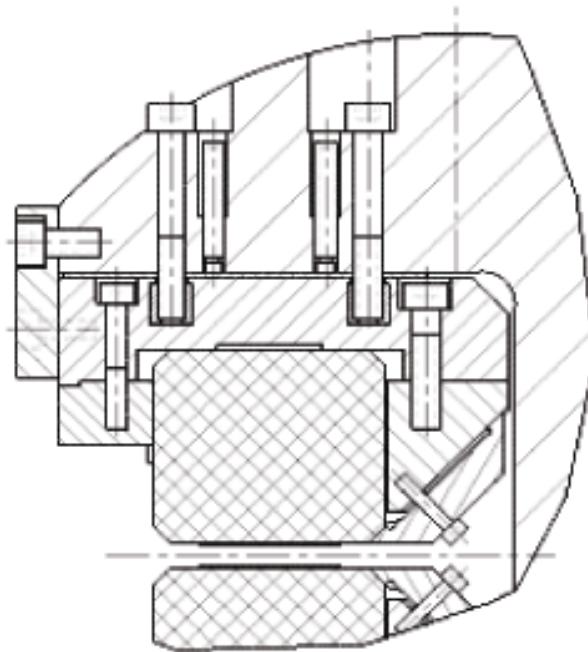


Figure 8.14 Enlarged view of the undulator segment

Parameters for the prototype undulator segment are listed in **Table 8.5**. The poles of the prototype undulator segments are located in precisely machined grooves located in the two sidebars. In order to achieve the maximum peak field, the magnets extend beyond the edges of the poles in three directions – on both sides, and in the direction away from the magnetic gap. There is no space on the gap side of the pole to clamp the pole into place, so the poles have

nonmagnetic “ears” added to their sides for clamping. The “ears” are made of titanium alloy and are ground and heat-treated along with the poles (see **Figure 8.15**). Titanium alloy was chosen because it possesses nearly the same thermal expansion as the pole material (i.e. vanadium permendur alloy). **Figure 8.16**, **Figure 8.17** and **Figure 8.18** show several pictures of a 9 pole, 5 period LCLS undulator segment model. It is obviously much shorter than the actual undulator segment, but clearly conveys the concepts used in the design.

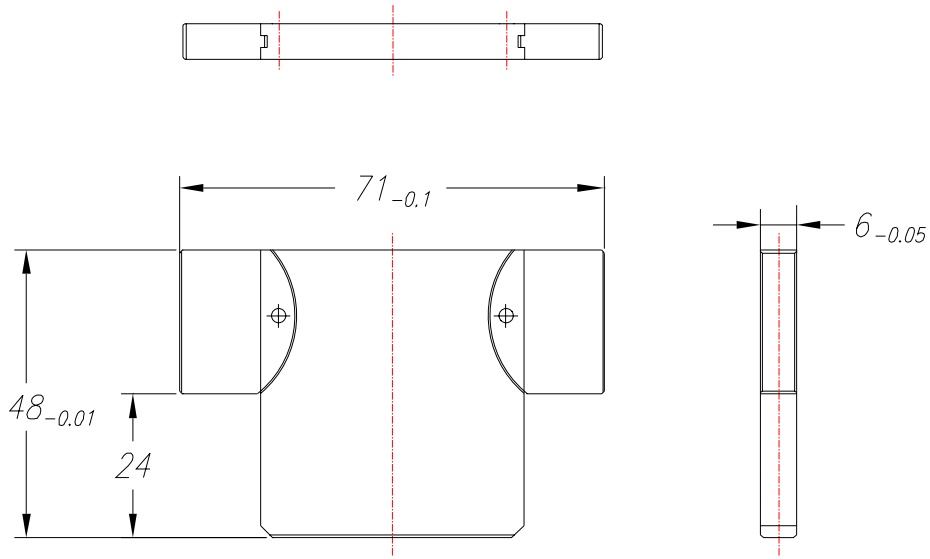


Figure 8.15 Titanium ‘ears’ are attached to the vanadium permendur poles so the poles can be clamped in place.

Table 8.5 Parameters for the LCLS prototype undulator segment:

Parameter	Value
Pole Gap (nominal)	6 mm
Period	30 mm
Pole Thickness	6 mm
Magnet Thickness	9 mm
Effective Field ³	1.325 Tesla
Effective K Value	3.71
Outside Dimensions	3400 × 305 × 450 mm
Weight	1100 kg.

³ Note that the calculated effective field specified in **Table 8.3** is a bit larger than the goal value given here. As stated in the text, the gap will be adjusted to make the final field equal to the goal value.

The magnetic structure is designed in such a way that only one clamp is required to hold each pole and each magnet, thus allowing one side of the structure (the back side in **Figure 8.18**) to remain open for the insertion of side shims.

The undulator segment core is made from a solid 3.4-m long titanium bar, which has a diameter of approximately 305 mm. A precise window machined along the entire length of the bar is used to locate the top and bottom magnetic jaws. The feasibility of this technique will be proven through manufacturing and testing of the prototype as unknown variables in the machining process such as material relaxation could cause twisting, bowing or warping. Titanium was chosen for the core material due to its low specific weight and low thermal expansion coefficient. The low specific weight will lighten the structure and thus decrease potential deflection of the undulator segment between supports; deflections of only a few microns are anticipated. Titanium's low thermal expansion coefficient will minimize thermally induced deflections caused by variations in the tunnel temperature. Temperature stability is very important to keep the magnetic field from changing significantly. The base plate, with its slots to hold the magnets and poles of the magnetic structure, is made of aluminum in order to partially compensate for the influences of temperature fluctuations, which can change the gap distances between poles (see Figure 8.13).

The prototype undulator segment has a total of 226 poles per jaw, and 225 magnets. The length of the magnetic array proper, including all poles and magnets, is 3381 mm. There is some space allowed at each end before the magnetic shield. The magnetic shields are 5 mm thick at each end, and the overall length of the undulator segment, including shields, is 3410 mm. Once the bolt heads are added in, the total mechanical length of the segment is 3422 mm. The Ti bar by itself is 3400 mm long.

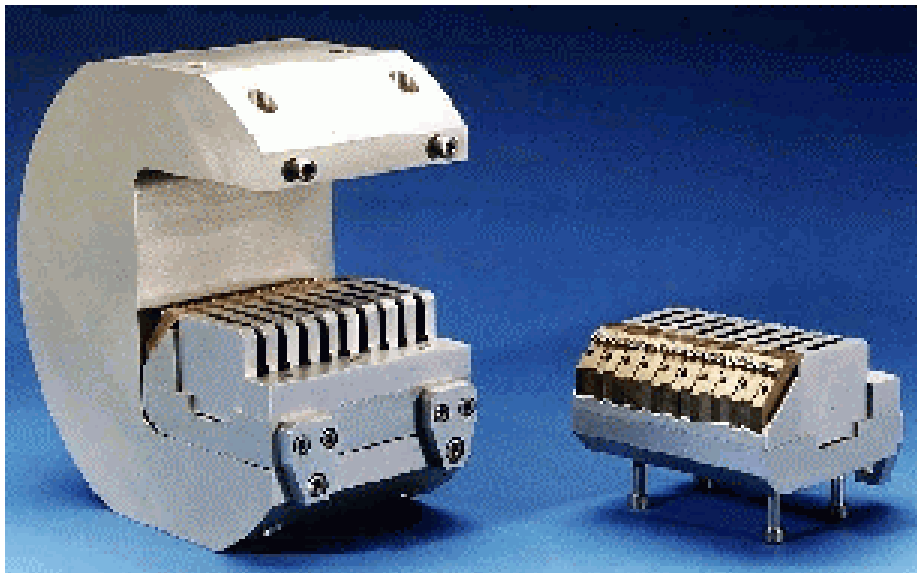


Figure 8.16 View of the short model of an undulator segment with upper jaw removed from the assembly

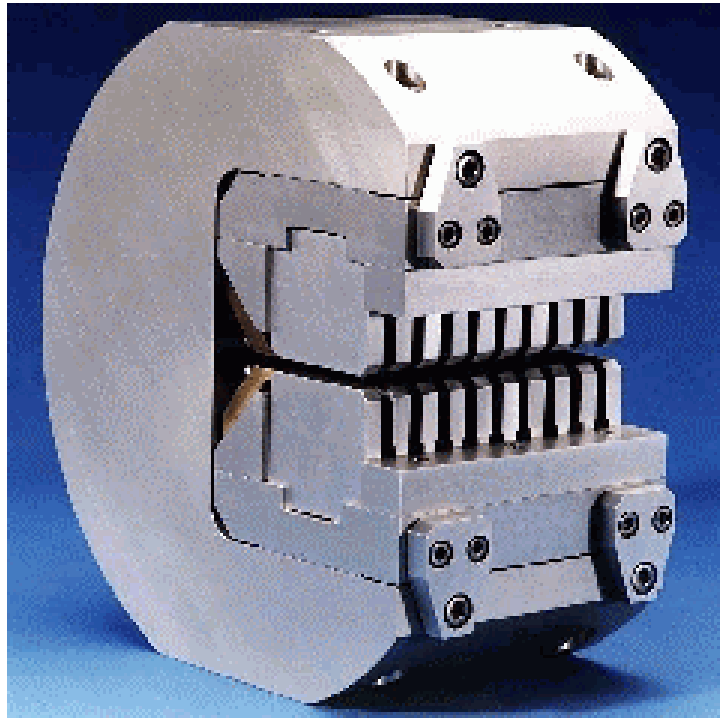


Figure 8.17 View of the short model (9 poles, 10 magnets) of an undulator segment, fully assembled. The C-shape housing will be made from titanium.

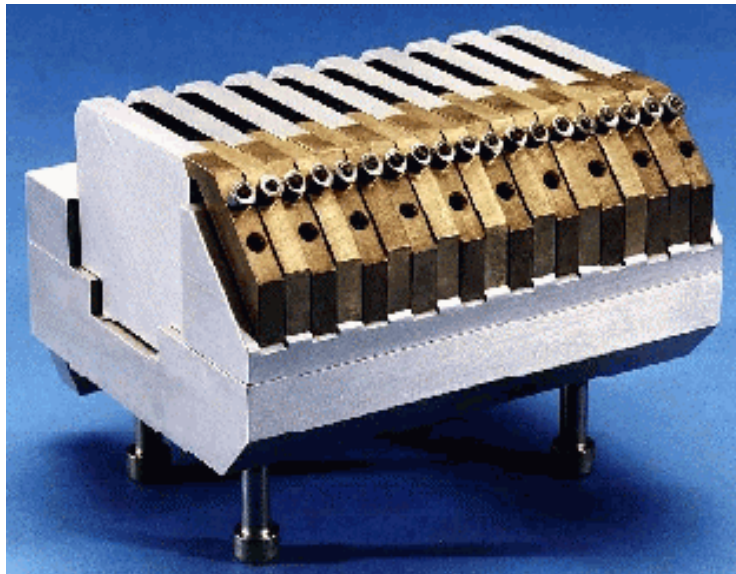


Figure 8.18 Upper jaw of the short model. Nine (dark) pole pieces are between the 10 magnets.

The attractive magnetic force generated by a 6-mm gap with a 30-mm undulator period is 17.7 N/mm length or 60,000 N for the entire structure. A cross-section of the titanium bar was modeled using ANSYS code. With an applied force of 17.7 N/mm length, the titanium bar has a deflection in the "Y" direction relative to the beam axis on the order of 7 microns per side. This was verified with several model variations of increasing complexity. **Figure 8.19** shows the

deflection in the "Y" direction for one of the model cases where the force was distributed along a line corresponding to the location of the magnetic jaws; the maximum deflection is 7.19 μm .

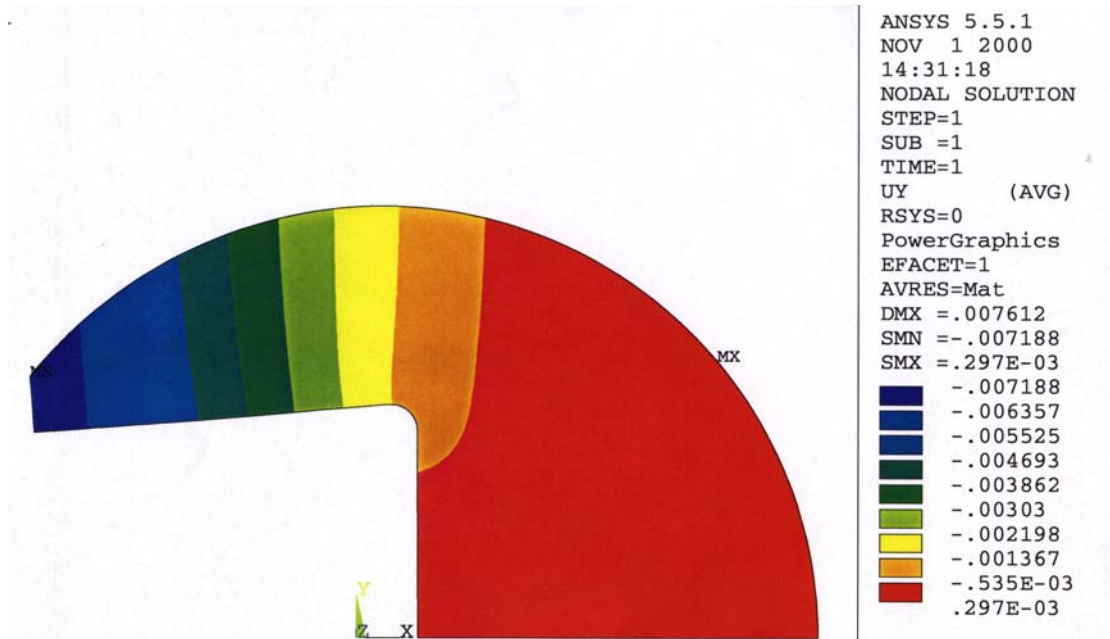


Figure 8.19 Calculated deflection of the titanium bar due to the magnetic forces.

8.6.2 Provisions for Magnetic Tuning

The magnets and poles of each jaw are assembled onto a base plate of aluminum, as mentioned above. The base plate for each jaw consists of five blocks placed end to end with three long blocks approximately 1-m long in the middle and a shorter block at each end. The design allows precision shims of various thicknesses to be placed between the core and jaw blocks in order to achieve precision tuning of the undulator segment. A series of these shims in 2-micron increments is being made for this purpose by precisely nickel-plating brass shims. There is also a design provision to achieve the same results using "push-pull" screws.

The magnetic structure can also be magnetically tuned using low carbon steel screws, referred to as side shims, which can be screwed in towards the poles in order to divert some of the magnetic flux and decrease the field under the pole. These side shims can be installed anywhere along the length of the undulator segment as required for precise tuning. The shim block assembly is shown in **Figure 8.20**.

The two end blocks of the base plate for each jaw can also be bent slightly, up to 80 microns, in order to change the gap at the end of the undulator segment. While this provides another means of tuning the undulator field strength, its primary function is for adjusting the phasing between the undulator segments. For this purpose, four PZT (Lead Zirconate Titanate) translators are housed inside holes within the titanium core as shown in **Figure 8.21**. The resolution of these translators is on the sub-micron level allowing very precise tuning of the undulator taper.

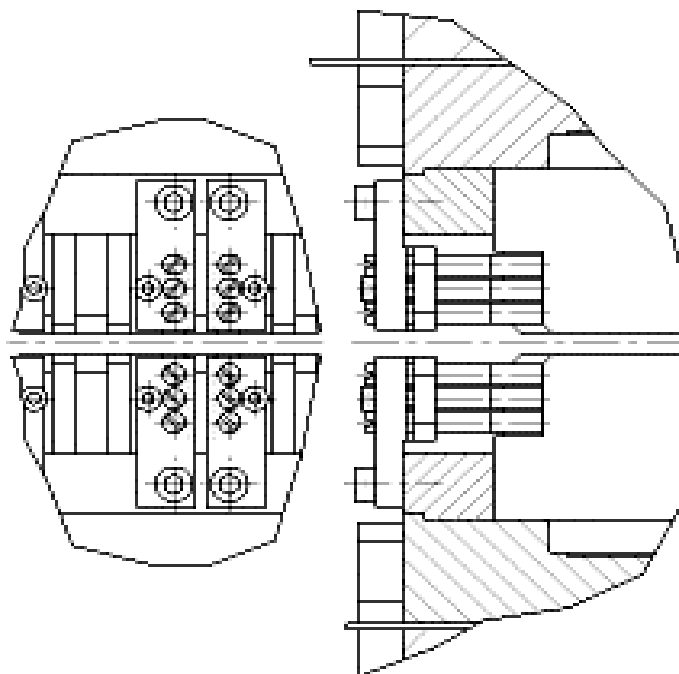


Figure 8.20 Low-carbon steel screws can be installed as necessary and positioned at varying distances from the poles in order to adjust the undulator field locally.

In conclusion, the following summarizes all of the design provisions that were made in order to achieve the high magnetic performance required for undulator segments. It is worth noting that the magnetic tolerance specifications for these segments are nearly an order of magnitude more stringent than those of the standard APS undulator "A".

- Precise tuning and measurement capabilities are required in order to make a precision magnetic device. For this reason, the space between poles is completely open (pole and magnet clamps are located only inside the device).
- For a very small fixed pole gap it becomes exceedingly complicated to use standard shims on top of the magnets to precisely tune the magnetic structure. Alternate provisions were made so that "push-pull" screws or a series of 2 micron increment shims can be used for tuning, greatly simplifying the process.
- Side shims can be used for final tuning.
- All components of the magnetic structure such as the poles, magnets, sidebars, and base plate have very precise mechanical tolerances.
- Along the length of the undulator segment, the magnetic structure is divided into five sections. The three middle sections can be tuned manually and the end sections can be slightly bent from a remote location with sub-micron accuracy in order to taper the

undulator segment.

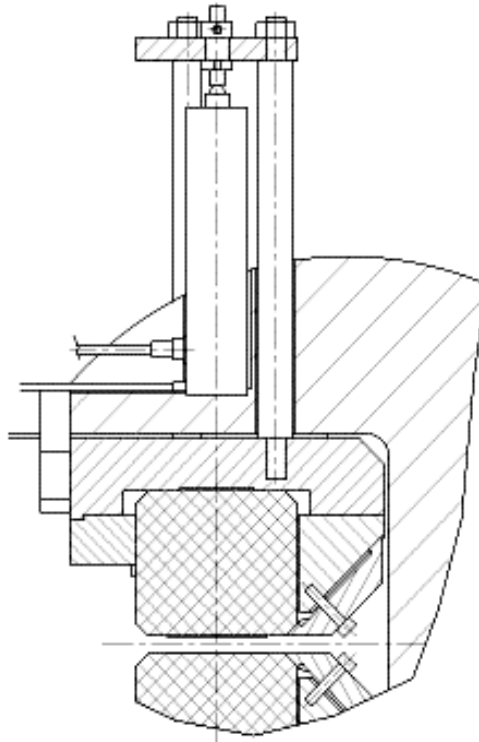


Figure 8.21 PZT translator located at the end of the undulator segment to adjust the magnetic gap of the end section. This adjusts the phasing between undulator segments.

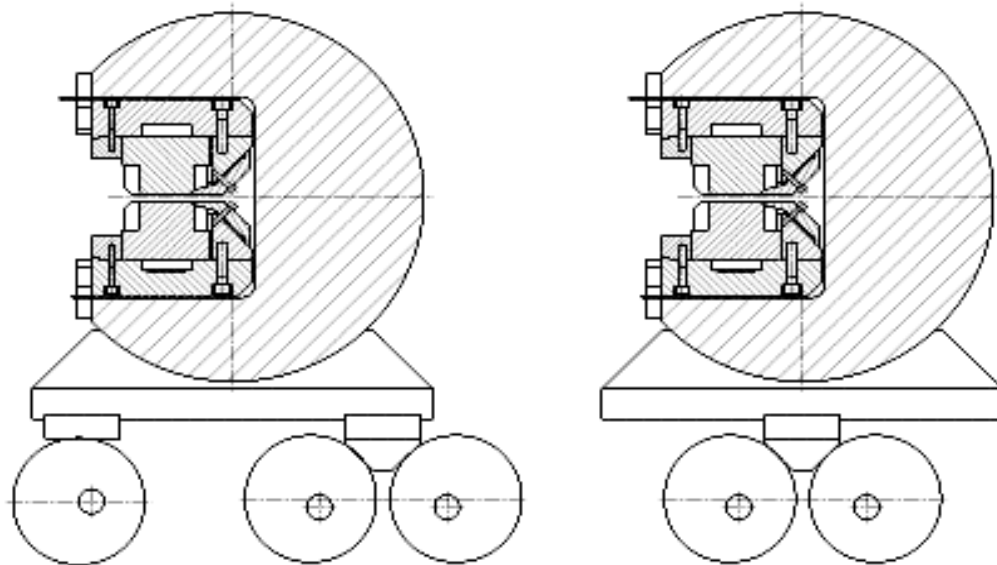


Figure 8.22 Schematic View of the undulator segment and movers showing three of the cams on one end of the segment and two on the other end.

- To ensure that the tight tolerances are met, each magnet and pole will be certified and a selective assembly procedure will be employed. The assembly will be performed in

an area where the temperature stability is better than $\pm 1^{\circ}\text{C}$.

- The core of the undulator segment is made from a solid titanium bar, to insure that long-term dimensional stability is maintained. Additionally, the titanium core shall be heat treated after both the rough and final machining processes in order to stress relieve the core.

8.6.3 Undulator Supports and Movers

Each undulator segment is supported on two pillars equipped with camshaft drive systems. The mounting scheme for the two ends of the undulator segment is shown in **Figure 8.22**. It is a three-point support. The cams that provide the support are eccentric, with an eccentricity of 3 mm. The support that uses a single cam can adjust the height only. The double-cam supports can adjust the height or the lateral position. By using the three support point adjustments 5 degrees of freedom in position adjustment are possible. There are no plans for adjustment of the z position.

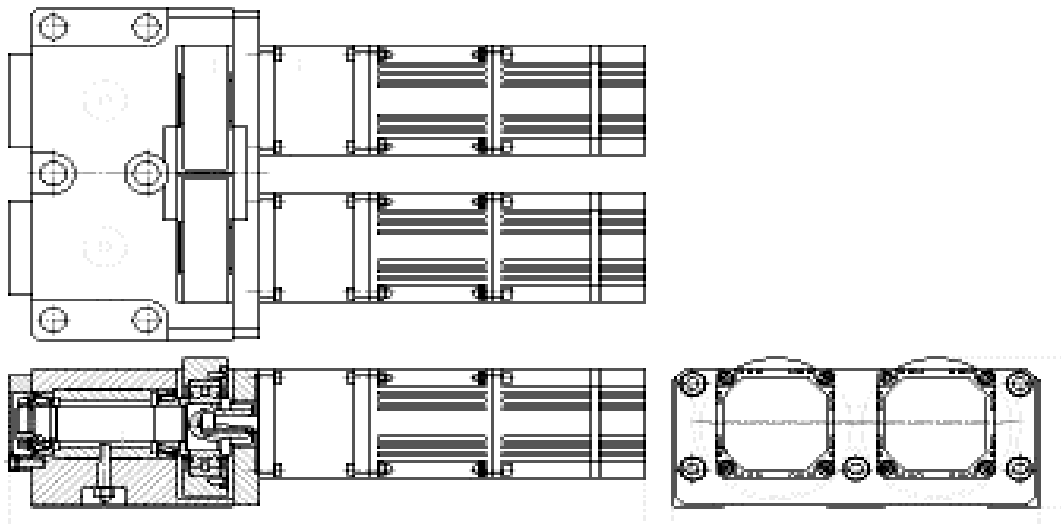


Figure 8.23 Eccentric cam mover system to adjust both height and lateral position.

Theoretically, the resolution of the mover system is better than one micron. In reality, the friction between the camshaft rings and undulator segment supports, tolerance inside of the roller bearings, etc. will determine the actual repeatability. This is expected to be well under the required tolerance.

Two different designs have been made for these units, one with only one camshaft and the other with dual camshafts. These systems are shown in **Figure 8.23** and **Figure 8.24**.

The piers are monolithic structures that will support the ends of each girder. The piers will also support components located between the girders. The piers will be made of Anocast[®] material. Its properties are more uniformly controlled and better known than concrete, and SLAC

has had positive experience with it and less satisfactory experiences with concrete for support structures.

To eliminate the diurnal temperature cycles associated with the ground, it is only necessary for the piers to extend 1–2 feet below the concrete floor [13]. Given that the piers should be set into the sandstone ground structure, the piers will extend about 60 cm below the floor level or more as required to reach the sandstone. The piers will be isolated from the concrete floor.

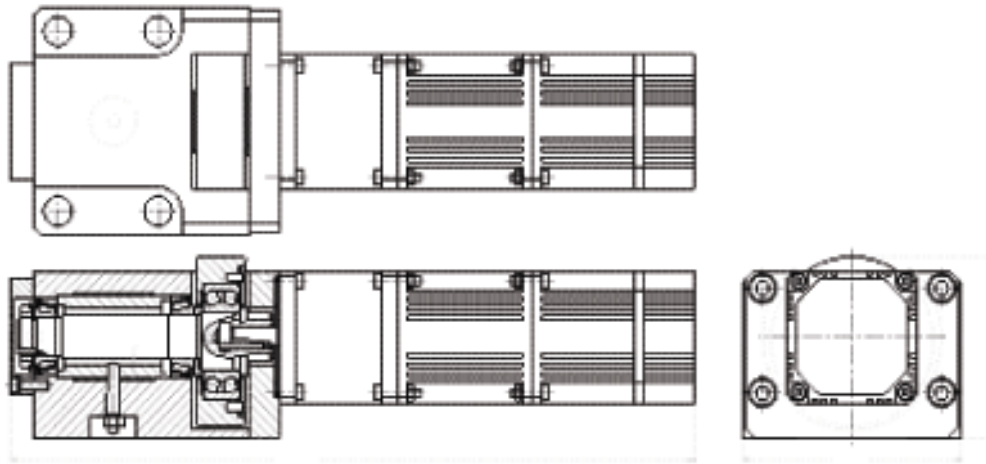


Figure 8.24 Eccentric cam alignment system to support and position one end of the undulator segment.

8.6.4 Thermal Considerations

Due to the low thermal expansion of titanium, it is estimated that if the tunnel temperature changes by $\pm 0.5^\circ\text{C}$, the resulting length change of the undulator segment will be on the order of only $\pm 15\mu\text{m}$. This change would not have a significant impact on the output wavelength of the undulator. The temperature variation in the strength of the undulator magnetic field due to the reduction in the remanent field of the permanent magnets at higher temperatures would have an effect, however. The remanence of the NdFeB magnets decreases by about 0.1% per $^\circ\text{C}$. This results in a decrease in the on-axis undulator field strength of about 0.054% per $^\circ\text{C}$. To compensate for this effect, the magnetic gap can be reduced due to differential thermal expansion as the temperature increases. Magnetic calculations show that to compensate for a 1°C temperature rise, the decrease in pole gap needs to be on the order of 8.6×10^{-4} of the gap. To accomplish this, an aluminum plate was placed between the titanium core of the undulator segment and the magnet/pole assemblies. The predicted decrease in pole gap for the model is approximately 8.26×10^{-4} , or almost the ideal value.

8.7 Permanent Magnet Quadrupoles

The FODO lattice of the undulator line incorporates permanent magnet quadrupoles. No provision is planned for adjusting the strength of the quadrupole, so magnetic tuning and

adjustment of the integrated quadrupole gradient will be done during the manufacture of the quadrupole, before it is installed.

The optical strength of the quadrupoles was one of the parameters that was optimized in order to minimize the power gain length. The value chosen is 0.112 m^{-1} for a beam of 14.35 GeV, but the minimum is very flat and a variation of up to 10% would not significantly affect the power gain length. When the LCLS is run at an energy other than 14.35 GeV (e.g., at 4.5 GeV), the strength of the quadrupoles will not be adjusted. At 14.35 GeV the averaged beta function is about 18 m, whereas at 4.5 GeV it is closer to 7 m.

Each quadrupole magnet is installed on slides so it can be moved, remotely, in both horizontal and vertical directions. This enables the quadrupoles to also serve as steerers. They will be used, along with the separate electromagnetic steerers, in the beam-based alignment procedure.

In the simulations that were run, the quadrupoles were placed in the middle of the break section. In the final mechanical design, the quads will be displaced to allow for optimal use of the break. Therefore, the final position of the quadrupoles will not be known until the mechanical design for the inter-undulator diagnostics is completed. However their relative separation will not change.

8.7.1 Quadrupole Mechanical Design

The space between undulator segments is very limited. The quadrupole design is very compact; the length is only 50 mm with an aperture of only 11.3 mm. The quadrupole assembly is shown in **Figure 8.25**.

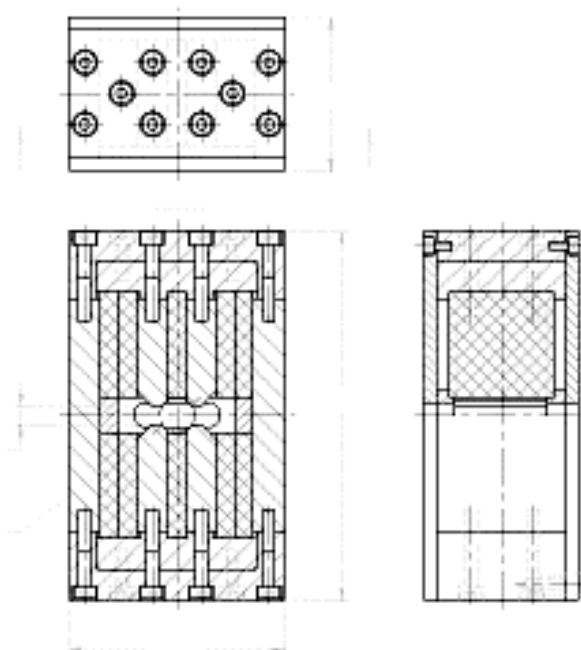


Figure 8.25 Sketch of the permanent magnet quadrupole. Ten identical permanent magnet blocks are used.

The quadrupole is designed in such a way that top and bottom halves of the assembly are symmetrical about the beam center. The outer housing of the assembly is fabricated from low carbon steel, thus providing a complete magnetic shield on all six sides. The top and bottom housing sections are fitted with aluminum inserts used to define the location of the magnets and poles. These sections, once fitted with the aluminum inserts, are precisely machined together side by side to ensure that the holders and inserts end up in the same plane. Similarly, the two carbon steel side shields are clamped together and precisely ground, thus creating two identical halves. As a result of this machining approach, the assembly, once bolted together, precisely defines the X and Y-dimensions (the Z-dimension is the beam direction). These in turn determine the gaps for the poles and magnets.

In the center of the four poles are the two central magnets. On the outside of each pole are pairs of magnets located side by side. Each of the magnets is slightly larger than the neighboring poles and overlaps the poles on three sides. All of the magnets in the assembly are the same size; thus, the outer magnet pairs are twice the thickness of the inner magnets.

Each end of the quadrupole assembly is fitted with a shield that has a 20-mm wide groove that allows insertion of a Hall probe for magnetic measurement purposes. The two side shields each contain a pair of precise holes in the median plane that are used to house standard tooling balls for alignment of the assembly in the beam line.

The quadrupoles are supported by the same Anocast[®] piers as the BPM modules but otherwise not coupled to them. Their transverse position (horizontal and vertical) can be remotely controllable by x,y-slides. The quadrupoles have a bore of 11.5 mm and thus provide plenty of aperture for the 6 mm OD vacuum chamber to fit without interference. There will be horizontal and vertical corrector coils connected to each quadrupole.

8.8 Vacuum Chamber

The undulator vacuum chamber is 120 meters long and must fit into the 6-mm undulator gap. The chamber will be segmented in the same way as the undulator with a diagnostics section between each undulator segment. It will be pumped by ion pumps at each diagnostics chamber. The diagnostics chambers need to be designed with a relatively smooth bore to minimize wakefields.

The proposed chamber through the undulator segments is formed from a stainless steel tube with copper plating on the inside to reduce the resistivity as seen by the beam. The following analysis shows that such a chamber can meet the LCLS requirements and withstand missteering events. It cannot withstand continuous missteering into the wall for extended periods of time. The Machine Protection System will prevent this.

8.8.1 Electron Beam Collimation and Vacuum Chamber Design

This section analyzes the vacuum chamber and magnetic material with regard to the need for protection from accidental electron beam losses and discusses the vacuum chamber surface roughness limits.

8.8.1.1 Beam Parameters Used in These Calculations

It is of vital importance to fully understand the consequences of exposure to the undulator to the primary electron beam. Of greatest concern is the response of the permanent magnet material and that of the undulator vacuum chamber to such events. The electron beam parameters (at injection into the undulator) and geometric dimensions that were used in the analysis are listed in **Table 8.6**.

Table 8.6 Parameters used in calculations of the effect of beam losses in the undulator.

Parameter	Value
Beam Energy	$E_o = 5\text{--}15 \text{ GeV}$
Bunch Charge	$Q = 1 \text{ nC}$ ($N = 0.625 \times 10^{10} \text{ e}^-/\text{bunch}$)
Repetition Rate	Pulse Repetition Rate, $\text{PRR} \leq 120 \text{ Hz}$
Average Power	$P_{av} \leq 1.8 \text{ kW}$
Beam Transverse Size	$\sigma \sim 32 \text{ }\mu\text{m}$
Magnet Gap	$g = 6.0 \text{ mm}$
Vacuum Chamber	$\text{OD} = 6.0 \text{ mm}$, $\text{ID} = 5.0 \text{ mm}$
Wall thickness	$t = 0.50 \text{ mm}$

8.8.1.2 Permanent Magnet Material

The material used for this analysis is neodymium-iron-boron (NdFeB) (2-14-1) and its material properties are listed **Table 8.7**

Table 8.7 Material Properties of neodymium-iron-boron (NdFeB) (2-14-1)

Property	Value
Modulus of Elasticity	$E = 1.5 \times 10^{11} \text{ N/m}^2$ ($21.74 \times 10^6 \text{ psi}$)
Poisson Ratio	$\nu = 0.3$
Tensile Strength	$\sigma_{UT} = 80 \text{ N/mm}^2$ ($11,600 \text{ psi}$)
Coefficient of Thermal Expansion	$\alpha_{ } = 3.4 \times 10^{-6}/^\circ\text{C}$ $\alpha_{\perp} = -4.8 \times 10^{-6}/^\circ\text{C}$ $E \alpha_{ } = 5.1 \times 10^5$ ($74 \text{ psi}/^\circ\text{C}$) $E \alpha_{\perp} = 7.2 \times 10^5$ ($104 \text{ psi}/^\circ\text{C}$)
Specific Gravity	$\rho = 7.4 \text{ to } 7.5 \text{ g/cm}^3$
Specific Heat	$c = 0.11 \text{ cal}/(\text{g}^\circ\text{C}) \equiv 0.46 \text{ Ws}/(\text{g}^\circ\text{C})$

Based on composition values and atomic weights of the constituents, the effective values of radiation length, atomic number, and material critical energy of the material are: $X_o = 11.54$ g/cm²; $X_o/\rho \sim 1.55$ cm; $Z \sim 29$; $\epsilon_o \sim 17.3$ MeV respectively. The minimum ionization loss is $dE/dx = \epsilon_o/X_o \sim 1.5$ MeV/(g/cm²). Note: these values very closely match those of copper.

For a square hit up front with no shower multiplicity (i.e., $\Pi(e^-) = 1$), the normalized power deposition is $P' \sim 1.35$ W/cm. For the highest envisioned incident beam energy of 15 GeV, shower maximum of the electromagnetic cascade occurs at a depth of $T_{max} \sim 5.8$ cm $X_o \equiv 9.0$ cm, and the maximum shower multiplicity is $\Pi_{max}^{(e^-)} \sim 106$ [14]. Consequently, the maximum normalized power deposition is $P'_{max} = P' \Pi_{max}^{(e^-)} \sim 145$ W/cm.

First, the exposure at the undulator entrance is estimated where the assumed Gaussian distributed beam has a predicted transverse size of $\sigma = 32$ μ m. Assuming a uniform particle distribution inside $0 < r \leq \sigma$, a heat source term is defined as $S = CP'/A_b \sim 16.5 \times 10^3$ W/cm³, where $C \sim 0.4$, and $A_b = \sigma^2 \pi \sim 32.2 \times 10^{-6}$ cm². For a specific heat capacity of $\rho c = 3.43$ Ws/(cm³°C), the temperature rise per pulse (RF-bunch) for a pulse repetition rate (PRR) = 120 Hz is

$$\Delta T = \frac{S}{\rho c PRR} \approx 40^\circ \text{ C/pulse.} \quad (8.31)$$

The consequential thermal stresses are proportional to the product of the coefficient of thermal expansion α and the modulus of elasticity E :

$$\sigma_{th} \propto E \alpha \Delta T. \quad (8.32)$$

Numerically σ_{th} is $\sim 2.83 \times 10^7$ N/m² (4100 psi or $\sim 0.35 \sigma_{UT}$) for a fully restrained body. Since this is near a surface, actual stresses are somewhat lower. This should not present any structural challenge to the magnetic material, even for repeated exposures. At T_{max} the effective transverse beam size increases to $\sigma_{eff} \sim 220$ μ m (from Monte Carlo simulations for copper and scaling.). Using $\Pi_{max}^{(e^-)} = 106$, the heat source term is $S \sim 37$ kW/cm³, and the resulting single pulse temperature rise is $\Delta T \sim 90^\circ$ C/pulse.

Somewhat higher temperatures are actually observed short of T_{max} , at a depth of ~ 3.5 to $4 X_o$ for $E_o = 15$ GeV, since the expanding transverse shower has not yet caught up with the rapidly increasing shower multiplicity. At $4 X_o$, σ_{eff} is ~ 130 μ m and $\Pi(e^-)$ is ~ 75 . The resulting effective heat source term is $S_{4X_o} \sim 73$ kW/cm³, for which the temperature rise per pulse is

$$\Delta T \sim 175^\circ \text{C/pulse,} \quad (8.33)$$

and the consequential thermal stress rise is of the order of σ_{th} is $\sim 1.24 \times 10^8$ N/m² (18,000 psi or $\sim 1.6 \sigma_{UT}$).

The permanent magnet material must therefore be protected from direct hits by the electron beam. The material is a powder-metallurgical product and is quite brittle, i.e., has very low ductility, and exposure to one pulse might fracture it. Independent of structural concerns, temperature changes of this magnitude would cause permanent changes in the remanent magnetic field, which are not acceptable.

Since the magnetic material has atomic properties very similar to copper, neither copper nor materials with equal or higher atomic number are suitable as primary collimator materials. The primary material must be protected by a low-Z material like titanium.

8.8.1.3 Undulator Vacuum Chamber

There are two distinctly different beam exposure scenarios for the undulator vacuum chamber. The first is direct e⁻-beam exposure at the entrance to the undulator with the momentum vector approximately parallel to the undulator and vacuum chamber axis (this assumes that no collimator is in place). The second exposure scenario results from excessive beam deflection inside the undulator resulting in the beam impinging at shallow angles onto the vacuum chamber. Selection of an appropriate material for the vacuum chamber involves tradeoffs between physics performance, survival during direct primary beam exposure, and ease of manufacture, and thus economics. Physics performance dictates a chamber material of low electrical resistivity, at least on the inside surface, to keep the resistive wall wake function at acceptable levels. Materials like copper and aluminum are good choices.

Long-term survival against direct hits by the e⁻-beam requires a low-Z material with good strength and endurance characteristics. Titanium and some of its alloys, as well as some aluminum alloys, are good choices. Since the undulator and its vacuum chamber are ~100 m long, the chamber needs to be built in segments (anticipated modular length ~3.4 m) and joined by vacuum flanges and bellows. The materials mentioned above are technically feasible to use, but they also present fabrication, installation, and economic challenges. Copper, aluminum, titanium, and stainless steel were evaluated for possible use as vacuum chamber material. Stainless steel is the final choice, and an analysis of its response to the two exposure scenarios is presented below. Cost effective manufacturing, ease of installation, and maintenance for ultra-high vacuum make stainless steel a first choice, but at the expense of high electrical resistivity. This handicap can be compensated by surface coating with a low resistivity material.

8.8.1.4 Beam Strikes at the Entrance to the Vacuum Chamber

Using the minimum ionization loss and no shower multiplicity ($\Pi^{(e^-)} = 1$), the power deposition at normal incidence to the chamber is

$$P' = (-\rho dE/dx) N \times 1.6 \times 10^{-19} PRR = 11.6 \times 10^6 \times 0.625 \times 10^{10} \times 1.6 \times 10^{-19} \times 120 = 1.4 \text{ W/cm} \quad (8.34)$$

using dE/dx for iron to approximate stainless steel.

Next, again assuming a Gaussian beam intensity distribution with $\sigma \sim 32 \mu\text{m}$, and also assuming uniform intensity within the radial interval $0 < r \leq \sigma$, the heat source term becomes $S \sim 17 \text{ kW/cm}^3$. The temperature rise per single rf-bunch follows as $\Delta T = 17 \times 10^3 / (4 \times 120) \sim 35^\circ\text{C}$. The resulting thermal stresses are $\sigma_{th} \sim 8.63 \times 10^7 \text{ N/m}^2$ (12,500 psi) for a fully restrained body. Thin-walled tubing and beam exposure near the surface (inside or outside) will remove some of these restraints and thereby reduce the magnitude of these stresses at the expense of increased elastic strain. The endurance limit for the type of stainless steel used for vacuum chamber tubing (300 Series) is $\sigma_{End} \sim 1.73 \times 10^8 \text{ N/m}^2$ (25,000 psi), and there would be no problem for this level of beam exposure. The yield strength $\sigma_y \sim \sigma_{th}$ is $\sim 2.07 \times 10^8 \text{ N/m}^2$ (30,000 psi) is also significantly above the exposure stress, and no plastic, permanent deformations would occur.

8.8.1.5 Beam Strikes Inside the Undulator

Once inside the undulator, the electron beam can experience additional deflections. Based on alignment considerations for both the undulator and the quadrupoles, it is desirable to have a dynamic range of $\pm 500 \mu\text{m}$ at each magnet mover. For an assumed maximum quadrupole gradient of 105 T/m and an effective magnetic length of $l_{eff} = 5 \text{ cm}$, the maximum kick angle becomes $50 \mu\text{rad}$. The present design value of the center-to-center module length is 3.4 m. The deflection at the end of one modular section is therefore $170 \mu\text{m}$. The vacuum chamber inside diameter is 5.0 mm. It can readily be shown that five consecutive maximum kicks will amount to a deflection of $\sim 2.6 \text{ mm}$ and the beam could strike the chamber wall near the end of undulator segment 5 with a maximum angle of $\theta \sim 300 \mu\text{rad}$ (see **Figure 8.26**). The shortest longitudinal distance, l_i , over which the 2σ core of the incident Gaussian distribution could strike the vacuum chamber is then $l_i = 2\sigma/\theta = 21.3 \text{ cm} \equiv 13 X_o$ for stainless steel with $1 X_o \sim 1.66 \text{ cm}$. Similarly, the shortest distance of the momentum vector traversing the vacuum chamber wall is $l_t = t/\theta = 167 \text{ cm} \equiv 100 X_o$. This means that every conceivable e^- energy envisioned for the undulator reaches the peak of the electromagnetic cascade inside the vacuum chamber wall, and also, with the exception of particles scattered out of the wall in the transverse direction, the chamber wall is almost a complete absorber of the cascade. Examining the region of shower maximum where the normalized power deposition varies little ($dP/dT \sim 0$) and using the longitudinal interval of $T_{max} \pm 1 X_o \equiv 4.5$ to $6.5 X_o \equiv 3.3 \text{ cm}$, Monte Carlo simulations using the EGS code show that $\sim 0.23 P_{av}$ is absorbed in this region. The volume element defined by 2σ and $\pm 1 X_o$ is a “skewed” ellipsoid, and after folding in a double convoluted Gaussian, the expected power deposition is $P_{4.5-6.5 X_o} \sim 0.23 CP_{av} = 0.23 \times 0.4 \times 1.8 \times 10^3 \sim 165 \text{ W}$. Let $\Delta\sigma$ be the average transverse increase in σ at the depth location of the ellipsoid; then the two axes are $(l_i + 2\Delta\sigma \sim l_i \sim 21.5 \text{ cm})$ and $(2\sigma + 2\Delta\sigma \sim 0.27 \text{ cm})$. The effective volume of the ellipsoid is then $V = A_{eff} h \sim [(l_i + 2\Delta\sigma) (2\sigma + 2\Delta\sigma) \pi/4] 2X_o \sim [21.5 \times 0.27 \pi/4] 2 \times 1.66 \times 300 \times 10^{-6} \sim 4.54 \times 10^{-3} \text{ cm}^3$.

Before arriving at a heat source term S , allowance has to be made for transverse leakage of shower particles out of the chamber wall. Monte Carlo calculations of a beam impinging in the center of a thin-walled stainless steel tube of similar wall thickness (1.27 mm) with the momentum vector parallel to the tube axis have been made. These resulted in volumetric power deposition values approximately a factor of 3.5 lower than those found for a semi-infinite

medium of the same material (E_o was 50 GeV and $\sigma = 100 \mu\text{m}$ for the tube and $200 \mu\text{m}$ for the semi-infinite medium). Then $P_{4.5-6.5X_o} \sim 40 \text{ W}$. The heat source term for assumed uniformly distributed heat sources is then

$$S_{eff} = P_{eff} / V \sim 9\text{kW/cm}^3 \quad (8.35)$$

and the temperature rise per pulse for stainless steel with $\rho c = 4 \text{ Ws}/(\text{cm}^3\text{C})$ is

$$\Delta T_{pulse} = S_{eff} / (\rho c PRR) \approx 20^\circ \text{ C} . \quad (8.36)$$

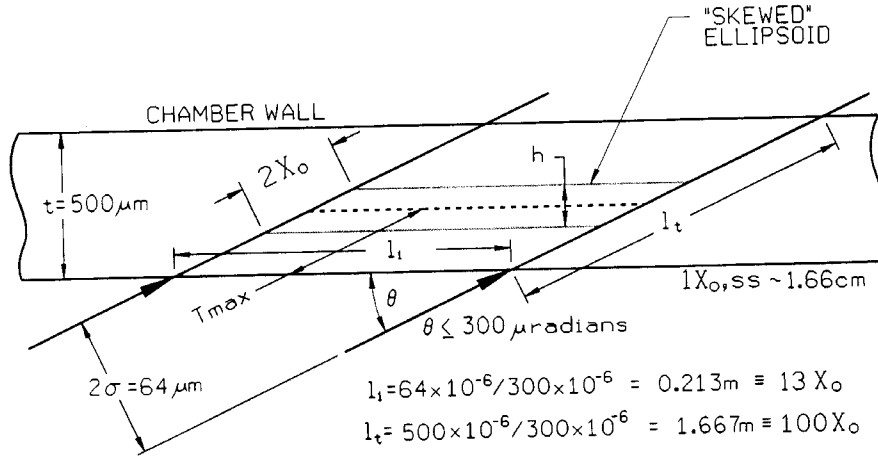


Figure 8.26 Model of accidental exposure of vacuum chamber to electron beam.

The consequential thermal stress spike in a fully restrained body would be about $\sigma_{th} \sim 4.55 \times 10^7 \text{ N/m}^2$ (6600 psi). Since a thin-walled tube is not very restrained, actual stresses would be even lower. Both pulse temperature rise and thermal stress are very modest; and one could comfortably manage even 2nC per pulse.

Next the steady state conditions are evaluated for when the beam is accidentally “parked” on the chamber for a long time. The effective power is converted into a heat load per unit length based on the distance of impingement, l_i . Then $P'_{eff} = P_{eff}/l_i = 40/21.5 \sim 2\text{W/cm}$. Assume a hypothetical heat sink at $\pi = 180^\circ$ from the line source. Then the azimuthal conduction heat flux in the tube is $q''_c = P'_{eff} / 2t = 2/(2 \times 0.050) \sim 20 \text{ W/cm}^2$. Ignoring natural convection and thermal radiation losses for the moment, the maximum temperature difference over π , i.e., $\delta = r\pi = 0.864 \text{ cm}$ and for a thermal conductivity of $k = 0.165 \text{ W}/(\text{cm}^2\text{C}/\text{cm})$ is $\Delta T = q''_c \delta / k = 20 \times 0.864 / 0.165 \sim 105^\circ \text{ C}$. This difference is modest, and to first approximation, a uniform temperature can be assumed for heat rejection by thermal radiation over the entire surface of the longitudinal section of chamber under consideration. The radiation heat flux is then $q''_r = P_{eff} / \pi d = 2/(0.06\pi) \sim 1.06\text{W/cm}^2$. For stainless steel tubing, the thermal emissivity is $\varepsilon \sim 0.1$ of black body. Solving the Stefan-Boltzmann equation for the surface temperature of the tubing, for black body radiation

to an ambient temperature $T_a \sim 300 \text{ K} \equiv 27^\circ\text{C}$, one finds $T_s = (q_r'' / \varepsilon\sigma + T_a^4)^{1/4} = 1345 \text{ K} = 1072^\circ\text{C}$.

Even if one factored in a small reduction due to the contribution of natural convection, steady state temperatures of this magnitude are too high for the stainless steel chamber and for the adjacent permanent magnet material. The MPS system will detect such an errant beam condition and rate-limit the beam

In addition to stainless steel, three other potential magnet vacuum chamber materials were analyzed. Aluminum was found to comfortably withstand the consequences of single rf-bunch hits; but for continuous exposure to a 1.8 kW beam, the steady state temperature exceeds the melting point. OFE copper was found to be able to take individual bunch hits but was marginal for repeated exposure at the same location; i.e., single bunch thermal stresses were modestly above the endurance limit. Continuous beam exposure resulted in steady state temperatures near the melting point, and this material is not suitable for a vacuum chamber. Early detection of errant beam would remove this handicap for both copper and aluminum. A proposed ceramic (Al_2O_3) vacuum chamber concept has also been analyzed. Single pulse temperature and stress rises were modest, and the steady state temperature was well within the capability of this material. When compared to stainless steel, neither of these materials was cost effective; and the ceramic chamber presented additional engineering challenges.

In summary, the proposed stainless steel vacuum chamber can comfortably accept missteered beam pulses inside the undulator and will not suffer any damage for $\sigma \geq 32 \mu\text{m}$ and $P_{av} = 1.8 \text{ kW}$. However, a continuous beam exposure must be detected and beam delivery terminated before significant temperature increases in the chamber and adjacent magnetic material occur.

8.8.1.6 Adjustable Collimators to Protect Undulator and Vacuum Chamber

The analysis of various collimator concepts resulted in selection of a jaw design with multiple materials. For many reasons, such as fabrication, water-cooling, compactness, etc., it is still highly desirable to use copper as the primary power absorber material. For fully annealed OFE copper to withstand the exposure to a very large number of pulses, the cyclic thermal stresses should not exceed 3.45 to $4.15 \times 10^7 \text{ N/m}^2$ (5000 to 6000 psi). Working backwards, the effective transverse beam size for an assumed Gaussian distributed beam should be $\sigma \geq 50 \mu\text{m}$ at the beam entrance face of a copper collimator jaw where $\Pi(e^-) = 1$. But the transverse beam size at that location is only $\sigma \sim 38 \mu\text{m}$. To guarantee long term survival of the copper, the transverse beam size must be increased. Using a spoiler of a lower Z material with appropriate mechanical properties is a simple and passive method of achieving this goal. In the past a titanium alloy (Ti-6Al-4V) has been successfully used for this purpose. Modeling with the Monte Carlo code EGS resulted in a minimum spoiler thickness required of $\sim 0.3 X_o$. This will protect the front part of the copper near the interface with the titanium. However, the region of the highest power density and therefore temperature rise for the beam energies of interest and for copper is at a depth of $\sim 3 X_o$. Since there is significant shower multiplicity to that depth without a commensurate transverse spread of the beam, the minimum size of the beam needs to increase to $\sigma \sim 160 \mu\text{m}$ at the front

face of the jaw. A spoiler of thickness $\sim 1 X_o$ ($\equiv 3.77$ cm) will do the job. The shower multiplicity in the titanium alloy at that depth is $\Pi(e^-) \sim 6$. The effective heat source term is $S_{1 X_o} \sim 4500$ W/cm³, the resulting single pulse temperature rise for the standard beam parameters is $\Delta T_{pulse} \sim 11^\circ\text{C}$, and the consequential thermal stress rise is $\sigma_{th} \sim 2.14 \times 10^7$ N/m² (3100) psi $< \sigma_{End}$. At a depth of $3 X_o$ (i.e., $1 X_o$ Ti + $2 X_o$ Cu), $\Pi(e^-)$ is ~ 45 and σ_{eff} is ~ 310 μm . Then the heat source term becomes $S_{3 X_o} \sim 9$ kW/cm³, $\Delta T_{pulse} \sim 22^\circ\text{C}$, and $\sigma_{th} \sim 4.28 \times 10^7$ N/m² (6200) psi $\sim \sigma_{End}$. This is acceptable for long term operation. The spoiler thickness can be increased even more, but it would be at the expense of more power deposition in the titanium jaw, which has poor thermal conductivity. The Ti-slab can be mechanically attached directly to the entrance face of the copper block.

The steady state power deposition into $1 X_o$ of Ti is $P \sim 6$ W and can be conducted into the copper. The copper block needs to be water-cooled. To completely attenuate and absorb a 15 GeV cascade shower, a total jaw length of $\sim 30 X_o$ is recommended. However, most of the power has been absorbed after $\sim 15 X_o$, and one could switch to a higher Z material at that depth and keep the assembly compact. The recommendation is to have a jaw composed of $1 X_o \equiv 3.77$ cm Ti-6Al-4V, followed by $14 X_o$ Cu $\equiv 20.23$ cm, and completed with $15 X_o$ W $\equiv 5.16$ cm for a total length of $30 X_o \equiv 27.2$ cm $\equiv 10.7$ inch. Here W stands for preferably W-26Re or a free-machining tungsten composite with good ductility. The transverse size should be of the order of 8 cm \times 8 cm. Only the copper section of the jaw would be water-cooled. A flow rate of ~ 0.5 to 1 gpm is recommended. Such jaws could be mounted to standard SLAC collimator designs with only minor modifications.

8.8.1.7 Fixed Aperture Protection Collimators

Since the undulator represents such a large investment and is the centerpiece of the whole LCLS, it is prudent to back up the adjustable collimators with an additional fixed aperture protection collimator just ahead of the entrance to the undulator. Such a collimator could be made of copper or even tungsten (if space were at a premium), would not have to be water-cooled, and would be a sacrificial device since exposure to primary beam would be an accidental occurrence. The aperture of the collimator would need to be less than the inside diameter of the vacuum chamber (ID = 5 mm), and its length should be 25 to $30 X_o$ (~ 36 to 44 cm) with sufficient transverse size to shadow all of the undulator structure. Its presence would also reduce exposure of the undulator to scattered radiation from the many possible sources in the e^- -beam transport system.

Additional fixed aperture collimators need to be placed in the transport system at strategic locations for equipment protection reasons. They should be patterned after the FFTB protection collimator design and can be either copper if $\sigma \gtrsim 50$ μm or must have a titanium insert (like Ti-6Al-4V) in locations where $\sigma < 50$ μm .

8.8.1.8 Vacuum Chamber Surface Roughness

Recent computer modeling [15] (Section 8.9.5) gave indications that the surface roughness on the inside of the undulator vacuum chamber may have deleterious effects on beam quality.

Two effects, namely the geometric wall wakefield and the resistive wall wakefield, can negatively influence beam performance. The 6 mm OD \times 5 mm ID stainless steel tubing needs to have a small surface roughness. Various roughness-reducing procedures have been investigated. The semiconductor industry has an ongoing need for ultra pure gas transport systems, and much R&D effort was invested in recent years to satisfy these demands. Present state-of-the-art technology identified fully austenitic stainless steel Type 316-L with very stringent chemical composition limits as a successful starting material. It is extruded into seamless tubing with special high quality dies, to great straightness, and under very clean conditions. The tubing is then cleaned and electropolished in lengths up to 6 m. Tubing with a surface roughness of $R_a \sim 125$ nm (rms) is readily available off the shelf and for modest cost. Flat surfaces are readily electropolished to $R_a \sim 50$ nm, and such a value might also be achievable inside a tube with more R&D effort. Another quantity in surface roughness evaluation is the total peak-to-valley depth of roughness, R_t or R_{max} , which varies from 4 to 12 times the R_a value.

An R&D program is underway at SLAC/SSRL to use such high quality industrial tubing as starting material and then improve the surface quality to $R_a < 100$ nm (rms) by further electropolishing. The best results to date from small samples (12 to 15 mm long \times 5 to 6 mm wide) cut out at random locations from 0.5 m long tubing sections showed R_a values from a best of 10 nm to the 50 nm (rms) range. The azimuthal values were always somewhat lower than the longitudinal ones. The measurements were made with an atomic force microscope and distances traversed with the stylus were ~ 55 μ m azimuthally and ~ 70 μ m longitudinally. It appears that the surface quality of the commercial products can be significantly improved to achieve values of surface roughness that will not negatively impact the performance of the LCLS undulator. Electro-polishing 3.4 m long tubing sections will, however, present additional challenges.

Since stainless steel has a high electrical resistivity, the resistive wall wake is increased. To reduce this effect, a thin layer of copper ($>$ skin depth) is deposited onto the highly electro-polished surface using a thin nickel substrate for better adhesion. This process is then followed by further electro-polishing the copper surface. Best values achieved to date are $R_a \sim 120$ nm (rms), but further refinements in the process are possible and should make the surface inside the undulator vacuum chamber smooth enough that it does not materially degrade the electron beam.

8.8.2 Vacuum System Requirements and Description

The vacuum system for the undulator must have the following attributes to provide a good environment for the electron and photon beams:

- The vacuum system components must provide low impedance to avoid producing beam instabilities and minimize higher-order mode heating.
- Adequate pumping must be provided to maintain a low beamline pressure ($< 10^{-7}$ Torr average).
- The beamline must provide an adequate aperture for the electron and photon beams.

The LCLS beam pipe is a 6 mm outside diameter, 0.5 mm thick wall stainless steel (type 316-L) tube. The interior surface of the tube will be plated with approximately 0.01 mm of OFE copper to minimize ohmic heating from the image current induced by the electron beam. The beam pipe is constructed in segments that are 3.42 m long and which correspond to the undulator magnet segments. The beam pipe segments are constructed from type 316-L stainless steel to minimize the magnetization of the heat-affected zone at the welds. After welding, each beam pipe section will be annealed to completely de-magnetize the welds. Vacuum processing of the vacuum tubes section will consist of baking at 200°C for a minimum of 4 hours.

Between undulator segments there are short gaps of 18.7 and long gaps of 42.1 cm every third segment where vacuum pumping, beam steering, and diagnostic components are located. A typical segment gap is shown in **Figure 8.27**.

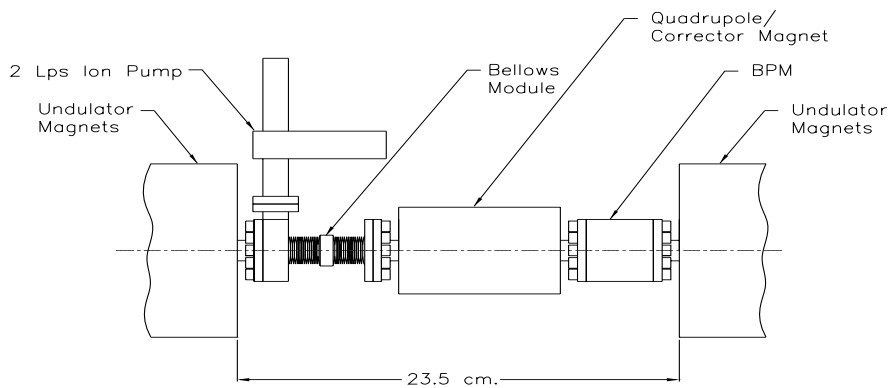


Figure 8.27 Undulator segment gap with vacuum and magnet components.

Between each undulator segment, there is an rf shielded bellows module. The purpose of the bellows is to provide flexibility for ease of installation of adjacent segments of the beam pipe and to account for any minor length changes due to temperature fluctuations. A cross-section of the LCLS bellows module is shown in **Figure 8.28**. Since space is tight, vacuum pumping of the beam pipe is accomplished within the bellows module. A 2 l/s noble diode ion pump is mounted on one of the bellows end flanges. Pumping occurs through ten 1-mm diameter holes in the beam pipe. Conductance losses through the module decrease the actual pumping speed to approximately 1 l/s.

The sliding rf fingers within the bellows are fabricated from a thin wall type 316-L stainless steel tube. The ends of the tube have 0.15 mm slits, which allow the tube to flex radially and provide spring force to maintain contact with the adjacent tubes. The tube slits are plated with 0.01 mm thick silver. The contacting surfaces of the adjacent tubes are plated with 0.01 mm thick rhodium. The combination of the relatively soft silver and the hard rhodium provide a sliding surface with both good lubricity and good electrical conductivity.

The flanges in the vacuum system are raised face type using a “VAT” style seal. The VAT seal is a commercially available, silver-plated, soft copper gasket. The gasket has a raised bead

around the inside diameter of the beam tube, which is crushed between the flanges. The raised bead acts as the RF seal across the flanged joint.

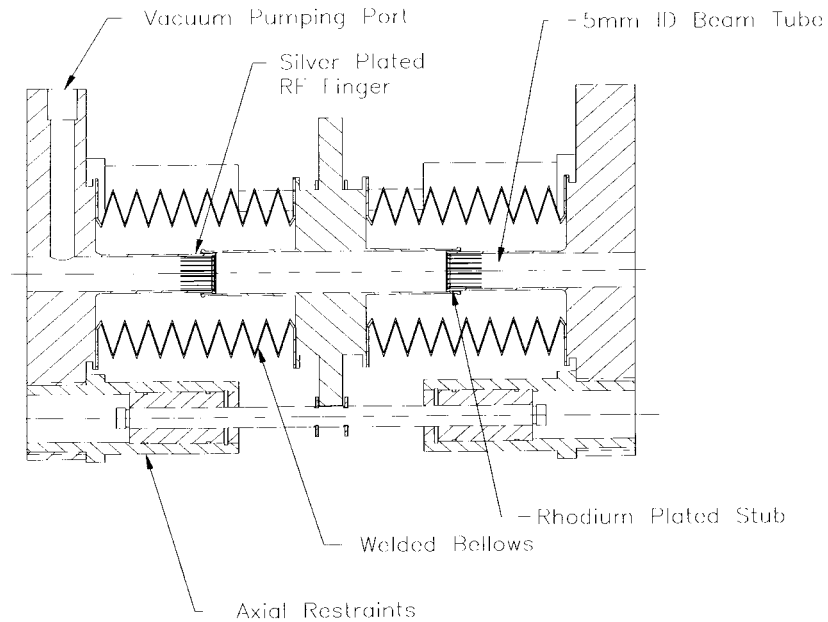


Figure 8.28 Bellows module cross-section.

8.8.3 Gas Load and Vacuum Pressure

In general, accelerator beam pipes are conductance-limited. In the case of the undulator vacuum system, this problem is extreme. It turns out that the amount of pumping at 3.42 m intervals has little effect on the average system pressure. This can be demonstrated with a simple calculation. Assuming a constant gas load along the length of the beam pipe and considering the symmetry of the vacuum system, the average beam pipe pressure is calculated analytically using the following equation:

$$P_{av} = \left(q \frac{pL}{C} \right) \left(\frac{C}{S} + \frac{1}{3} \right) \quad (8.37)$$

- where
- P_{av} , average pressure, Torr
 - q , H₂ gas load = 1×10^{-11} Torr-liter/sec-cm²
 - p , circumference = $\pi(5 \text{ mm}) = 1.57 \text{ cm}$
 - L , half-length of segment = 171 cm
 - C , beam pipe conductance = 0.0269 liter/sec
 - S , pumping speed

Assuming a pumping speed of 1 l/s, the average pressure is 3.59×10^{-8} Torr. If the pumping speed is increased to 10 l/s, the average pressure decreases to 3.34×10^{-8} Torr (only a 7.6% improvement). From this, it can be seen that minimizing the gas load has a much greater effect on beam pipe pressure than does pumping speed. The gas load within the undulator vacuum system comes from two processes, thermal desorption and photo-desorption. Thermal desorption is common to all types of vacuum systems; it is the heat-stimulated release of gas constituents adsorbed on the walls of the system. Photo-desorption is the outgassing that occurs due to synchrotron radiation hitting the walls of the beam pipe and desorbing gas molecules. Good thermal desorption data exists for UHV processed copper plated stainless steel from the PEP-II project [16,17]. Typically, $q_t = 5 \times 10^{-13}$ Torr-liter/sec-sq cm (@ T = 20°C) after a 200°C bake for 4 hours. Since the undulator vacuum system is expected to operate at 20 °C, this value will be used.

Photodesorption is a little harder to estimate. The undulator produces 90 GW of total peak power. Photon flux is estimated using 100 GW of power hitting the walls of the vacuum system using the following formula:

$$N_{\gamma} = \frac{P_{SR} t f (6.242 \times 10^{15} \text{ keV/J})}{E_{\text{photon}}} \quad (8.38)$$

- where
- N_{γ} , photon flux = photons/sec
 - P_{SR} , synchrotron radiation power = 100×10^9 Watts
 - t , pulse length = 100×10^{-15} sec
 - f , pulse frequency = 120 sec^{-1}
 - E_{photon} , average photon energy = 200 keV/photon

N_{γ} for the undulator is 3.74×10^{13} photons/sec. The distribution of the spontaneous photon flux is assumed to increase linearly along the length of the vacuum system as shown in **Figure 8.29**.

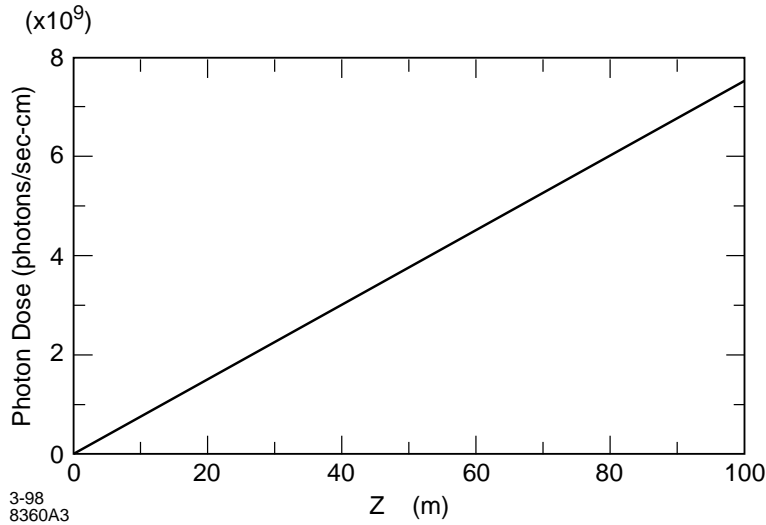


Figure 8.29 Undulator photon flux profile.

The photo-desorption gas load is calculated as follows:

$$q_p = N_\gamma \eta (2.83 \times 10^{-20} \text{ Torr-l/molecule}) \quad (8.39)$$

where q_p , photo-desorption gas load = Torr-liter/sec

η , photo-desorption rate = molecules/photon

Photo-desorption of copper and stainless steel beam tubes were investigated in the past. Brookhaven National Laboratory conducted studies for the PEP-II Project, determining the values of η with respect to flux [18]. The photon flux for the undulator vacuum system is in fact quite low, so, realistically, photon scrubbing will not occur during the lifetime of the machine. From the Brookhaven results, it has been determined that an $\eta = 5 \times 10^{-3}$ molecules/photon is appropriate for design purposes. Using this value, the photo-desorption profile is calculated and is shown along with the calculated thermal desorption profile in **Figure 8.30**.

Using the desorption profiles, a vacuum pressure profile for the 100-m long undulator vacuum system is calculated using VACCALC [19], a pipeline pressure computer code. The entire undulator beam pipe is modeled using discrete pipeline segments. Each segment is defined by its length (m), conductance (l/s), gas load (nTorr-l/s), and pumping speed (l/s). All values for conductance, gas load and pumping speed are calculated for “hydrogen.” **Figure 8.31** shows the pressure profile along the length of the undulator vacuum system, with its average pressure being 1.06×10^{-9} Torr (1 nTorr). This is well below the design requirement of 10^{-7} Torr.

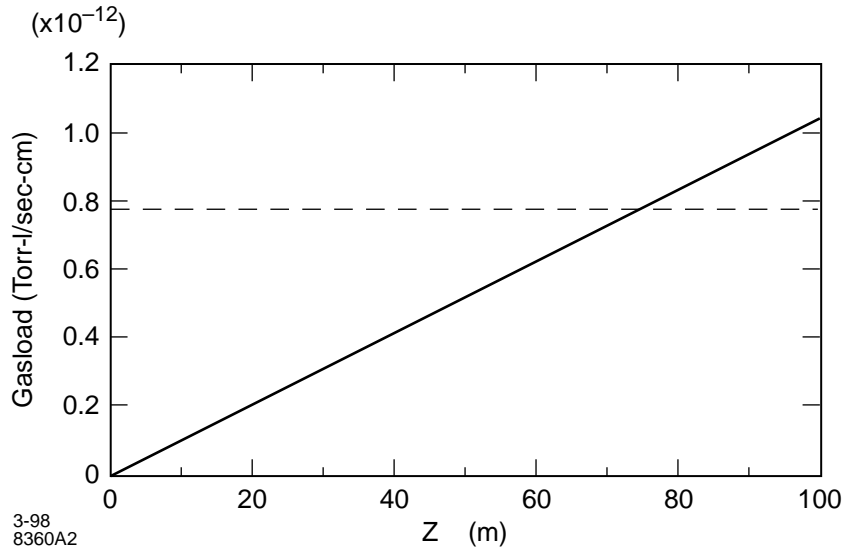


Figure 8.30 Undulator thermal and photo-desorption profiles.

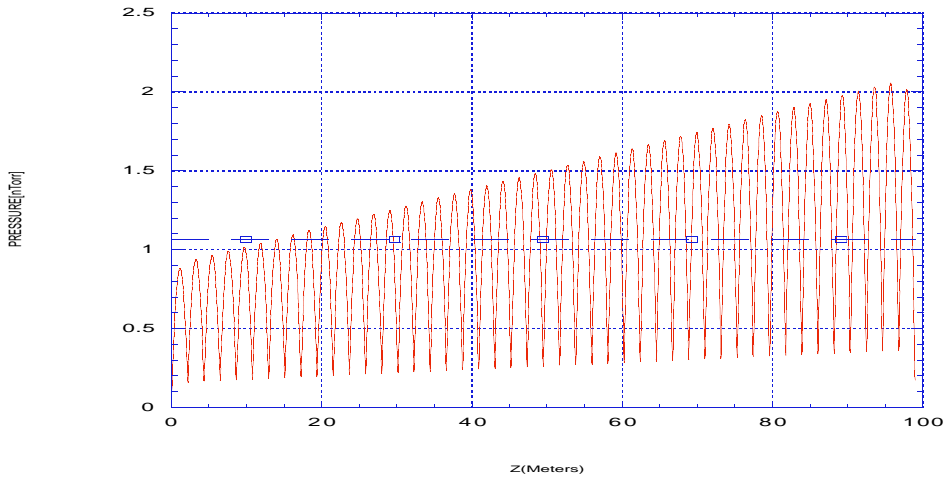


Figure 8.31 LCLS vacuum pressure profile.

8.8.4 Thermal Considerations

As described above, 100 GW peak of synchrotron radiation power strikes the walls of the beam pipe in the worst case scenario. However, the length of the photon pulse is 70×10^{-15} sec rms and the frequency of the pulse is 120 Hz. Therefore, the total power absorbed by the entire 121 m of beam pipe is 1.2 Watts. With such a low level of incident power, there is no need to actively cool the vacuum chamber.

8.9 Wakefield Effects in the Undulator

8.9.1 Introduction

When the electron beam moves through the undulator it will excite longitudinal and transverse wakefields due to the resistance and the discontinuities in the beam tube wall. Let us assume that the wall geometry is cylindrically symmetric. Then the longitudinal (monopole) wakefield will generate an energy loss and an increase in energy spread independent of the beam orbit, and the transverse (dipole) wakefield will generate an emittance growth that does depend on the orbit. It is, however, important to recognize that the forces due to the wakefields are correlated with longitudinal position. Assuming the bunch is composed of many slices at different longitudinal positions, the wakefields affect only the centroid values of the slices — i.e., the average energy and the average position of the slices in, respectively, the longitudinal and the transverse case. The distributions of the slices about their centroids are not affected.

The critical issues concerning the electron beam with respect to wakefield effects in the undulator are:

- The absolute value of the maximum relative energy deviation of a bunch “slice” (slippage length: $\sim 0.5 \mu\text{m}$) with respect to the mean of the whole bunch generated over the length of the undulator at 14.3 GeV should be less than $\sim 0.1\%$. This tolerance is derived from GINGER simulations.
- The dilution of the “projected” emittance (emittance projected over the entire bunch) should not exceed $\sim 10\%$.
- The mean energy loss over the undulator, including radiation losses, will determine the necessary taper of the magnetic fields of the undulator dipoles.

Since undulator wakefields have very little effect on the “slice” energy spread and the “slice” emittance, these tolerances are not considered here.

In this report the longitudinal and transverse wakefield effects on the LCLS beam during its time in the undulator are estimated to see how well these conditions are satisfied. Note that the beam dynamics and wakefield concepts that are presented are thoroughly discussed, with equations in [20].

8.9.2 Wakefield Induced Beam Degradation

In the longitudinal case, the wake function for a Gaussian bunch, from which the average wake (also known as the loss factor) $\langle W_z \rangle$ and the rms deviation of the wake with respect to the mean, $(W_z)_{rms}$ (the units are V/C/m) are derived, is first obtained. Then the wakefield induced energy loss is given by

$$\langle \delta \rangle = -\frac{e^2 N L \langle W_z \rangle}{E}, \quad (8.40)$$

with N the number of particles in the bunch, L the length of travel, and E the beam energy. The rms energy spread, with respect to the mean, becomes

$$\sigma_{\delta} = \frac{e^2 NL \langle W_z \rangle_{rms}}{E}. \quad (8.41)$$

In the transverse case, the average of the transverse wakefield of a Gaussian bunch $\langle W_x \rangle$ (here in units of V/C/m²) is first obtained. The focusing lattice in the undulator is a FODO type with a phase advance of 13°/cell at 14.3 GeV, and therefore a smooth focusing analysis is appropriate. First, to study the effect of injection jitter, the wake function is applied to obtain the projected emittance growth due to a betatron oscillation in the undulator. The offset at the end of the undulator, averaged over the bunch, can be written as

$$\langle x \rangle = x_0 e^{iL/\beta} (1 - i\nu), \quad (8.42)$$

with x_0 the initial offset, β the beta function, and ν the strength parameter (as long as it is small). The strength parameter is given by

$$\nu = \frac{e^2 NL \langle W_x \rangle \beta}{2E}. \quad (8.43)$$

The relative emittance growth, if it is small, is then given by

$$\frac{\Delta \varepsilon}{\varepsilon} = \frac{x_0^2 \nu^2 \gamma}{2 \varepsilon_N \beta}, \quad (8.44)$$

with γ the energy factor and ε_N the normalized emittance. If the beam tube wall is not perfectly straight and aligned then even if the beam does not undergo betatron oscillations the projected emittance can grow. However, unlike in the case of injection jitter, since this error is a static error some correction can usually be performed to reduce the effect. The misalignment errors are divided into two types, those that are uncorrelated to each other and those that are correlated. In the former category suppose the wakefield generating object is composed of M_p equal, randomly misaligned pieces. Then the emittance growth will again be approximately given by **Eq. (8.44)**, but with x_0 replaced by the rms misalignment of the pieces divided by the factor $M_p^{1/2}$. For correlated errors, the largest effect, for a given misalignment amplitude, is when the misalignment varies as $\cos(z/\beta)$, and the results are the same as given in **Eq. (8.44)**, but with x_0 representing the misalignment amplitude. If the oscillation frequency of the misalignments differs from the betatron wave number by Δk then the effect on emittance decreases according to $\text{sinc}^2(\Delta k L)$.

The above effects are due to a resonance term in the equation of motion. But there is normally also a bounded, non-resonance term. For example, consider the case where the beam's trajectory follows the magnetic focusing axis in the undulator, but this axis is not aligned with the axis of the impedance generating objects. In this case the projected emittance of the beam will grow and then again decrease within the undulator. Even though the final emittance growth in the LCLS undulator due to this effect is small, there may be a tolerance for bunch emittance growth anywhere within the undulator. In such a case this effect will set a tolerance for the alignment of the wakefield generating axis with respect to the magnetic axis. For this example, the maximum

emittance growth is given by **Eq. (8.44)**, with x_0 the distance between the two axes and with $\nu = 2e^2N\langle W_x \rangle \beta^2/E$.

In the calculations below, the following bunch and machine properties are considered: total charge of 1 nC, rms bunch length $\sigma_z = 20 \mu\text{m}$, normalized emittance $\epsilon_N = 1.0 \text{ mm-mrad}$ (the undiluted emittance is used for a conservative estimate), and energy $E = 14.3 \text{ GeV}$. The length of the undulator is $L = 121 \text{ m}$ and the average focusing beta function is $\beta = 18 \text{ m}$. Note that in reality the bunch shape is not Gaussian, and to obtain a more accurate result one would need to use the real bunch shape in the calculations. The results given in this report should serve as reasonable estimates. The generators of wakefields considered are the wall resistance of the beam tube, the flange gaps, the pumping slots, and the bellows. The effect of the beam position monitors (BPMs) is discussed in **Section 8.11.3**. Finally, the effects of wall surface roughness are considered.

8.9.3 The Resistive Wall Wakefields

The beam tube inside the undulator is made of stainless steel plated with copper. It is of circular cross-section and has a radius of $a = 2.5 \text{ mm}$. The normal formulas for the resistive wall wakefields are valid only if $\sigma_z/s_0 > 1$, with the characteristic distance

$$s_0 = \left(\frac{2a^2}{Z_0\sigma} \right)^{1/3}, \quad (8.45)$$

where $Z_0 = 377 \Omega$ and σ is the conductivity of the metal. For stainless steel (SS) $\sigma = 1.7 \times 10^6 \Omega^{-1}\text{-m}^{-1}$, for copper (Cu) it is $60 \times 10^6 \Omega^{-1}\text{-m}^{-1}$. Therefore, for the beam tube with SS $s_0 = 27 \mu\text{m}$, with Cu $s_0 = 8 \mu\text{m}$. Thus, in either case, since $\sigma_z \sim 20 \mu\text{m}$, the normal formulas should be valid. The average of the longitudinal wakefield of a Gaussian bunch is given by

$$\langle W_z \rangle \approx \frac{\Gamma(3/4)}{4\sqrt{2}\pi^2} \frac{c}{a\sigma_z^{3/2}} \left(\frac{Z_0}{\sigma} \right)^{1/2}, \quad \sigma_z/s_0 > 1 \quad (8.46)$$

with $\Gamma(3/4) \approx 1.23$, and the rms is given by $(W_z)_{rms} \approx (1.02)\langle W_z \rangle$. Combined with **Eq. (8.40)** this gives $\langle \delta \rangle = 0.34\%$ for stainless steel and 0.06% for copper, and similar results for the induced rms energy spread. The effects of the more realistic, non-Gaussian bunch distribution is calculated using the point-charge wake function [21],

$$W_z(s) = -\frac{4cZ_0}{\pi a^2} \left(\frac{1}{3} e^{-s/s_0} \cos \frac{\sqrt{3}s}{s_0} - \frac{\sqrt{2}}{\pi} \int_0^\infty \frac{x^2 e^{-x^2 s/s_0}}{x^6 + 8} dx \right), \quad (8.47)$$

generalized to the case where, s_0 is larger than or similar to the bunch length. Here, a , is the radius and, σ , the conductivity of the vacuum chamber. Here the resistive-wall loss and spread are both smaller than that of the Gaussian case examined above.

For the transverse case

$$\langle W_x \rangle \approx \frac{\Gamma(1/4)}{2\sqrt{2}\pi^2} \frac{c}{a^3\sigma_z^{1/2}} \left(\frac{Z_0}{\sigma} \right)^{1/2}, \quad \sigma_z/s_0 > 1 \quad (8.48)$$

with $\Gamma(1/4) \approx 3.63$. Combined with **Eq. (8.43)** it is seen that ν is 0.58 and 0.10 for the SS and Cu cases, respectively. For an extreme 100- μm oscillation (e.g. random pulse-to-pulse jitter which is not correctable) the emittance growth is 260% for SS and 8% in the case of Cu.

As to the effects of static errors, it is noted first that the beam tube is composed of 33 equal pieces. With uncorrelated, random misalignments with an rms of 100 μm , the emittance growth will be a factor of 33 less than given above. Or, conversely, the misalignment tolerance for 10% emittance growth, assuming copper is used, is 800 μm . For a correlated, cosine variation of misalignments of amplitude 100 μm the emittance growth is approximated by the above jitter results multiplied by $\text{sinc}^2(\Delta kL)$, where Δk is the deviation from the betatron wave number of the wall oscillation wave number. Finally, if the static emittance growth has to be kept to less than 10% anywhere within the undulator, the axis of the beam tube must be aligned to the axis of the quads to within 200 μm in the case of copper.

8.9.4 The Effect of Flange Gaps, Pumping Slots, and Bellows

The flange gaps are small cavities with a gap of $g = 0.25$ mm; over every 3.42-m section there are 4, or a total of $M = 132$ objects in the entire undulator. For the flange gaps, since $\sigma_z/a \ll 1$, the diffraction wakefield model applies [22]:

$$\langle W_z \rangle \approx \frac{\Gamma(1/4)}{4\pi^{5/2}} \frac{Z_0 c M}{aL} \sqrt{\frac{g}{\sigma_z}}, \quad \sigma_z/a \ll 1 \quad (8.49)$$

with $\Gamma(1/4) \approx 3.63$, and $(W_z)_{\text{rms}} \approx (0.40)\langle W_z \rangle$ gives the average effect of all the flange gaps. In the transverse case

$$\langle W_x \rangle \approx (4.63) \frac{Z_0 c M}{\pi^3 a^3 L} \sqrt{g\sigma_z}, \quad \sigma_z/a \ll 1. \quad (8.50)$$

Substituting for the parameters of the flange gaps, $\langle \delta \rangle = 0.012\%$ and $\sigma_\delta = 0.005\%$, the emittance growth due to a 100 μm oscillation is very small, 0.08%.

The pumping slots consist of ten, longitudinally arranged ovals in each 3.42 m section, or a total of $M = 330$ slots. For each slot the width $w = 1$ mm and length $g = 5$ mm. Usually in accelerators pumping slots are inductive. In the LCLS case, however, since $\pi\sigma_z$ is small compared to the slot width, energy will radiate into the slot. The diffraction formulas of the previous paragraph, multiplied by an azimuthal filling factor $w/2\pi a$ ($=0.064$), can be used to estimate the wakefields. The results are that $\langle \delta \rangle = 0.008\%$, $\sigma_\delta = 0.004\%$, and the emittance growth due to a 100 μm oscillation is 0.04%. There is one bellows in every 3.42 m section, giving a total of 33. The bellows are shielded, so that the wake effects should be negligible, and will be taken to be zero.

The results of the above calculations, as well as the effects of the BPMs (see **Section 8.12**), are summarized in **Table 8.8**. Note that a stainless steel surface (top row) is clearly not acceptable. It is further noted that, with copper, the resistive wall wakefield still dominates the

impedance, though in this case, the rms energy spread is nearly a factor of two below the maximum tolerable deviation per slice. Finally, another effect that will add to these values is that of incoherent synchrotron radiation within in the undulator, which will produce a relative energy loss of 0.16% for a 14.3 GeV electron beam. Combining this with the loss factors (Cu) of results in a total loss of ~0.3% which is approximately the undulator field taper required. These results are for a Gaussian bunch distribution. The effects of the non-Gaussian distribution are examined in **Chapter 4**.

Table 8.8 The total longitudinal and transverse wakefield effects, for a Gaussian axial distribution, due to the various types of objects in the LCLS undulator. Given are the average energy loss, $\langle \delta \rangle$, the rms energy spread, σ_δ , and the relative correlated emittance growth, $\Delta \epsilon / \epsilon_0$, of a 100 μm betatron oscillation.

Type of Objects	$\langle \delta \rangle / \%$	$\sigma_\delta / \%$	$\Delta \epsilon / \epsilon_0 / \%$
Resistive Wall (SS)	0.340	0.350	260
Resistive Wall (Cu)	0.060	0.060	8
Flange Gaps	0.008	0.003	0.08
Pumping Slots	0.006	0.002	0.06
BPMs	0.019	0.007	0.007

8.9.5 The Effect of Wall Surface Roughness

In the first model of wakefields [23] the roughness was simulated by a collection of bumps of a given shape randomly distributed over a smooth surface. If the bump dimensions are small compared to the bunch length, the impedance in this model is purely inductive. For such simple shapes of the bumps as hemispheres or cubes, the model predicts relatively large impedance and results in severe tolerances on the level of roughness. A more realistic model of roughness effects was developed in Ref. [24]. In this model, the rough surface is considered as a terrain with a slowly varying slope. As was shown in direct measurements of the surface roughness with Atomic Force Microscope [25], this representation of the roughness is adequate for the real surface of the prototype pipe for the LCLS undulator. In the limit when the bunch length is larger than the correlation length of the roughness, the impedance in this model is also inductive,

however the tolerance on the rms height of the surface roughness are much looser than predicted in [23].

In another approach [26], the roughness wakefield was associated with the excitation of a resonant mode whose phase velocity is equal to the speed of light. The existence of such modes in a round pipe with periodically corrugated walls with rectangular shape of the corrugation was studied theoretically in Ref. [27]. In the case when the typical depth of the wall perturbations is comparable to the period, it was shown that the loss factor of such modes reaches the theoretically maximal value for the resonant wakefield. However, as was shown in [28], when the height of the periodic wall corrugations becomes smaller than the period, the loss factor for the mode rapidly decreases.

A naive idea of a rough surface as a microscopic mountain country with sharp peaks and deep canyons does not correspond to reality. A metal surface with a good finish more resembles water surface of a swimming pool in quiet weather. Pictures of scanned surfaces for different types of machining can be found in surface metrology books [29,30]. Most of them are characterized by a typical peak-to-valley height h of the roughness that is much smaller than the spacing between the crests g . The *aspect ratio* g/h can easily exceed a hundred for smooth surfaces. For illustration, **Figure 8.32** shows the profile of a surface of a metal pipe measured in Ref. [25]. This pipe is considered as a possible prototype for the vacuum chamber of the LCLS undulator. The rms height of the roughness for this surface is about 100 nm, and the transverse size g , as is seen from the picture, can exceed tens or even a hundred of microns.

The small ratio h/g implies a small angle θ between the tangent to the surface and the horizontal plane. Using the smallness of this parameter it is possible to develop a perturbation theory of electromagnetic interaction of the beam with the surface based on the so-called *small-angle* approximation [24]. This approach extends the earlier treatments [31,32] of an axisymmetric periodic perturbation of the boundary. It also agrees with the more general results of Ref. [33] valid for nonperiodic axisymmetric boundary perturbations.

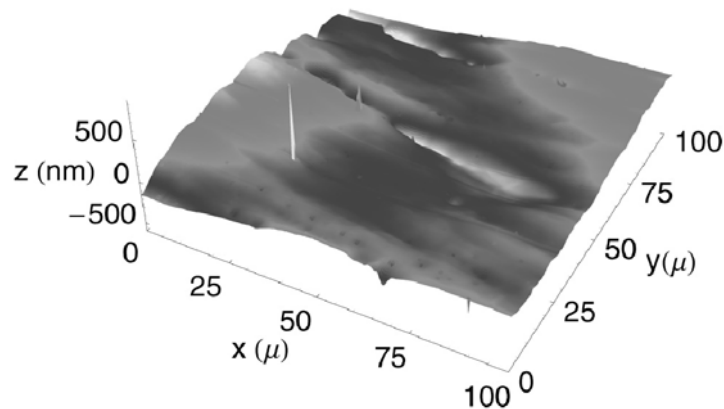


Figure 8.32 A sample surface profile measured with Atomic Force Microscope in Ref. [29]. Note the different scales in the vertical and horizontal directions.

As follows from Refs. [31,32], for a periodically corrugated wall with the wavelength λ_0 much smaller than the pipe radius b , there exist synchronous modes in the pipe which propagate with phase velocity equal to the speed of light. The wavelength of these modes is below $2\lambda_0$, so that only a short bunch of length $\sigma_z \leq 2\lambda_0$ can efficiently excite these modes. If, on the other hand, the bunch length is larger than λ_0 , the excitation of these modes will be relatively weak. In the roughness problem the parameter g plays the role of λ_0 , and two different regimes are expected depending on whether σ_z is larger or smaller than g .

In the regime where $\sigma_z > g$ one expects an inductive impedance because the beam does not lose energy by excitation of synchronous modes. However, the interaction between the head and the tail of the bunch can cause energy variation along the bunch and may interfere with the lasing.

Let $h(x, z)$ denote the local height of the rough surface as a function of coordinate x in azimuthal direction, and coordinate z along the axis of the pipe. The requirement $h \ll g$ can alternatively be expressed as $\Theta \approx |\nabla h| \ll 1$. The treatment of Ref. [24] was additionally limited by the assumption that the bunch length is larger than the typical size of the roughness bumps, $\hat{\lambda} \sim \sigma_z \gg g$. It was found that in this limit the impedance is purely inductive, and the inductance \mathcal{L} per unit length of the pipe is given by the following formula:

$$\mathcal{L} = \frac{Z_0}{2\pi cb} \int_{-\infty}^{\infty} \frac{\kappa_z^2}{\sqrt{\kappa_g^2 + \kappa_z^2}} S(\kappa_z, \kappa_g) d\kappa_z d\kappa_g, \quad (8.51)$$

where $Z_0 = 4\pi/c = 377$ Ohm, and $S(\kappa_z, \kappa_g)$ is the spectrum of the surface profile as a function of wave numbers k_z and k_g in the longitudinal and azimuthal directions, respectively. The spectral density S can be defined as a square of the absolute value of Fourier transform of h ,

$$S(\kappa_z, \kappa_g) = \frac{1}{(2\pi)^2 A} \left| \int_A h(z, x) e^{-i\kappa_z z - i\kappa_g x} dz dx \right|^2, \quad (8.52)$$

where the integration goes over the surface of a sample of area A . It is assumed that the sample area is large enough so that the characteristic size, \sqrt{A} , is much smaller than the correlation length, g , of the roughness.

In Ref. [34] a comparison was done between the small-angle approximation and a previous model of roughness, developed in [23]. It was shown that in the region of mutual applicability both models give the results, which, within a numerical factor, agree with each other.

A detailed study of the surface roughness for a prototype of the LCLS undulator pipe using the Atomic Force Microscope was done in Ref. [25]. A high quality Type 316-L stainless steel tubing from the VALEX Corporation with an outer diameter of 6.35 mm and a wall thickness of 0.89 mm with the best commercial finish, A5, was used for the measurements. The samples to be analyzed were cut from this tubing using an electrical discharge wire cutting process, to eliminate damage from mechanical processing. The samples were subsequently cleaned chemically to remove particles adhering to the surface from the cutting process, which used a brass wire.

The measured profiles were Fourier-transformed and the inductance \mathcal{L} per unit length of the pipe was calculated using **Eq. (8.51)**. Because this inductance is inversely proportional to the pipe radius b , a convenient quantity is the product $\mathcal{L}b$, which does not depend on the pipe radius and characterizes the intrinsic properties of the surface. The computed value of this product was found to be between 3×10^{-4} pH and 5×10^{-4} pH.

These values should be compared with the impedance budget for the LCLS beam. For the nominal parameters of the LCLS: beam charge 1 nC, $\sigma_z = 20 \mu\text{m}$, undulator length 112 m, and final beam energy $E = 14.3 \text{ GeV}$, one finds that the requirement that the relative energy spread $\delta E_{rms}/E$ generated by the wake be less than 0.05% is met for $\mathcal{L} < 1.6 \text{ pH/m}$. For the vacuum pipe radius $b = 2.5 \text{ mm}$ the tolerance on the product $\mathcal{L}b$ is $(\mathcal{L}b)_{tol} = 4 \times 10^{-3} \text{ pH}$. The measured value of the impedance is seen to be almost an order of magnitude smaller than the tolerance.

It should be emphasized here that the above results are based on two assumptions that are not completely fulfilled for the LCLS. First, a Gaussian beam distribution was assumed. As detailed simulations show [58], for the LCLS the bunch shape more resembles a rectangular than a Gaussian shape. Second, **Eq. (8.51)** used for the calculation of the inductance, was derived in the limit $\sigma_z \gg g$, which, as roughness measurements indicate, is not satisfied.

The theory for the case $\sigma_z < g$, which is more pertinent to the measurements, was developed in [14]. In this theory the roughness was treated as a sinusoidal wall corrugation with the amplitude h_0 and the period $2\pi/\kappa$. The amplitude h_0 of the corrugation is assumed much smaller than the period, $h_0\kappa \ll 1$, which is a requirement of the small-angle approximation. Such a corrugation qualitatively simulates a rough surface with parameter $g \sim \kappa^{-1}$ and the rms height of the bumps of the order of h_0 .

This theory shows, that when using the long-bunch approximation ($\sigma_z\kappa \gg 1$) in the regime where $\sigma_z\kappa < 1$, the wake is overestimated by a factor of $(\sigma_z\kappa)^{-1/2} \sim (g/\sigma_z)^{1/2}$. For this reason, the result of Ref. [25] should be considered as an upper boundary for the roughness impedance.

Using the result of Ref. [35], the wake for a rectangular bunch shape, $\rho(s) = 1/l_z$ for $0 < s < l_z$ can be calculated. The parameters used in the calculation are: beam charge 1 nC, $h_0 = .28 \mu\text{m}$ (corresponding to the rms roughness of $0.2 \mu\text{m}$), $g = 2\pi/\kappa = 100 \mu\text{m}$, $L = 112 \text{ m}$, $E = 14.3 \text{ GeV}$, $b = 2.5 \text{ mm}$. The average energy loss for the distribution shown in **Figure 8.33** is 4.5×10^{-5} and the rms energy spread is 2×10^{-5} . In addition to the mechanism of the wake generation described above involving interaction with short-wavelength waves, $\tilde{\lambda} \leq g$, there is another contribution to the wake, which was first pointed out by A. Novokhatski and A. Mosnier [26]. It comes from a relatively low-frequency synchronous mode with $\tilde{\lambda} \gg g$.

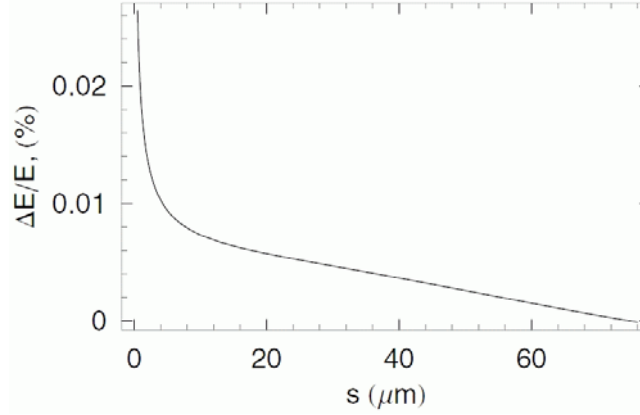


Figure 8.33 The relative energy loss of the LCLS beam at the end of the undulator as a function of position within the bunch.

The properties of the synchronous mode in the case of rectangular corrugation of the wall were studied in Ref. [27]. In this paper, the wall roughness was modeled by axisymmetric periodic steps on the surface of height δ , width g , and period p . All three parameters were assumed much smaller than the pipe radius b . The model gives for the frequency ω_0 of the mode

$$\omega_0 = c \sqrt{\frac{2p}{\delta b g}}, \quad (8.53)$$

and for the longitudinal wakefunction of the point charge

$$w(s) = \frac{Z_0 c}{\pi b^2} \cos(\omega_0 s / c), \quad (8.54)$$

Surprisingly, the amplitude of the wake in this approximation does not depend on the roughness properties at all. These results however are valid if $kp \ll 1$. **Eq. (8.53)** shows that when δ becomes very small, the parameter k increases and eventually kp becomes comparable to unity. Hence, this model becomes invalid in the limit $\delta \rightarrow 0$. The results of computer simulations that confirm the predictions of this model can be found in Refs. [36,37].

To take into account the effect of the shallowness of the roughness a different model was developed in Ref. [28]. In this model the roughness was treated as a sinusoidal perturbation of the wall with $h_0 \kappa \ll 1$. It was found that, indeed, under certain conditions, a low-frequency synchronous mode with $\lambda \kappa \gg 1$ can propagate in this system. The longitudinal wake generated by this mode is given by

$$w(s) = \frac{2Z_0 c}{\pi b^2} U \cos(\omega_0 s / c), \quad (8.55)$$

where the dimensionless factor U and the frequency of the mode ω_0 depend on the parameter $r \equiv h_0 \sqrt{b \kappa^3} / 2$. The plot of these two functions is shown in **Figure 8.34**. In the limit $h_0 \rightarrow 0$ the frequency ω_0 approaches $\kappa c / 2$, and $U \approx r^4 / 32$. For large values of r , $\omega_0 \approx 2c / h \sqrt{b \kappa}$ and $U \rightarrow 1/2$.

To estimate the wake, realistic parameters of roughness, i.e. $h_0 = 0.28 \mu\text{m}$ (corresponding to the rms roughness of $0.2 \mu\text{m}$), $g = 2\pi/\kappa = 100 \mu\text{m}$, and $b = 2.5 \text{ mm}$, are used. This gives a value of $r \equiv h_0 \sqrt{b\kappa^3} / 2 = 0.11$. The corresponding loss-factor parameter is

$$U \approx 4.5 \cdot 10^{-6}, \tag{8.56}$$

which indicates that the effect of the wake in this regime will be negligibly small.

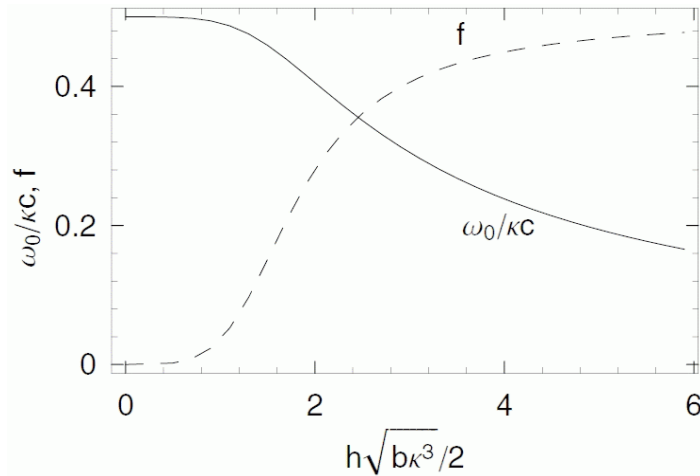


Figure 8.34 Synchronous mode dispersion relation.

It is important to emphasize here that the wakefield generated by the roughness is very sensitive to the geometry of the surface profile. The models which do not take into account the large aspect ratio of the real roughness — the ratio of the characteristic size along the surface (correlation length) and the typical height of the bumps — tend to overestimate the impedance and lead to very tight tolerances for the surface smoothness. The latest models that include the large aspect ratio into consideration predict much smaller impedance which is below the tolerable level for the LCLS undulator, if the typical height $\sim 100 \text{ nm}$ and $g \sim 100 \mu\text{m}$. The surface measurements [25] show that roughness with such characteristics can be achieved in a pipe with a good surface finish.

8.10 Ion Effects

In this section the number of ions generated during a bunch passage in the 121 m long undulator line of the LCLS x-ray FEL is calculated, emittance dilution caused by these ions is discussed, and the acceptable vacuum pressure is estimated.

8.10.1 Introduction

This section investigates ion production by the beam and by the synchrotron-radiation photons during a bunch passage in the LCLS undulator [38], and three different mechanisms of emittance dilution induced by these ions. The acceptable vacuum pressure for FEL operation is estimated from the calculated emittance growth.

8.10.2 Ionization Processes

There are three conceivable mechanisms by which ions can be created:

8.10.2.1 Ionization by the beam.

A typical ionization cross-section for a 15 GeV electron beam and carbon monoxide or nitrogen gas is of the order of 2 Mbarn (the ionization cross section for hydrogen molecules would be approximately 10 times smaller). The 2-Mbarn cross section translates into an ion line density of about

$$e_{ion}[m^{-1}] \approx 5N_b p[nTorr] \quad (8.57)$$

at the end of the bunch, or 320 ions per meter for a pressure of 10 nTorr and $N_b = 6.3 \cdot 10^9$ electrons per bunch.

8.10.2.2 Ionization by incoherent synchrotron radiation.

The ionization cross-section of 8-keV photons for typical elements is about 100 barn [39]. Even though the number of photons at 1.5 \AA is three orders of magnitude higher than the number of electrons, this cross section is so much smaller than the collision-ionization cross section that the photoionization at Angstrom wavelengths can be neglected in comparison.

In addition to the photons emitted at the first (and higher) FEL harmonic wavelengths, a broad spontaneous photon spectrum extends to much lower energies, where the photoionization cross section is considerably higher. Below about 100 eV the photoionization cross section becomes comparable to, and may even exceed by up to a factor of 5, the cross section for collisional ionization.

From Figure 6 in Ref. [38], illustrating the spontaneous photon spectrum, and from **Figure 8.35**, showing its low-energy part, it is estimated that, at the end of the undulator, there are about 6×10^{10} photons per bunch with energies below 1 keV, and fewer than 5×10^9 photons whose energy is below 100 eV. Thus, the number of low-energetic photons is about equal to the number of electrons in the bunch. With an rms opening angle of 10-20 μrad for the spontaneous radiation (and an even wider opening angle at low photon energies), the photoionization processes occur on average far away from the beam orbit. Therefore, considering the small number of low-energy photons, the ions are assumed to be produced by photo-ionization form a diffuse halo, whose effect on the beam is negligible compared with that of the much denser ion cloud produced by collisional ionization inside the beam.

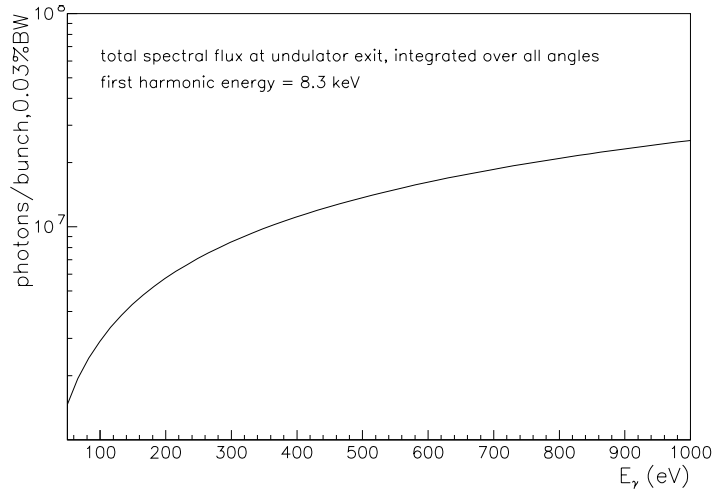


Figure 8.35 Number of photons per 0.03 % frequency interval and per bunch passage at the end of the LCLS undulator; the spontaneous flux increases linearly along the undulator.

8.10.2.3 Tunneling ionization in the coherent laser field.

Up to frequencies of the order

$$\omega_t = ceE / \sqrt{2m_e c^2 I} \quad (8.58)$$

the tunnel effect is determined simply by the instantaneous value of the electric field [40,41]. In Eq. (8.58), the parameter E is the electric field, m_e the electron mass, and I the ionization potential. The peak electric field of the laser pulse can be roughly estimated from the equation

$$\hat{E} \approx \left(\frac{2N_\gamma h\nu}{(2\pi)^{3/2} \varepsilon_0 \sigma_x \sigma_y \sigma_z} \right)^{1/2} \quad (8.59)$$

and is found to be about 85 GV/m. Somewhat arbitrarily using $I \approx 20$ eV, the threshold frequency is $\omega_t \approx 10^{16} \text{ s}^{-1}$, which is very low compared to the FEL frequency $\omega \approx 10^{19} \text{ s}^{-1}$. This means that the standard formula for static tunneling ionization does not apply here. To determine if the coherence of the FEL x-rays is important, the photon density is calculated as

$$n_\gamma \approx \frac{N_\gamma}{(2\pi)^{3/2} \sigma_x \sigma_y \sigma_z} \approx 7.2 \times 10^{24} \text{ m}^{-3}, \quad (8.60)$$

which implies that in a sphere with a radius equal to the Bohr radius a_0 ($a_0 \approx 0.5 \text{ \AA}$) on average there are only 1.2×10^{-6} photons at any given time during the pulse. It is thus legitimate to consider the photons as incoherent [42], in which case, as seen under point 2, their contribution to the ionization is insignificant.

8.10.3 Emittance Dilution

Ions could dilute the bunch emittance in various ways: first, the ions induce a tune shift across the bunch which could lead to filamentation and to an effective increase in the transverse emittance; second, the electrons or, third, the ions generated by the bunch head can excite the bunch tail and cause a beam break-up instability.

Pessimistically assuming that all electrons originating in the ionization process are dispersed and lost before the end of the bunch (using this assumption, which is not fulfilled for the LCLS, the actual tune shift will be overestimated), one can estimate the ion-induced shift in betatron phase advance between head and tail of the bunch at the end of the undulator:

$$\Delta\psi_{\beta_{xy}} \approx \frac{\beta_{x,y} r_e \lambda_{ion} L_u}{\gamma \sigma_{x,y} (\sigma_x + \sigma_y)} \quad (8.61)$$

Using an ion line density λ_{ion} , as expected for collisional ionization, **Eq. (8.57)**, the phase shift is $\Delta\psi_{x,y} \approx 4 \times 10^{-6}$ rad for 1 nTorr and 4×10^{-4} rad for 100 nTorr. Significant emittance growth due to filamentation would be expected only for an average pressure exceeding 100 μ Torr, for which the phase shift approaches 1 rad.

Since, different from the situation in most other accelerators, the bunch length in the LCLS is same order than the transverse beam size, the electrons do not escape from the bunch during its passage, but the electrons generated by the head will still affect the trailing particles. The resulting emittance growth can be estimated from a first-order perturbation expansion, in analogy to the treatment in [43]:

$$\Delta\epsilon_y \approx \frac{\pi^2 N_b \lambda_{ion}^2 r_e^3 \sigma_z L_u^2 \hat{y}^2 \beta_y}{54 \sqrt{2\pi} \gamma^2 \sigma_y^3 (\sigma_x + \sigma_y)^3} \quad (8.62)$$

where \hat{y} describes the amplitude of an initial vertical perturbation of the form $y_b^0(s,z) = \hat{y} \cos(s/\beta + \phi) \sinh(\omega_i z + \theta)$ with $\omega_i \equiv [4 N_b r_e / 3 \sqrt{2\pi} \sigma_x \sigma_y (\sigma_x + \sigma_y)]^{1/2}$, where s is the longitudinal position along the beam line, and z denotes the longitudinal position of a particle with respect to the bunch center. Inserting numbers, $\omega_i \sigma \approx 0.3$. Exactly the same expression with the subindices x and y interchanged applies to the horizontal case, and, by symmetry, it yields the same emittance growth. Inserting numbers and assuming an ion density as in **Eq. (8.57)**, **Eq. (8.62)** is rewritten as

$$\Delta(\gamma\epsilon_y)[\text{m}] \approx 4 \times 10^{-19} \left(\frac{\hat{y}}{\sigma_y} \right)^2 (p[\text{nTorr}])^2. \quad (8.63)$$

For a huge perturbation, $\hat{y} \approx 10\sigma_y$, one finds that the emittance growth becomes significant when the pressure approaches 10^{-4} Torr, which is three orders of magnitude higher than the anticipated operating pressure.

8.10.4 Conclusion

In this section, the number of ions generated during a bunch passage in the LCLS undulator and their effect on the beam emittance has been established. The ionization of the residual gas due to the coherent x-rays and, from the viewpoint of beam dynamics, also the ionization due to the lower-energetic spontaneous photons were found to be insignificant compared with the collisional ionization by the beam. There is not a tight tolerance on the vacuum pressure in the LCLS undulator. Even a pressure as high as 1 μ Torr would still appear to be perfectly acceptable.

8.11 Electron Beam Diagnostics

8.11.1 Performance Requirements

For proper operation of the LCLS free electron laser, the electron beam trajectory through the undulator segment must deviate from straightness by no more than 2 microns rms over approximately a 10-meter field gain length. The goal for beam trajectory measurement stability is required to be better than 1 micron rms for at least an 8 hour time period. Imaging diagnostics must be able to resolve the transverse beam size as small as 30 microns rms. These requirements are to be met using 0.1 – 1.0 nC of charge per pulse with a repetition rate as high as 120 Hz. The vacuum chamber has a full aperture of 5 mm.

8.11.2 Overview

The LCLS undulator will consist of an array of thirty-three 3.4-meter-long undulator segments separated by short breaks containing diagnostics and permanent magnet focusing elements. The thirty-three segments are arranged in sets of three, forming eleven half-cells, with somewhat longer breaks between half-cells to allow for additional diagnostics. Approximately 15 cm will be available for electron beam diagnostics at each transition section.

Shown in **Table 8.9** is a summary of the electron beam diagnostics to be used in the undulator segment. A total of 48 beam position monitors (BPMs) are required between the undulator segments and at the extreme upstream and downstream ends of the undulator. Two BPMs will be used in the breaks between half-cells. Optical transition radiation imaging diagnostics will be provided in these longer breaks at every third diagnostic station, in addition to being located at three successive locations upstream of the undulator for a three-screen emittance measurement. A complementary measure of emittance will be provided by a set of four wire scanners located upstream of the undulator. Working in combination with a set of 33 Cherenkov detectors, the wire scanners will provide a very precise measure of the beam size averaged over many pulses. In addition these wire scanners will assist in defining the average incoming electron beam trajectory (position and angle).

The Cherenkov detectors are sensitive to hard gamma and high energy electrons but not the x-rays generated in the FEL process. Located at all diagnostics stations, they detect electron beam losses generated by the wire scanners for emittance measurement, or as a result of beam

missteering. A current monitoring toroid will be placed at the entry and exit of the entire array, providing information on beam intensity and transfer efficiency.

Table 8.9 Undulator electron beam diagnostics

Type	Quantity	Location
Beam position monitor	48	All stations
Optical transition radiation (OTR) imaging diagnostic	13	Every third station
Wire scanners	4	Upstream of Undulator segments
Cherenkov Detectors	33	All stations
Current Monitors	2	Upstream and downstream of undulator

8.11.3 Undulator Beam Position Monitors

Conventional button-type or stripline-type pickup electrodes combined with similarly conventional electronics, e.g. amplitude to phase conversion, can provide sub-micron single shot beam position measurement resolution when using small beam apertures. Two micron rms resolution with a 4 mm aperture has been demonstrated at the Advanced Photon Source (APS) low energy undulator test line (LEUTL) [44]. Because the sensitivity of conventional button- or stripline-type beam position monitors (BPMs) scales with vacuum chamber aperture [45], electronics stability need only be better than about one part in a thousand in the determination of “difference over sum” to achieve micron-scale measurement stability with a 5-mm aperture.

While position monitoring resolution at the micron scale is straight forward, even for single shot diagnostics, absolute accuracy becomes extremely difficult below the 50-micron scale, owing to fabrication and assembly tolerances, and survey and alignment limitations. Separate Anocast[®] piers that provide better than 1-micron stability support the modules. The positions of the BPM modules are locally adjustable for alignment purposes.

Because absolute accuracy is difficult, it will be important to make use of beam-based alignment in the determination of position monitor offsets relative to nearby focusing elements. It is expected that this determination can be made at the 2-micron level or better using a procedure expected to take a few of hours of machine time.

In order to assure the long-term stability of position measurement, the combination of standard button-style pickup electrodes with a cavity-based pickup in a compact assembly is envisaged (**Figure 8.36**). The strengths of the cavity-based position monitor are that it has a very stable and reproducible electrical center, very high resolution (10s of nm) with very small amounts of beam [46], and that it can be very accurately machined, down to the micron-level [47]. Disadvantages of the cavity BPM technique are the need for a reference phase signal for determining the sign of the position measurement, in addition to possible problems associated with wakefield effects on the beam. Because a higher order mode conveys the position information, the rejection of the fundamental mode frequency in the electronics places a fundamental limitation on position determination, although this limitation is expected to be at or

below the 1-micron level. The raw position signal from a cavity BPM is proportional to beam charge, so that a normalization procedure will be necessary to extract position information.

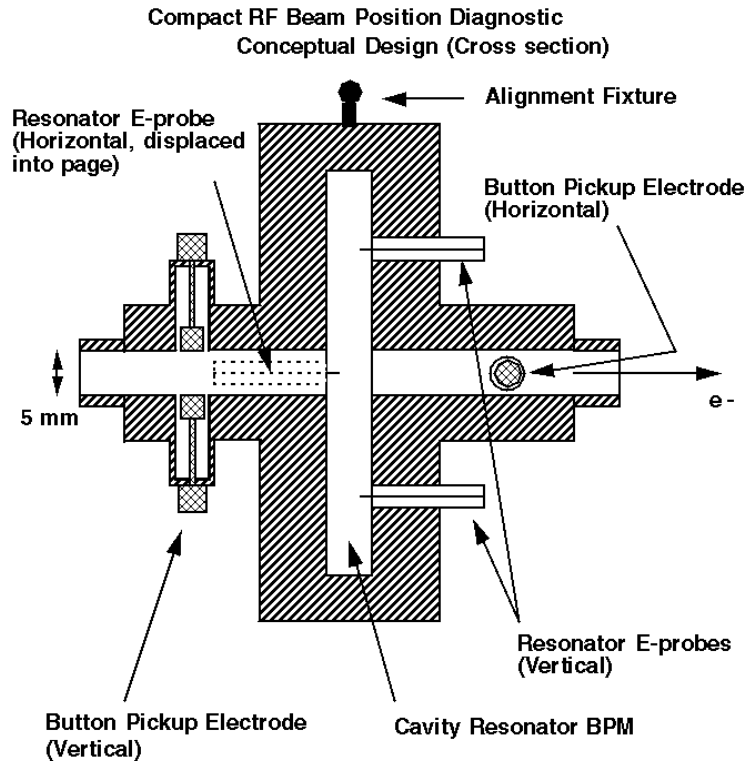


Figure 8.36 Conceptual design for a combined button- and cavity-type position monitor

Recent research at Stanford, supporting the NLC project, has produced an X-band cavity-BPM design, which solves the fundamental mode problem by a clever arrangement of the output waveguides [48]. In this design, a second cavity is also integrated in the design with its fundamental mode frequency set to match the position sensitive cavity's mode frequency. This second cavity can then be used to extract the phase (sign) information, in addition to providing charge normalization.

The incorporation of conventional button- and cavity- type pickup electrodes in the same assembly affords several advantages over either system alone. It is relatively simple to calculate the sensitivity (e.g. volts per micron) of a conventional button-type position monitor. The analogous sensitivity for the cavity monitor, though potentially much higher, depends on such things as cavity Q, waveguide coupling efficiency, etc., and as such may not be as easily determined *a priori*. A cross-calibration of the two with beam immediately resolves any uncertainties in the determination of length scales. Similarly, the cavity monitor has a very easily determined and highly accurate electrical center, reproducible at the sub-micron level, while conventional electronics have always performed poorly in this regard. By steering to the cavity null and recording the readbacks from the conventional electronics attached to the buttons, uncertainty in electrical center stability of the conventional electronics is significantly reduced.

Using this “belt and suspenders” approach will increase confidence in the electron beam trajectory determination, in addition to simplifying the electronics for the cavity, since no microwave phase determinations will be needed to determine the sign of the position.

A fundamental limitation on the ability to align the beam along the undulator segments will be mechanical stability of components arising from thermal drift, ground settling, etc. Even with careful design, 10 micron-scale component position drifts over 24 to 48 hour periods should be expected. While a careful initial alignment (< 50 microns absolute) is important, the key to success will be to have a robust beam-based alignment algorithm in place for the relative determination of magnet and diagnostic centroids.

8.11.4 Undulator Optical Transition Radiation (OTR) Electron-Beam Profile Monitors

It will be critical to the ultimate understanding of the LCLS SASE physics for the electron-beam transverse size and profile to be monitored between the undulator segments. The transverse size of $\sigma_{x,y}=30 \mu\text{m}$ for a 14.5 GeV beam involving a 1nC bunch is a challenge. It is also required that the bremsstrahlung radiation generated by the electron beam's interaction with the radiation converter be minimized. Based on experiences gained at several laboratories, the use of optical transition radiation (OTR) converter screens/foils made of low- z , ultra thin foils as a minimally intercepting technique is planned. Such thin foils should generate lower levels of bremsstrahlung than the crystals proposed for x-ray beam diagnostics.

Several successful examples of OTR experiments can be cited. Beam sizes of $30 \mu\text{m}$ (σ) for a 600-MeV beam at APS using an aluminum mirror surface as converter [49] have been observed. In addition, preliminary images at 7-GeV in a transport line at APS have been obtained. At Jefferson Lab's CEBAF, 0.8- μm thin aluminum foils have been used with a 4-GeV, 200 μA beam for beam sizes of $50 \mu\text{m}$ (σ) [50]. Experiments have also been done at SLAC with a 30-GeV beam as reported at PAC '99 [51]. More recently in the APS SASE FEL project, OTR imaging from a flat mirror as well as a 6- μm thick foil have been used between undulator segments for the 217-MeV beam. Total system resolution has been limited by the camera optics employed, not the OTR mechanism.

Some brief background on the OTR mechanism is in order [52]. Optical transition radiation is generated at the boundary of media with different dielectric constants, such as vacuum and a metal, as the charged particle transits the boundary. It is a surface phenomenon and therefore has no volume effect as do scintillators or known saturation effects. One might simplistically describe this process by the formation of an image charge in the foil as the charged particle approaches the boundary. As the charge reaches the boundary, the charge and its image basically act as a collapsing dipole, and a burst of broadband radiation is emitted. As shown in **Figure 8.37** there is both forward OTR and backward OTR relative to the e-beam direction. If the foil surface is inclined at 45° to the beam direction, then the backward OTR is emitted in an annular cone around the angle of specular reflection, 90° in this case. Although the azimuthal intensity peak is at $1/\gamma$, where γ is the Lorentz factor, OTR is emitted into large angles as well. Most of the total

power is at angles greater than $1/\gamma$. For this reason, the OTR is not diffraction-limited at $1/\gamma$, but limited only by the aperture of the collecting optics for a given wavelength. **Figure 8.38** shows a schematic of the OTR angular distribution features at 40 MeV. For a wide-aperture optical system, sub-10 μm resolution is expected. At APS, B. Yang has recently tested in the lab a camera-lens package with sub-10 μm resolution for the chicane beam size monitor.

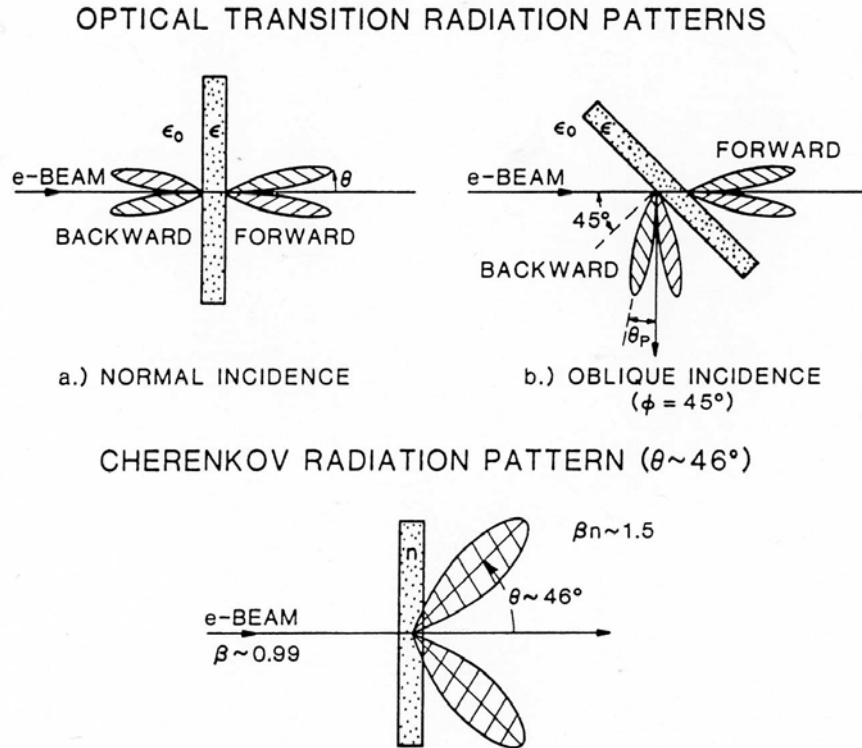


Figure 8.37 A schematic of forward OTR and backward OTR generation for interfaces normal to the beam (left) and at 45° to the beam (right). The dielectric constants for vacuum (ϵ_0) and the medium (ϵ) are indicated.

In addition to the beam profile function, one may take advantage of the laser-like angular distribution of OTR to measure e-beam angle. As has been done in previous experiments in the 1980's, the camera-lens system can be set so the sensor is at the focal plane of the lens. In this configuration far-field or angular distribution information is obtainable as schematically illustrated in **Figure 8.39**. Since in this case $1/\gamma \sim 35 \mu\text{rad}$, the optics and distances would have to be chosen appropriately. Alternatively, at a 10-m distance the angular divergence contribution from OTR would give a projected spot size of $\sim 700 \mu\text{m}$ with no lens. The centroid of such an image is related to beam direction and angle. An angle sensitivity of several micro-radians should be possible.

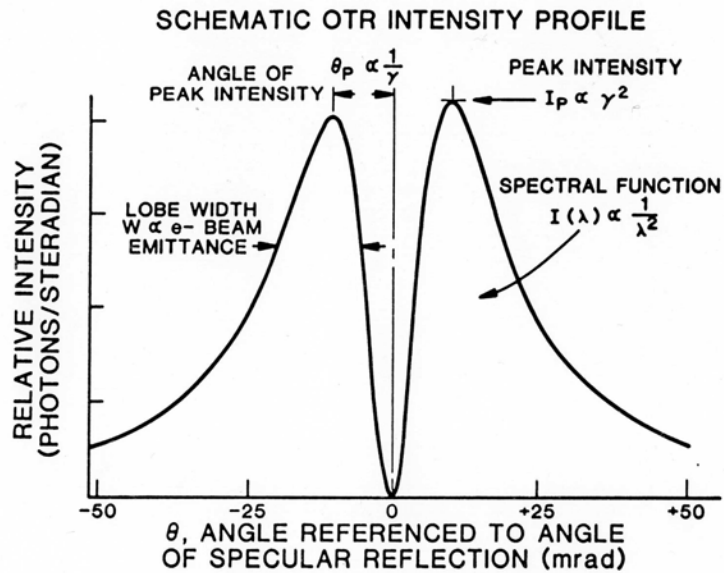


Figure 8.38 A schematic of the OTR intensity profile in the angular distribution pattern. The angle θ is referenced to the angle of specular reflection and the peak is at $1/\gamma$.

Some tests on foil survivability are needed. An engineering design for stretching the thin foil across an aperture of few-mm diameter is also needed. In addition, another foil that is opaque to visible synchrotron radiation will be installed upstream of the 45° foil. Extensions of OTR techniques to x-ray transition radiation (XTR) or diffraction radiation (DR) techniques may provide some trades on spatial resolution and nonintercepting features, respectively. A schematic of the diagnostics station is shown in **Figure 8.54**.

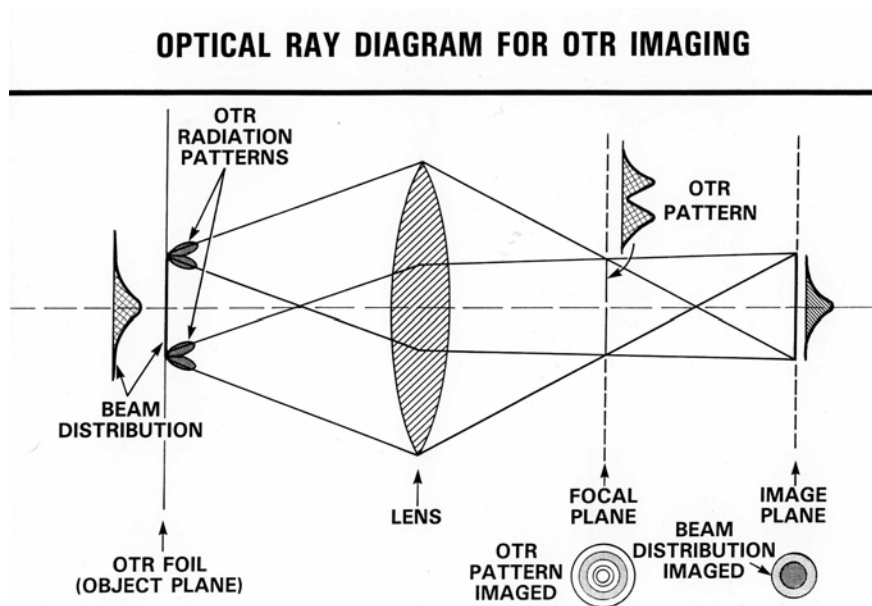


Figure 8.39 An optical ray diagram for imaging of OTR when the sensor is positioned at the focal plane and image plane. Such imaging provides the OTR angular distribution pattern or the beam profile, respectively.

8.11.5 Cherenkov Detectors

A series of Cherenkov detectors will be placed at all diagnostics stations between undulator segments. These devices are similar to those used at the PEP-II project as beam loss monitors [53]. These devices are quite simple conceptually, involving a small piece of fused silica glass, which emits Cherenkov radiation when traversed by high energy charged particles. A miniature photomultiplier tube is used to amplify these small pulses, which are then transmitted to data acquisition electronics, e.g. a gated integrator followed by a digitizer. To prevent FEL x-rays from corrupting the bremsstrahlung gamma ray signal, the fused silica pellet is embedded in a lead-lined housing such that only very high energy photons can penetrate. Refinements to the PEP-II mechanical design and data acquisition have been carried out recently at the APS [54].

8.11.6 Current Monitoring Toroids

High quality pulsed current monitoring toroids are commercially available, together with front end electronics, if so desired. It is important to measure the charge entering and exiting the undulator to provide information for normalization of data sets and to tune for maximum transport efficiency. It should be straightforward to monitor a nominal 1 nC pulse with a few percent accuracy shot to shot. Data acquisition is provided.

8.12 Beam-based Alignment

8.12.1 Undulator Beam-Based Alignment

The electron trajectory within the LCLS undulator needs to be straight to a high degree of accuracy so that the 1.5-Å radiation grows efficiently over each gain length. For the LCLS, this condition requires a trajectory straightness of a few microns over a ~10-meter length. This level is very difficult to achieve with component survey alignment techniques. For this reason, the final alignment will rely on empirical *beam-based* alignment, which makes use of beam position monitor (BPM) readings as a function of large, deliberate variations of the electron energy. The BPM measurements at various energies are analyzed and then converted to 1) quadrupole magnet transverse position offsets, 2) BPM readback offset corrections and 3) adjustments of the incoming beam position and angle at the undulator entrance (initial launch conditions). The alignment procedure is repeated three times in succession for the initial machine startup, and then one pass of the procedure is reapplied approximately once per month, as necessary. Between these infrequent applications, a fine steering technique will be used for daily trajectory control, and a fast feedback system will maintain the trajectory over the time scale of a few pulses. This section primarily discusses the most involved alignment procedure, which is applied during the initial machine commissioning period. The effects of various errors are included in a full simulation of the alignment procedure.

8.12.1.1 Introduction

The readback m_i of the i^{th} BPM, which measures the centroid of the transverse position of the electron bunch at location s_i along the beamline, can be written as

$$m_i = \sum_{j=1}^i \theta_j C_{ij} - b_i \quad , \quad (8.64)$$

where θ_j is the kick angle at point j ($< i$) due to a transversely misaligned quadrupole magnet or undulator pole field error upstream of BPM- i , C_{ij} is the transfer coefficient which maps a beam angle at point j to a position at point i , and b_i is the readback offset (mechanical misalignment and/or electrical bias) of the i^{th} BPM. This is described graphically in **Figure 8.40** where the BPMs are shown as circles. The kick angles in the figure are represented as dipoles, however they are completely equivalent to either quadrupole magnets with transverse displacements and/or field strength errors of the undulator poles. The quadrupole focusing within the undulator is not explicitly shown in the figure, but it is represented mathematically in the transfer coefficients, C_{ij} . The initial launch conditions are ignored for now (more on this below).

Since the kick angles θ_j are inversely proportional to beam momentum p , whereas the BPM offsets b_i are independent of momentum, variations of the beam energy (momentum) can be used to measure both parameters simultaneously. This is clear by substituting a dipole field error, ΔB_j , (equivalent to a quadrupole misalignment) for θ_j and explicitly showing the momentum dependence of **Eq. (8.64)**.

$$m_{ik} = \frac{1}{p_k} \sum_{j=1}^i e\Delta B_j \ell C_{ij}(p_k) - b_i \tag{8.65}$$

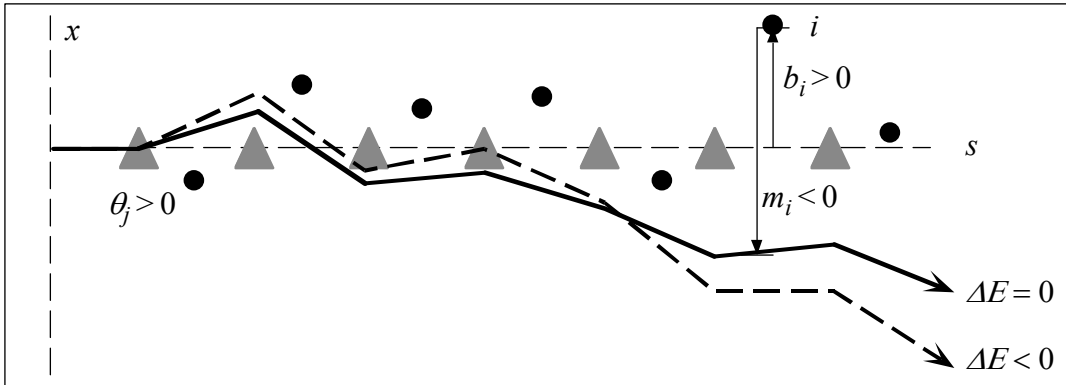


Figure 8.40 Schematic of electron trajectory for nominal beam energy ($\Delta E = 0$) and for a lower energy ($\Delta E < 0$). Undulator-induced oscillations of central trajectory not shown.

Here ℓ is the dipole length, e is the electron charge, and the subscript k on momentum and BPM readback is introduced to indicate the different values of beam momentum. The transfer coefficients, $C_{ij}(p_k)$, also include a momentum dependence, except in the case of no focusing. As a simple example, this no-focusing case is graphically represented in **Figure 8.41** as a linear dependence of m_i on $1/p$ plus an offset, b_i . The measurement then reduces to a line-fit where the slope is equal to the summation term in **Eq. (8.65)** and the offset is equal to $-b_i$. The general case, including quadrupole focusing, is similar but does not appear as the simple line-fit shown.

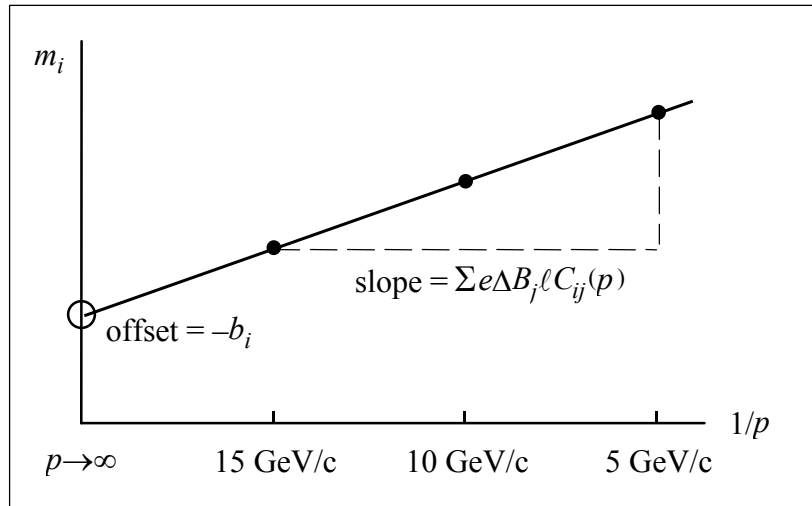


Figure 8.41 Graphical representation of **Eq. (8.65)**. The BPM readback is linear with $1/p$, has a slope equal to the summation term, and an offset equal to $-b_i$. The plot is linear only if the C_{ij} elements are momentum-independent (e.g., no focusing).

The solutions are more effectively obtained in a linear fit using all BPMs and energies simultaneously. A matrix expression for this linear system is given in **Eq. (8.66)**. Here the elements $P_{ij}(k) \equiv eC_{ij}/p_k$ are the scaled momentum-dependent transfer coefficients which map the

j^{th} kick to the i^{th} BPM. The equation, as written here, also indicates N BPMs, N kicks and two different momenta ($k = 1, 2$).

$$\begin{array}{c}
 \left. \begin{array}{c} m_{11} \\ m_{21} \\ \vdots \\ m_{N1} \\ m_{12} \\ m_{22} \\ \vdots \\ m_{N2} \end{array} \right\} = \begin{array}{c} \left[\begin{array}{cccccccc} -1 & 0 & \cdots & 0 & P_{11}(1) & 0 & \cdots & 0 \\ 0 & -1 & \cdots & 0 & P_{21}(1) & P_{22}(1) & \cdots & 0 \\ \vdots & \vdots & \ddots & \vdots & \vdots & \vdots & \ddots & \vdots \\ 0 & 0 & \cdots & -1 & P_{N1}(1) & P_{N2}(1) & \cdots & P_{NN}(1) \\ -1 & 0 & \cdots & 0 & P_{11}(2) & 0 & \cdots & 0 \\ 0 & -1 & \cdots & 0 & P_{21}(2) & P_{22}(2) & \cdots & 0 \\ \vdots & \vdots & \ddots & \vdots & \vdots & \vdots & \ddots & \vdots \\ 0 & 0 & \cdots & -1 & P_{N1}(2) & P_{N2}(2) & \cdots & P_{NN}(2) \end{array} \right] \cdot \left. \begin{array}{c} b_1 \\ b_2 \\ \vdots \\ b_N \\ \Delta B_1 \ell \\ \Delta B_2 \ell \\ \vdots \\ \Delta B_N \ell \end{array} \right\}
 \end{array} \quad (8.66)$$

There are a very large number of undulator poles along the undulator (3762) and therefore too many to determine, so the BPM data are fitted to quadrupole magnet misalignments and BPM offsets only. Therefore, any BPM readback sensitivity to energy change will be identified as upstream quadrupole offsets, and the determined quadrupole misalignments (in the wiggle-plane) will necessarily be biased in order to best cancel the net dipole error (i.e., real localized pole errors plus quadrupole misalignment). The quality of this cancellation is examined in the simulation section described below. The non-wiggle plane has no dipoles and therefore the determined quadrupole positions in this plane will not be biased (unless pole roll errors or other stray magnetic fields exist). This is a significant advantage for the energy scan technique because all bend fields, without explicit knowledge of their source, are approximately canceled by biasing the final quadrupole positions in order to best remove the trajectory's sensitivity to energy variations.

To explicitly write **Eq. (8.66)** in terms of quadrupole misalignments, $\Delta B_j \ell$ is replaced with the quadrupole magnet misalignment Δx_j , and $P_{ij}(k)$ is replaced with

$$P_{ij}(k) \rightarrow [1 - Q_{11}^j(k)] R_{11}^{ji}(k) - Q_{21}^j(k) R_{12}^{ji}(k). \quad (8.67)$$

Where $Q_{11}^j(k)$ and $Q_{21}^j(k)$ are the thick-lens transfer matrix elements across the j^{th} quadrupole magnet evaluated at the k^{th} momentum, and $R_{11}^{ji}(k)$ and $R_{12}^{ji}(k)$ ($=C_{ij}$) are the position-to-position and angle-to-position, respectively, transfer matrix elements from the exit of the j^{th} quadrupole to the i^{th} BPM, also evaluated at the k^{th} momentum. Note, a thin lens quadrupole of pole-tip field B , radius r , and length ℓ has a focal length $f = rp/B\ell$. Then the right side of **Eq. (8.67)** reduces to $-C_{ij}(k)/f$, where the minus sign indicates that a horizontally focusing quadrupole ($1/f < 0$) displaced in the positive direction ($\Delta x > 0$) will kick the beam in the positive direction.

In practice, the linear system of **Eq. (8.66)** is solved by imposing 'soft-constraints' on the solutions to stabilize the system. The inclusion of the soft-constraints is equivalent to including the additional known information that the quadrupole and BPM offsets are zero to within a reasonable scale (e.g., ~ 1 mm). The constraints are not hard limits but rather weight the fit error

(χ^2) such that the solutions do not wander out to large values over long distances (see Ref. [55]). **Eq. (8.68)** shows the standard least-squares minimization where additional ‘soft-constraints’ are included for the BPM and the quadrupole offsets (last two terms) [56]:

$$\chi^2 = \sum_{i,k} \left\{ \frac{1}{\sigma_{m_i}} \left(m_{ik} - \left[\sum_{j=1}^i P_{ij}(k) \Delta x_j - b_i \right] \right) \right\}^2 + \sum_{i=1}^N \left\{ \frac{\Delta x_i}{\sigma_x} \right\}^2 + \sum_{i=1}^N \left\{ \frac{b_i}{\sigma_b} \right\}^2 \quad (8.68)$$

The BPM and quadrupole offsets are weighted by their respective soft-constraints, σ_x and σ_b (≈ 1 mm is used in the initial simulations to follow), and the fit deviations are weighted by the measurement error of the BPM reading, σ_{m_i} (i.e., the estimated BPM resolution—in this case ~ 1 μ m rms). The solutions are then found in the usual way where the gradient of χ^2 with respect to the solutions, Δx_i and b_i , is set to zero and the resulting linear system is solved.

Ignoring the initial launch conditions of the beam at the entrance to the undulator in **Eq. (8.66)** has the effect of defining the reference line for the determined BPM and quadrupole misalignments (b_i and Δx_j) as the incoming position and angle of the beam. At a point when **Eq. (8.66)** has been solved and the N values of b and Δx are available, a best line fit (initial position and angle) is extracted from these data and the launch conditions are accordingly adjusted with steering dipoles prior to the undulator so that the quadrupole and BPM offset corrections will not systematically follow these initial erroneous launch conditions. This also limits the size of the quadrupole and BPM offset corrections applied. On the next application of the procedure, the launch conditions will be much closer to the axis defined by the initial BPM and quadrupole positions (the initial tunnel survey).

The advantage to scanning the beam energy, compared with scanning quadrupole field strengths, is that the energy-scanned BPM data is sensitive to all bending fields whether due to quadrupole misalignments, undulator pole errors or other stray fields such as the earth’s field. By using this field sensitive data, the solutions obtained provide the best minimization of all bending by biasing the quadrupole positions slightly offset with respect to the beam centroid. The net effect is to produce minimal erroneous bending within the undulator, even without explicit knowledge of the fields. Given undulator pole field errors and other stray fields, this produces a much straighter trajectory than is obtainable by varying quadrupole field strengths.

8.12.1.2 Simulation Results

Simulations have been run for the entire beam-based alignment algorithm, from initial rough steering through final precision alignment. The simulations use 32 quadrupoles and 32 BPMs within the undulator, where the quadrupoles are separated by 3.68 m (center-to-center) and have a field gradient of 107 T/m and length of 5 cm. One high-resolution BPM is located at the upstream face of each quadrupole, and each quadrupole is mounted on a mechanical mover. The weak natural field gradients of a real undulator segment are not included in this simulation, but a large energy error is included.

A conservative set of statistical and systematic errors is included in the simulations as summarized in **Table 8.10**. The undulator poles are assumed to have random uncorrelated relative field strength errors of 0.04% rms. In fact, shimming techniques used to correct the pole fields will introduce pole-to-pole field error correlations, which are more forgiving than uncorrelated errors. The 0.04% random uncorrelated error used here (in the wiggle-plane only) is therefore considered as something of a worst case. Sensitivities of the final results to the size of the input errors are studied in the next section.

Table 8.10 List of errors used in simulation of beam-based alignment procedure. All random errors have gaussian distributions.

Description	Value	Unit	Comments
BPM rms resolution	1	μm	net resolution—not necessarily single pulse
BPM offsets (uncorrelated)	50	μm	rms BPM-to-BPM survey and/or electrical offsets
BPM offsets (correlated)	300	μm	rms BPM ‘random walk’ over length of undulator
BPM mean calibration errors	10	%	mean calibration error over all BPMs
BPM rms calibration errors	3	%	rms calibration error spread over all BPMs
quad. offsets (uncorrelated)	50	μm	rms quad-to-quad trans. alignment survey errors
quad. offsets (correlated)	300	μm	rms quad ‘random walk’ over length of undulator
mean beam energy error	2.0	%	mean error of electron beam energy over the scan
rms beam energy error	0.5	%	rms error of electron beam energy over the scan
quad. mean gradient errors	0.3	%	mean gradient error over all quadrupoles
quad. rms gradient errors	0.3	%	rms gradient error spread over all quadrupoles
undulator pole errors	0.04	%	rms uncorrelated field errors over all poles
mover mean calibration errors	5	%	mean calibration error over all magnet movers
mover rms calibration errors	3	%	rms calibration error spread over all magnet movers
incoming trajectory bias	10	σ	initial orbit pos. and ang. in beam size units (static)
incoming orbit jitter	0-0.1	σ	rms orbit variation in beam size units (dynamic)

A beam energy error simulates the imprecise knowledge of the electron energy during the scan. A 2% average error (constant over the scan) and a 0.5-% rms error (variable over the scan) are included. In the table, the ‘correlated’ BPM and quadrupole offsets (misalignments) define a random walk where the expectation value of the square of the misalignment, $\langle \Delta x^2 \rangle$, is related linearly to its distance from the undulator entrance [57]. This treatment approximates the long undulator survey ‘wander’ error arising over 120 meters. In this case, an rms level of 100 μm per 10 meter length, or $\sim 300 \mu\text{m}$ over 100 meters is included. The BPMs and quadrupoles both follow the same random walk plus an additional 50 μm rms ‘uncorrelated’ component applied to both BPMs and quadrupoles separately. Two adjacent elements are therefore misaligned with

respect to each other by $\sqrt{2} \times 50 \mu\text{m} \approx 70 \mu\text{m}$ rms. Over longer distances the relative misalignment increases.

The 1- μm BPM resolution listed is the net rms measurement resolution over many pulses. Averaging can also be used to get better resolution (i.e. 100 pulses are saved at each energy, the BPM single-pulse resolution can be closer to 10 μm). The BPM offsets must, however, be constant to a level of $\sim 1 \mu\text{m}$ over the few hour period during which the energy is being scanned. This implies, for example, adequate temperature stability for the BPM electronics, etc. The various ‘calibration’ errors in the table imply that the BPMs (or magnet movers) are misscaled so that, for example, an actual displacement of 100 μm will read back as 110 μm . The ‘incoming trajectory bias’ is a static (constant) beam launch error which is ten times that of the rms beam size in both position and angle ($\sim 10 \times 30 \mu\text{m}$ and $\sim 10 \times 1.5 \mu\text{rad}$). The ‘incoming orbit jitter’ is a randomly varying launch position and angle error, which occurs during the energy-scan data acquisition. The simulation shown here includes no orbit jitter, but in fact the results are insensitive up to a 10% rms launch jitter. The jitter can actually be reduced even further in practice, to a level of a few percent, by acquiring ~ 100 orbits and using the 8-10 pre-undulator BPMs to select only those orbits which produce a constant mean trajectory launch. In addition, the variable trajectory can be included as additional fit parameters; an option which was found to be unnecessary in these simulations.

A mover reproducibility error has also been studied [58], which provides a small random mechanical error on the final position of the quadrupole magnet mover. This effect has been ignored here since small dipole steering coils will be used to augment the magnet movers and provide a very fine vernier steering control. The quadrupole magnet movers are then controlled to a level of a few microns, and the steering coils are used for smaller corrections. Without the steering coils the magnet movers would require a mechanical reproducibility precision of $< 1 \mu\text{m}$.

The undulator alignment procedure for initial machine startup is outlined in **Table 8.11**. The machine time required for each step is only a rough estimate. Practical experience and computer automation may significantly reduce these time estimates. The initial step specifies reducing the strength of the 2nd bunch compressor chicane in order to increase the bunch length in the undulator to $\sim 150 \mu\text{m}$ rms. Although not studied in detail, this should alleviate transverse resistive wall wakefields as a source of systematic error, which may otherwise be significant when large trajectory excursions occur during the alignment procedure. Geometric wakefields increase with a longer bunch, but should still be quite weak with a 150- μm bunch length.

Figure 8.42 shows the specific quadrupole and BPM misalignments used in this simulation with respect to a line defined by the linac beamline axis (as are all figures in this section unless otherwise noted). In this plot only, the initial BPM offsets are shown (blue diamonds). In plots to follow, the actual *readbacks* of the BPMs, including noise and calibration errors, are shown (green circles).

Table 8.11 Beam-based undulator alignment procedure. Beam energy is 14.3 GeV unless otherwise noted, as in step-3.

Step #	Description
0	Adjust the 2 nd bunch compressor chicane for a ~150 μm rms electron bunch length to minimize transverse wakefields in the undulator
1	Adjust the launch using best position and angle fit to 1 st six undulator BPMs
2	Apply weighted steering to reduce (not zero) simultaneously both the absolute BPM readings ($\pm 50 \mu\text{m}$) and the applied magnet mover changes ($\pm 50 \mu\text{m}$)
3	Save ~100 sets of BPM readings for each of 5, 10 & 14.3 GeV beam energies while scaling upstream linac magnets to the new energy each time
4	Run BPM data through analysis program to determine BPM and quadrupole offsets (select from data sets to minimize orbit jitter)
5	Adjust launch position and angle to remove determined linear component of BPM and quadrupole offsets
6	Move quadrupoles to new positions and correct BPM offsets in software
7	Fine steer offset-corrected BPM readings to approximately zero using a minimum number of magnet movers and steering coils
8	Repeat steps 3-7 until peak BPM readings at 5 GeV are $< 15 \mu\text{m}$

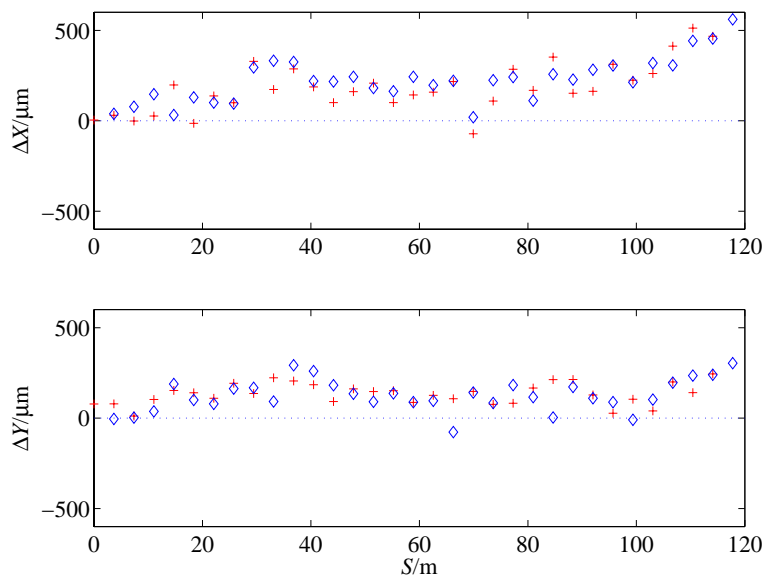


Figure 8.42 Quadrupole (red-cross) and BPM (blue-diamond) initial misalignments used in the simulation, with respect to the line defined by the linac beamline axis.

The resultant, un-steered horizontal and vertical beam trajectory through the undulator is shown in **Figure 8.43** (prior to step-1, **Table 8.11**). The true orbit (blue solid line) is shown, as in

plots to follow, every 1.5 cm along the undulator, at the center of every pole of ~ 8000 poles. The BPM readbacks (green circles) are, in practice, the only known (measured) quantities. This trajectory is an example of the first beam pulse in the newly installed undulator.

The first correction (step-1, **Table 8.11**) is to rough-steer the incoming trajectory based on the first six BPM readbacks in the undulator, which are used in a best fit to an incoming betatron oscillation (see black dashed line in first 20 meters of **Figure 8.43**). **Table 8.12** shows the initial launch conditions for this simulation both before and after the step-1, **Table 8.11**, rough correction. At this rough stage, direct use of the first few BPM readbacks, before their offsets are corrected, is still very effective in removing large incoming launch errors.

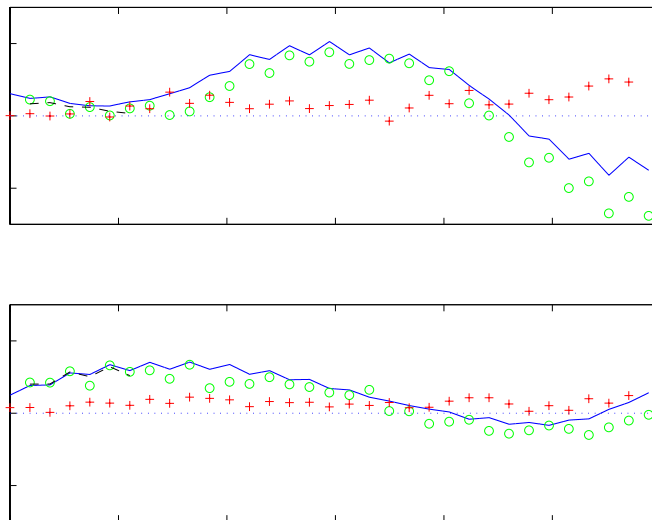


Figure 8.43 Simulated first beam trajectory (blue-solid) through the newly installed undulator, including incoming trajectory bias of $-300 \mu\text{m}$ and $-15 \mu\text{rad}$. Also shown are BPM readbacks (green-circle), quadrupole positions (red-cross), and the fitted initial launch using the readbacks of the first six BPMs (dash—first 20 meters only).

The launch conditions are significantly improved in this case, reducing the trajectory amplitude and, given systematic errors such as BPM calibration and quadrupole field gradient errors, improving the speed of convergence of the algorithm. A complete correction is not possible at this stage since the BPMs used in the launch fit may include large offsets, and the misaligned quadrupoles between the BPMs may kick the trajectory off of a free betatron oscillation. Note, the quality of this correction is dependent on the specific set of misalignments (random seed). The random seed shown here is fairly typical. The quality of this correction impacts only the speed of convergence.

Table 8.12 Initial launch conditions at undulator entrance before and after step-1, **Table 8.11** correction.

Launch parameter	Before Step-1, Table 8.11	After Step-1, Table 8.11
$\langle x \rangle$	310 μm	14 μm
$\langle x' \rangle$	14 μrad	3.5 μrad
$\langle y \rangle$	250 μm	13 μm
$\langle y' \rangle$	17 μrad	-1.7 μrad

Step-2, **Table 8.11**, involves a weighted steering procedure using the undulator quadrupole magnet movers where the absolute readings of the BPMs are minimized with respect to a 50 μm weighting and the applied magnet mover changes are simultaneously minimized with respect to a 50 μm weighting. Without this weighting the magnet movers can move by up to ~ 1 mm in order to exactly zero each BPM reading which, due to the large BPM offsets, is an unnecessary and undesirable steering accuracy at this early stage. With the weighting included, the movers change by ~ 50 μm , which is sufficient to correct the large trajectory deviations of **Figure 8.43**. **Figure 8.44** shows the trajectory after the step-2 weighted steering is applied. This step simply improves the trajectory before the energy is changed.

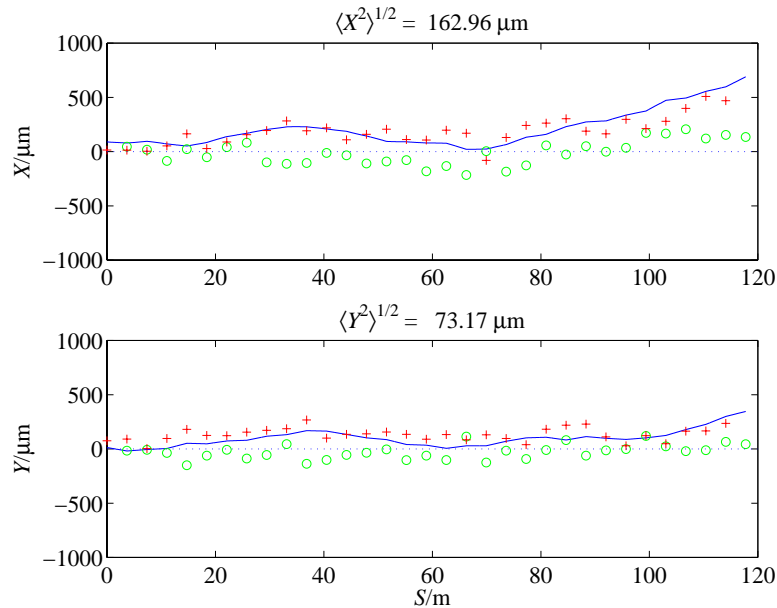


Figure 8.44 Trajectory (blue-solid) at 14.3 GeV after application of step-2, **Table 8.11**, weighted steering. BPM readbacks (green-circle) and applied magnet mover changes are both minimized with respect to a 50 μm weighting. The post-steering quadrupole positions (red-cross) are also shown. These BPM readings are saved for analysis.

These 14.3-GeV BPM data are saved and the energy is then lowered to 10 GeV by switching off half of the klystrons in linac-3. The fields of the magnets upstream of the undulator are scaled to the new energy and any beam position differences upstream of the undulator, with respect to

the 14.3-GeV orbit, are manually corrected, if necessary, until the launch position at 10 GeV is within $\pm 3 \mu\text{m}$ of that at 14.3 GeV. Note, any beam *angle* difference originating at the undulator entrance will not be detectable with the BPMs upstream of the undulator. However, this angle will eventually be properly incorporated into a correction of the transverse position of the first undulator quadrupole. **Figure 8.45** shows the new trajectory at 10 GeV, while **Figure 8.46** shows a third trajectory at 5 GeV (most of the linac-3 klystrons switched off). No changes are made to the undulator components during the energy scan. Only the pre-undulator trajectory is adjusted, if necessary, to maintain a constant beam position at the undulator entrance.

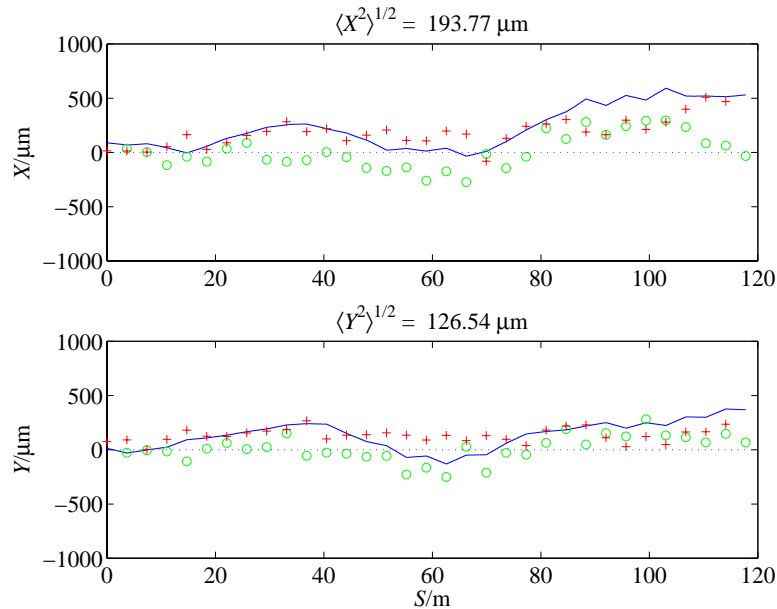


Figure 8.45 Trajectory (blue-solid) at 10 GeV. BPM readbacks (green-circle) and quadrupole positions (red-cross) are also shown. These BPM readings are saved for analysis.

Since the fields of the magnets upstream of the undulator will be scaled to the lower energies, the beta functions at the undulator entrance will be constant during the procedure. Since the undulator focusing is accomplished with permanent magnet quadrupoles, a betatron-mismatch, with respect to the energy dependent periodic beta functions of the undulator FODO lattice, will propagate through the undulator at the lower beam energies. In the worst case (5 GeV) the beam size will beat at twice the betatron frequency reaching a peak rms size of $\sim 80 \mu\text{m}$ as compared to the $50 \mu\text{m}$ beam size of the 5-GeV periodic beta functions. This worst-case beat in beam size should have no significant effect on the alignment procedure, which utilizes trajectory centroid information only.

With the 5, 10 and 14.3-GeV BPM readback data saved, the analysis program is run, which calculates BPM offsets, and quadrupole magnet positions with respect to the step-1-corrected incoming beam position and angle. **Figure 8.47** shows the calculated quadrupole offsets as well as the true offsets (used in the simulation). The fine structure of the calculated offsets agrees well with the true offsets. The values differ, however by a straight line which is due to both 1) the

step-1-corrected launch bias, and 2) the correlated component of the BPM and quadrupole offset errors (the random walk-off effect of the initial survey). A line is then fit to the calculated BPM and quadrupole offsets. The slope and offset of the best line fit is used to readjust the initial launch position and angle at the undulator entrance.

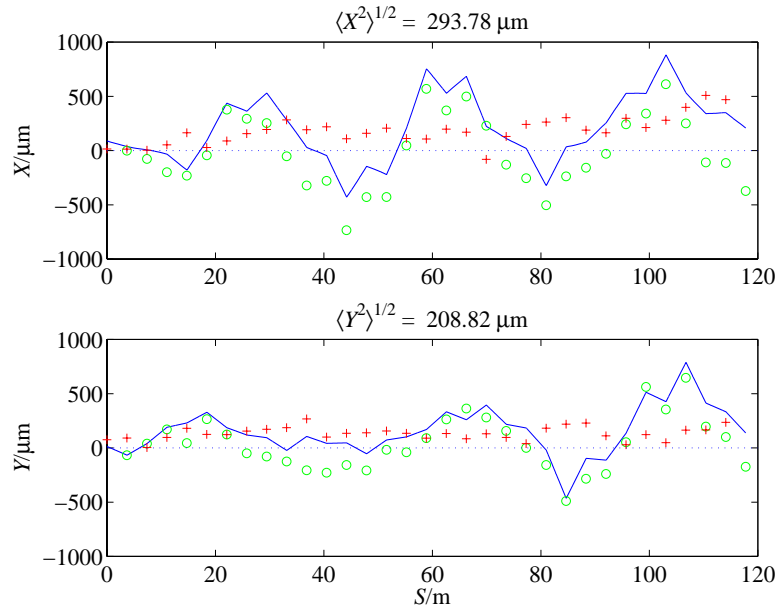


Figure 8.46 Trajectory (blue-solid) at 5 GeV. BPM readbacks (green-circle) and quadrupole positions (red-cross) are also shown. These BPM readings are saved for analysis.

Figure 8.48 shows the new electron trajectory after the launch conditions, the quadrupole magnet movers and the BPM offsets are corrected. The BPM offsets and the mover corrections applied are the differences between the best line fit and the data (error bars). In addition, a final steering using a minimum number of steering coils is applied to remove any remaining detectable betatron oscillation (based on BPM readback). At each stage in the simulation, the real magnet mover limitations (calibration errors) and BPM errors (calibration and resolution) are incorporated.

The linear component, which remains in the **Figure 8.48** trajectory is due to the correlated quadrupole and BPM offsets (random walk of initial tunnel survey). Since these offsets are due dominantly to the difference between the line defined by the linac beamline axis and the slightly different line established by the undulator beamline, the alignment procedure inevitably launches the electrons straight down the undulator vacuum chamber, which presumably follows these correlated tunnel survey errors. The true trajectory shown in **Figure 8.48** is then actually the most desired trajectory, where a slight change in beam

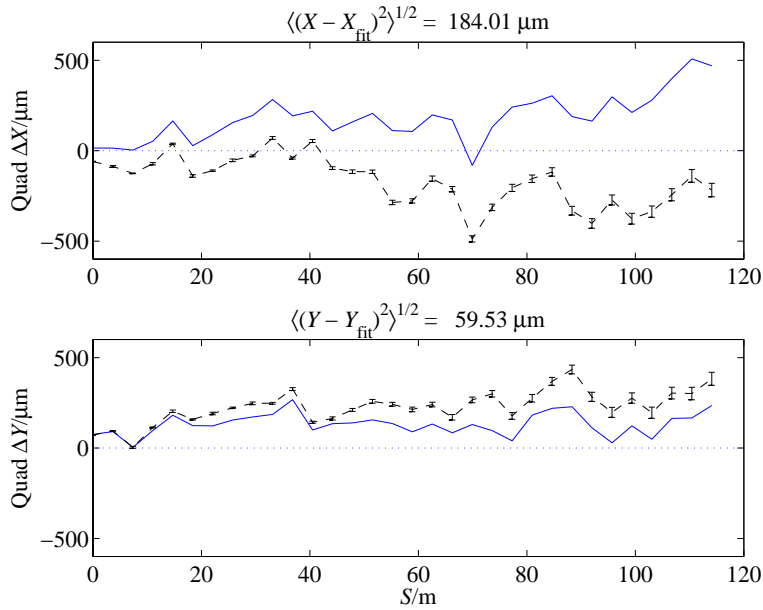


Figure 8.47 True (blue-solid) and calculated (black-dash) quadrupole positions. The BPM offsets are similar but not shown here. The fine structure is reproduced well.

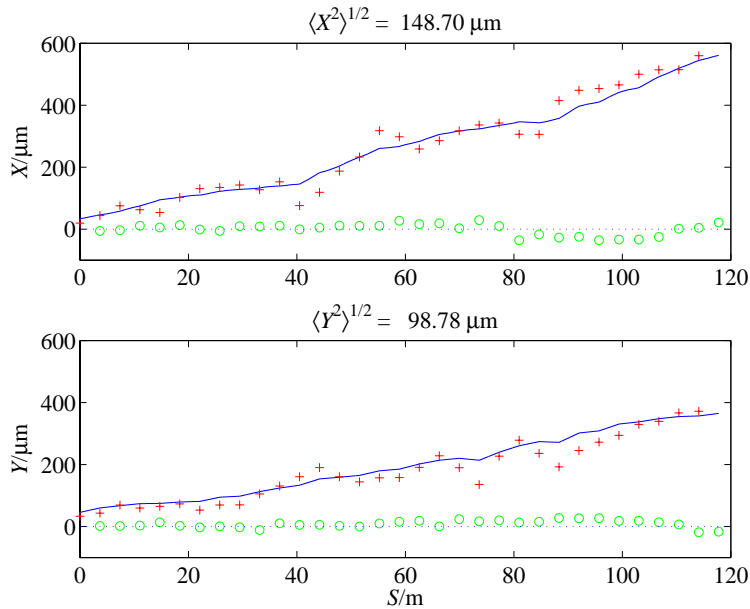


Figure 8.48 Trajectory (blue-solid) at 14.3 GeV after one iteration of steps 1-7. BPM readbacks (green-circle) and quadrupole positions (red-cross) are also shown. The trajectory is fairly straight but does not necessarily follow the line established by the linac axis. This is due to the correlated BPM and quadrupole misalignments (random walk of the initial tunnel survey).

position and angle at the undulator entrance is used to launch the electron beam down the center of the undulator, and the beam follows along near the center of the quadrupoles. The tiny

dispersion generated by this slight position and angle change is completely negligible, especially in consideration of an rms relative energy spread of <0.1%.

Figure 8.49 shows the same data as in **Figure 8.48** except that the linear component of the true orbit has been removed in order to show more clearly the straightness of the trajectory. **Figure 8.50** shows this linear-corrected view of the final trajectories after a second iteration of steps 3-7 is applied, and **Figure 8.51** shows this view after a third iteration. Each plot lists the rms of the real trajectory, $\langle \Delta X^2 \rangle^{1/2}$, the rms of the BPM readings, $\langle \Delta X_{BPM}^2 \rangle^{1/2}$, and the rms quadrupole alignment, $\langle \Delta X_{QUAD}^2 \rangle^{1/2}$. The rms of the electron trajectory over the length of the undulator with respect to a straight line achieves a value of <8 μm after the 2nd iteration and <3 μm after the 3rd iteration. The BPM readbacks achieve an rms level of 1 μm , while the quadrupoles are aligned to 11 μm and 7 μm in x and y respectively. The x alignment is worse since the positions of the magnets are slightly biased in order to best correct the net dipole field, including undulator pole errors.

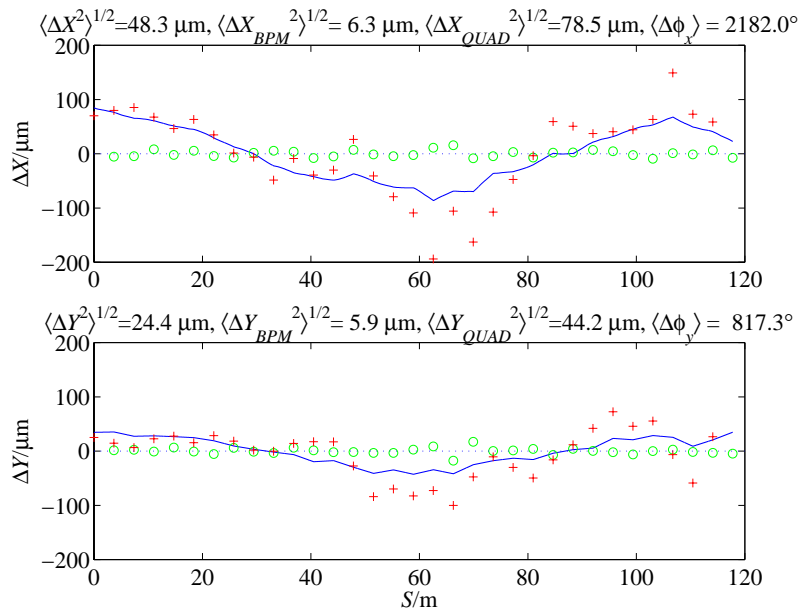


Figure 8.49 Trajectory (blue-solid) at 14.3 GeV, with linear component removed, after one iteration of steps 1-7. BPM readbacks (green-circle) and quadrupole positions (red-cross) are also shown. The quadrupole positions are shown in the same linear-corrected coordinates of the true orbit. The beam trajectories with respect to a straight line over the undulator length (for this first pass correction) have rms values of $x_{rms} = 48 \mu\text{m}$, $y_{rms} = 24 \mu\text{m}$ and peak values of $x_{pk} = 86 \mu\text{m}$, $y_{pk} = 43 \mu\text{m}$.

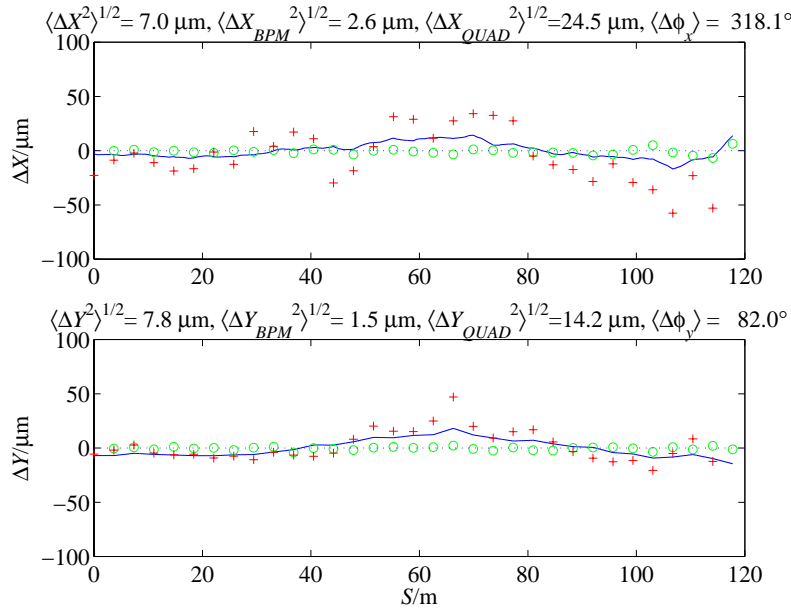


Figure 8.50 After two iterations of steps 3-7 ($x_{rms} = 7.0 \mu\text{m}$, $y_{rms} = 7.8 \mu\text{m}$ and peak values of $x_{pk} = 17 \mu\text{m}$, $y_{pk} = 18 \mu\text{m}$). A new scale is used here.

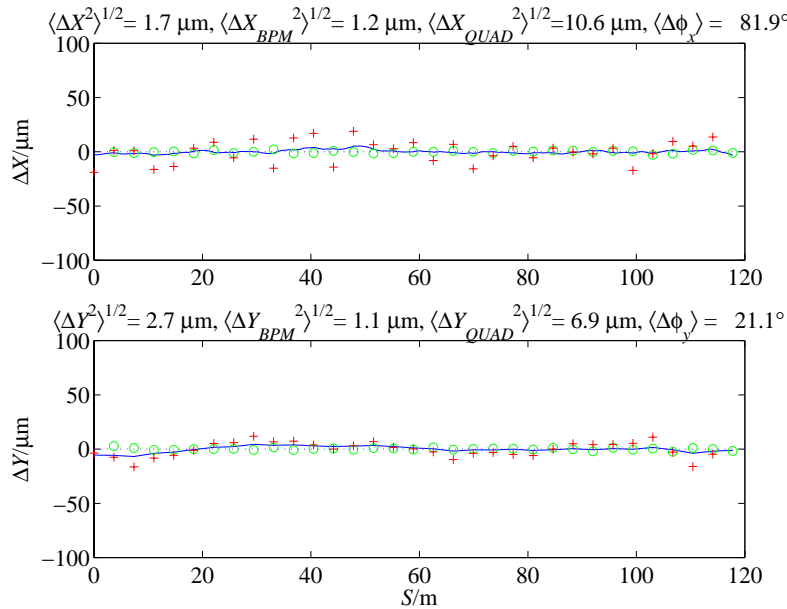


Figure 8.51 After three iterations of steps 3-7 ($x_{rms} = 1.7 \mu\text{m}$, $y_{rms} = 2.7 \mu\text{m}$ and peak values of $x_{pk} = 5.3 \mu\text{m}$, $y_{pk} = 6.8 \mu\text{m}$).

The raw BPM readbacks also give a clear indication as to whether the procedure is converging and when to terminate the process. As the alignment is improved, the BPM readbacks will respond less and less to energy variations. With the energy lowered to 5 GeV the BPM readings should change, with respect to the readbacks at 14.3 GeV, by $<15 \mu\text{m}$ when the procedure has converged to the level shown here. In these simulations at 5 GeV, the peak

readings change by $<150 \mu\text{m}$ after the second pass and by $<15 \mu\text{m}$ after the third pass. In practice, this should provide a clear convergence signal.

To further evaluate the quality of the final trajectory obtained, the trajectory simulation data are used to calculate the total path length of the electrons over the length of the undulator. The electron path length is compared with the path length of a 1.5-\AA -wavelength x-ray beam that follows a perfectly straight path down the center of the undulator. A phase slip error is then calculated for each plane, $\langle\Delta\phi_x\rangle$ and $\langle\Delta\phi_y\rangle$, with the total phase error as the sum. The results are shown on each trajectory plot for each iteration pass. The final trajectory after the third correction reduces the phase error to $\langle\Delta\phi_x\rangle \approx 82^\circ$ and $\langle\Delta\phi_y\rangle \approx 21^\circ$, for a total phase error of $\langle\Delta\phi_x\rangle + \langle\Delta\phi_y\rangle \approx 103^\circ$. The horizontal phase error is larger than the vertical due to the undulator pole errors. FEL simulations using *Ginger* indicate that a total phase error of $\sim 400^\circ$ increases the saturation length by one power gain length. Finally, studies with the FEL code RON, and using the precise trajectories, which result from these simulations, also indicate a saturation length increase of less than one power gain length for the resulting simulated trajectory.

Figure 8.52 shows the final quadrupole magnet mover settings after the three iterations have been completed. The final alignment correction requires magnet mover settings with an rms value of $\sim 100 \mu\text{m}$ and maximum excursions of $\sim 350 \mu\text{m}$.

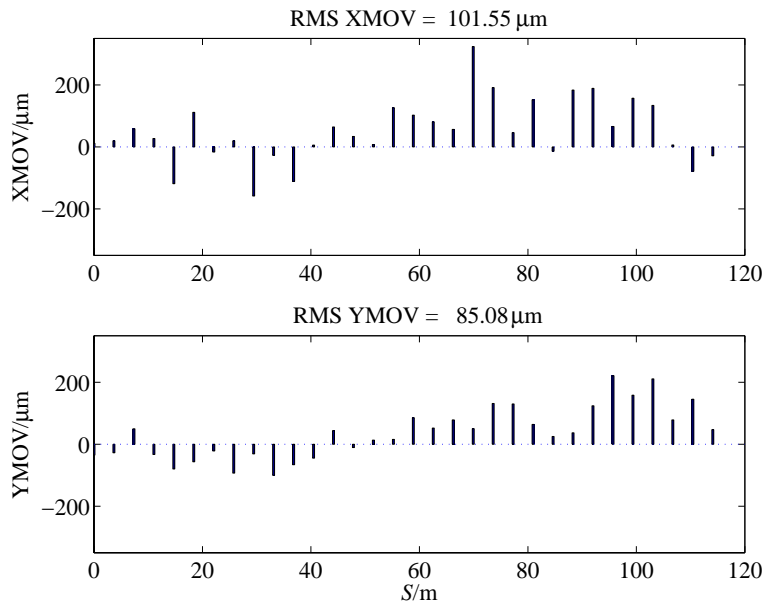


Figure 8.52 Final quadrupole magnet mover settings after three iterations of the alignment procedure. The movers are initially set to zero prior to the alignment procedure and the final rms values shown are: $x_{rms} = 102 \mu\text{m}$ and $y_{rms} = 85 \mu\text{m}$.

8.12.1.3 Sensitivities

The sensitivities of the final rms trajectory to the simulation input errors are summarized below in **Table 8.13**. A new simulation is run using the input errors listed in **Table 8.10**, except that for each run a different individual error is approximately doubled in value. The first row

summarizes the simulation already described, and every following row represents a new simulation where the noted error has been increased with respect to **Table 8.10**.

Table 8.13 Trajectory and phase error sensitivities to simulation input errors. All errors are those of **Table 8.10** unless noted, in which case that error has been approximately doubled in value. The random seed used is unchanged for purposes of comparison.

Increased input error	x_{rms} / y_{rms} [μm]		$\langle \Delta\phi_x \rangle / \langle \Delta\phi_y \rangle$ [deg]	
	after 2 nd pass	after 3 rd pass	after 2 nd pass	after 3 rd pass
(using all errors of Table 8.10)	7.0 / 7.8	1.7 / 2.7	318 / 82	82 / 21
2- μm BPM resolution	5.6 / 7.3	2.5 / 5.2	351 / 89	117 / 67
0.1-% rms undulator pole errors	8.0 / 7.8	2.0 / 2.7	544 / 82	350 / 21
100- μm uncorrelated BPM & quad offsets	11 / 14	2.3 / 3.2	721 / 232	112 / 29
0.6-% quad. gradient errors (mean & rms)	6.5 / 8.9	1.5 / 2.7	229 / 104	74 / 22

All errors are returned to their original values for each new run, except for the noted error. As the table demonstrates in most cases, three iterations of the alignment procedure render the algorithm fairly insensitive to the precise set of beamline errors. A doubled BPM resolution and (independently) a more-than-doubled set of pole field errors have a noticeable impact, but the rms trajectory is still $\leq 5 \mu\text{m}$ and the total phase error is $< 400^\circ$.

8.12.1.4 Long Term Stability

After beam-based alignment has achieved a straight trajectory, ground motion effects in the FFTB tunnel can slowly alter the undulator alignment. Betatron oscillations over full or partial sections of the undulator can be removed by occasional small steering corrections. Higher frequency trajectory disturbances (e.g., from BPM to BPM), however, are much more damaging and difficult to remove. When the trajectory is distorted sufficiently to impact the FEL gain, and small isolated steering corrections are no longer helpful, one single iteration of the beam-based alignment procedure will need to be repeated.

An estimate of the long term stability of alignment can be made by applying the ‘‘ATL-law’’ [59], which estimates the effects of diffusive ground motion. The variance, σ^2 , of the relative transverse alignment between two points separated by a distance, L , is described by

$$\sigma^2 = A \cdot T \cdot L, \tag{8.69}$$

where T is the time since the two points were initially aligned, and A is a site-specific constant, usually specified in units of $\mu\text{m}^2/\text{m}\cdot\text{s}$. Measurements of the coefficient A have been made at many locations on the globe, including in the actual FFTB tunnel at SLAC where the LCLS undulator will reside. A value of $A \approx 5 \times 10^{-7} \mu\text{m}^2/\text{m}\cdot\text{s}$ has been measured in the FFTB tunnel [60] and is used here to estimate the time required for which beam-based alignment must be repeated. The distance L is taken as the BPM-to-BPM spacing, since these short scale trajectory distortions cause the largest electron-to-photon phase errors, and misalignments over distances greater than,

or of the order of one power gain length have much less impact. With $L = 3.68$ m and $A = 5 \times 10^{-7}$ $\mu\text{m}^2/\text{m}/\text{s}$, a 30-day period will produce a relative misalignment of $2 \mu\text{m}$ rms between BPMs. While steering corrections will control the build-up of the trajectory amplitude caused by this slow drift, the phase errors induced by localized, short scale misalignments will eventually reduce the FEL gain. An average closed trajectory bump of $2 \mu\text{m}$ amplitude ($= \Delta x = \Delta y$) at each of $N = 32$ BPMs in both planes, at a radiation wavelength of $\lambda_r = 1.5 \text{ \AA}$, will produce a phase error of

$$\Delta\phi = \frac{2\pi N}{L\lambda_r} (\Delta x^2 + \Delta y^2) , \quad (8.70)$$

which amounts to 170° over the undulator. From this rough model it is estimated that a single iteration of the beam-based alignment procedure (~ 2.5 -hour procedure) will be required once per month.

8.12.1.5 Summary

An electron trajectory of $< 3 \mu\text{m}$ rms, with respect to a straight line over the length of the LCLS undulator, is achievable using energy scanned beam-based alignment. The electron-to-photon phase error, at 1.5 \AA , over the full undulator length can be reduced to $\sim 100^\circ$, which is completely adequate. Prior to the alignment procedure, initial BPM and quadrupole uncorrelated misalignment levels of $100 \mu\text{m}$ rms, plus $300 \mu\text{m}$ rms correlated component are correctable. Effects such as BPM and magnet mover calibration errors, quadrupole field errors, energy errors, and undulator pole field errors have been included in a detailed simulation which demonstrates this level can be achieved realistically with reasonable confidence. Only one random seed has been presented here as an example, but several seeds have been run with similar success. An estimated time of 8-12 hrs is required to accomplish the initial beam-based alignment. Based on ground motion studies in the FFTB tunnel, one 2.5-hour iteration of the procedure will be required approximately once per month to maintain the alignment.

8.13 X-Ray Diagnostics

8.13.1 Introduction

The x-ray diagnostics consists of tools for measurement and analysis of the spectral and spatial characteristics of spontaneous and SASE radiation along the undulator line. The main goal is to measure the absolute flux of x-rays as a function of the distance along the undulator line. Furthermore, the diagnostics permits verification of the overlapping of radiation cones from different undulator segments.

8.13.2 Undulator Cell Structure

The LCLS undulator line is designed as a set of standard cells shown schematically in **Figure 8.53**. Each half-cell consists of six 3.42-m long undulator segments with two 187 mm breaks and one 421 mm break between undulator segments. The short breaks are filled with the focusing or defocusing lens, electron BPMs and steering coils. The last break includes those same components and additional x-ray diagnostics.

The length of the undulator has been optimized based on the requirement of operating the LCLS with electron beam energies over the range of 4.5 GeV to 14.5 GeV. Also, it has been shown independently that the chosen cell length corresponds to the optimum position of the BPMs [61].

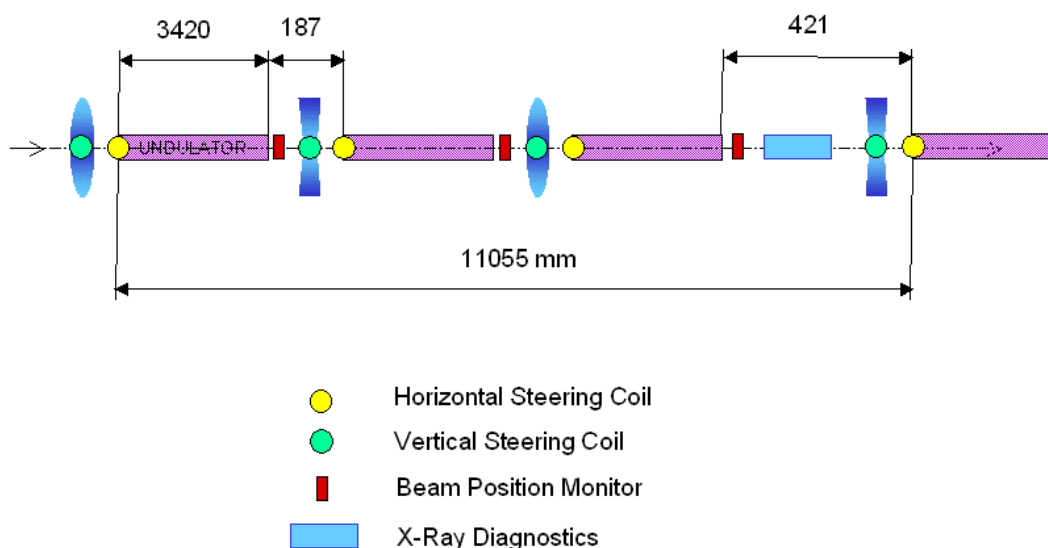


Figure 8.53 Cell structure of the LCLS undulator

8.13.3 X-Ray Diagnostics Specifications and Experimental Set-up

In order to utilize the x-ray diagnostics efficiently and meaningfully, the diagnostics should satisfy the following requirements:

- one shot sensitivity for all types of spectral, flux and spatial measurements;
- several microradian angular resolution;
- accuracy of the absolute flux measurement better than 10%; and
- many⁴ orders of magnitude in dynamic range.

An experimental set-up that meets all the above requirements is shown in **Figure 8.54**. It consists of a 200- μm -thick diamond (111) crystal monochromator, x-ray CCD cameras and a PIN diode [62]. The monochromator has a bandpass of 10^{-4} and can analyze x-ray radiation in the

⁴ For the LEUTL FEL attenuation of the radiation by as much as 9 orders of magnitude was necessary and has been achieved.

energy range from 4 to 9 keV. The combination of the monochromator and the CCD camera as an area detector is used for the spectral and spatial (angular) measurements, whereas the combination of the monochromator with the PIN diode provides absolute flux measurements along the undulator line. The OTR part of the diagnostics is described in **Section 8.11.4**.

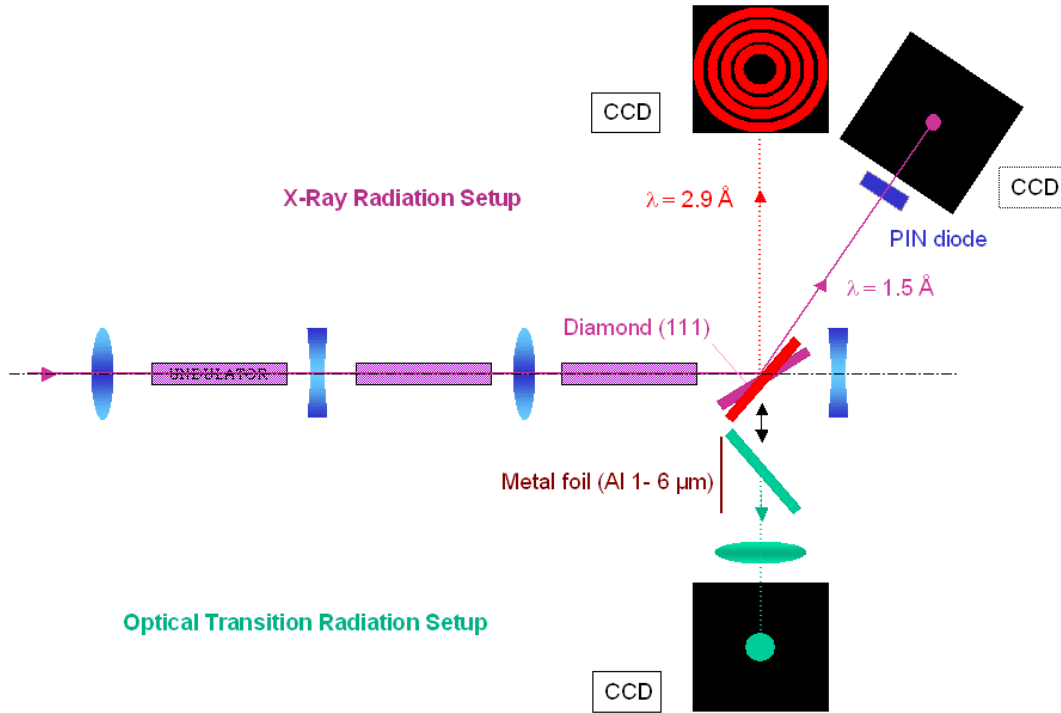


Figure 8.54 X-Ray/OTR Diagnostics setup

8.13.4 On-Axis X-Ray Diagnostics

The purpose of the on-axis x-ray diagnostics is to measure in absolute units the increase in the spectral flux along the undulator line and to provide information about the spatial distribution of radiation. In order to analyze the performance of the on-axis x-ray diagnostics, a set of calculations has been carried out using the program SRW [63] for near and far field cases.

For on-axis x-ray diagnostics, the monochromator is set at a Bragg angle of 21.35 degrees which selects the fundamental undulator harmonic at the energy of 8.27 keV. Calculations of the spectral flux generated by the undulator cell and transmitted through the monochromator yield $5 \cdot 10^6$ photons/shot, or 1.6 nC charge registered by the silicon PIN diode. A cooled silicon PIN diode could detect a single x-ray photon. The dynamic range of the PIN diode covers ten orders of magnitude without any additional filtering.

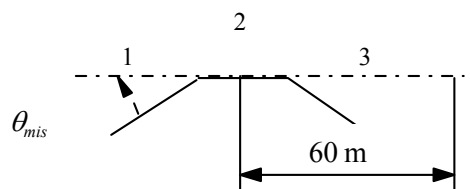


Figure 8.55 Undulator trajectories in the cell.

The x-ray diagnostics setup will provide absolute measurements (within 10%) of spectral flux after each undulator cell. The growth rate could be derived from the measured flux at successive diagnostics stations. The growth rate of the flux is a valuable means of evaluating and studying the development of the SASE process.

The spatial flux distribution for one undulator cell is the superposition of radiation from three undulator segments. In order to evaluate the sensitivity of the x-ray diagnostics to the angular misalignment of undulator segments, e-beam trajectories in the first and third undulator segments in the cell are given a missteering angle θ_{mis} (**Figure 8.55**). A series of calculations of spontaneous radiation for a cell have been performed for a nominal electron beam emittance of 0.05 nm-rad at a photon energy of 8.29 keV and at a distance of 60 m from the undulator cell. This 8.29 keV energy is detuned slightly, towards higher energy, from the fundamental energy of 8.27 keV, in order to reduce the angular divergence of the undulator radiation. The calculated spatial intensity distribution is shown in **Figure 8.56** for a missteering angle of 4 μ rad, and calculated horizontal profiles are shown in **Figure 8.57** for missteering angles of 2, 3, and 4 μ rad. The figures show that a missteering of 4 μ rad can be clearly discerned if the diagnostics station is far enough from the undulator cell.

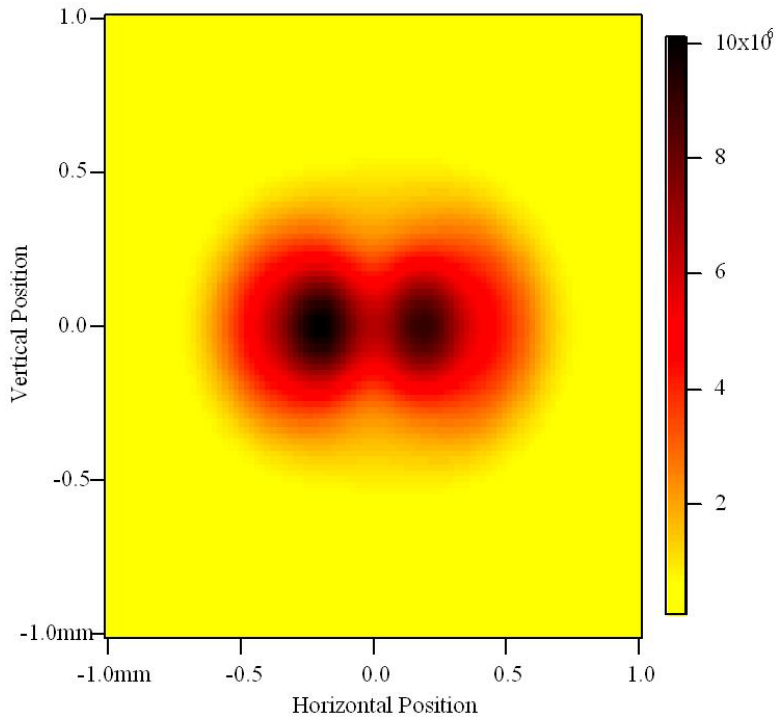


Figure 8.56 Calculated spatial distribution of the undulator radiation from a three-undulator cell with a missteering $\theta_{mis} = 4 \mu$ rad, an electron beam emittance of 0.05 nm-rad, and a photon energy of 8.29 keV, at 60 m from the undulator segments.

Measurements of the spatial distribution of radiation generated in each undulator cell will complement the electron beam-based alignment, but will not substitute for it. x-ray diagnostics will be especially useful in the first steps of the beam-based alignment procedure.

Knowing the calculated flux distribution and the efficiency of the x-ray diagnostics, one can estimate the required sensitivity of the system at 60 m, which was found to be $5 \cdot 10^2$ electrons/pixel/shot for a $7 \times 7 \mu\text{m}^2$ pixel CCD. That is substantially above the CCD noise level. Appropriate filtering in front of the CCD will keep the flux in the last diagnostics stations within the dynamic range (about 10^5 e⁻/pixel) of the detector.

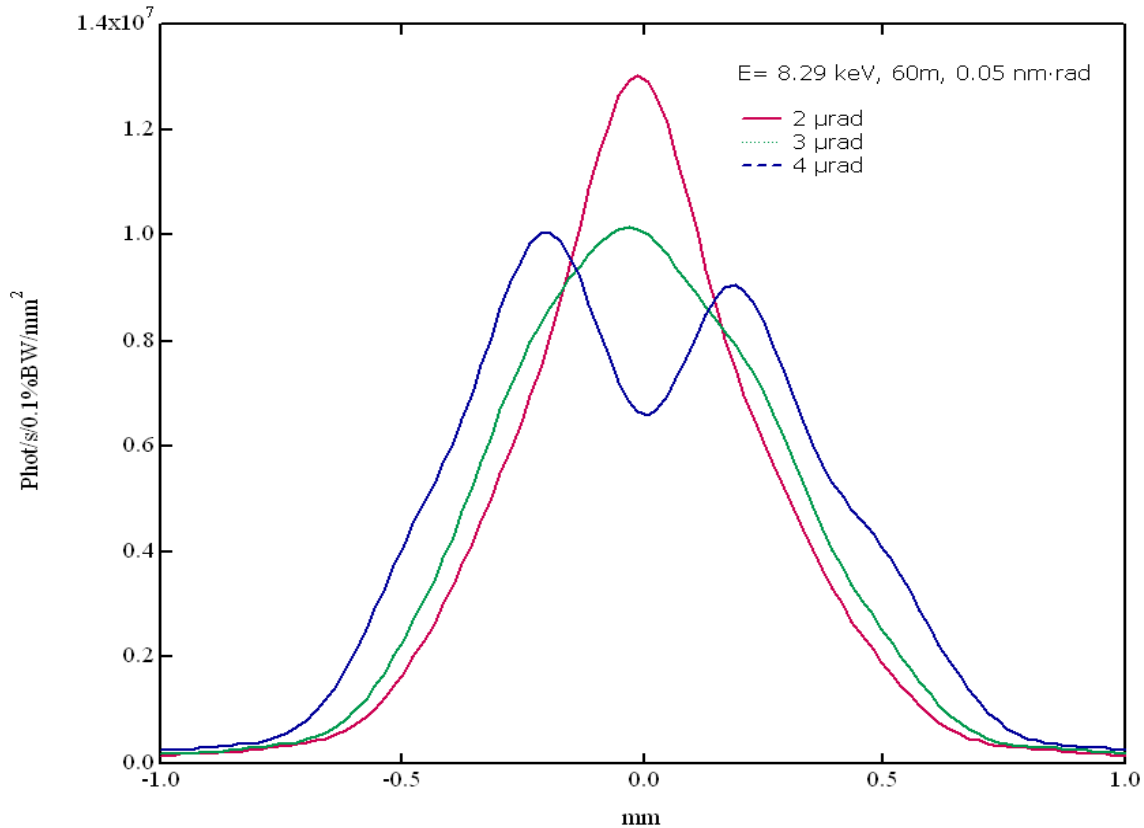


Figure 8.57 Horizontal profiles of the undulator radiation for missteering angles θ_{mis} of 2, 3 and 4 μrad .

When the on-axis diagnostics stations are in use, the electron beam will always be hitting the diamond crystal in one of the diagnostics stations. The electron beam energy loss in a 200- μm -thick diamond crystal is equal to 0.25 MeV/particle and independent of whether the beam energy is 4.5 or 14.5 GeV. As a result, a 1 nC electron beam deposits an average power of 30 mW for a 120 Hz repetition rate. Finite element analysis shows that the most simple cooling design (clamped crystal, no coolant) will lead to a 0.06 μrad slope error on the crystal, which is negligibly small compared with the 10 μrad width of the crystal rocking curve. After exiting the crystal, the electron beam will have an angular spread of 40 μrad (rms).

Recent experimental data taken at the FFTB facility at SLAC show that a diamond crystal can withstand a high energy, highly focused electron beam without any visually observed damage [64].

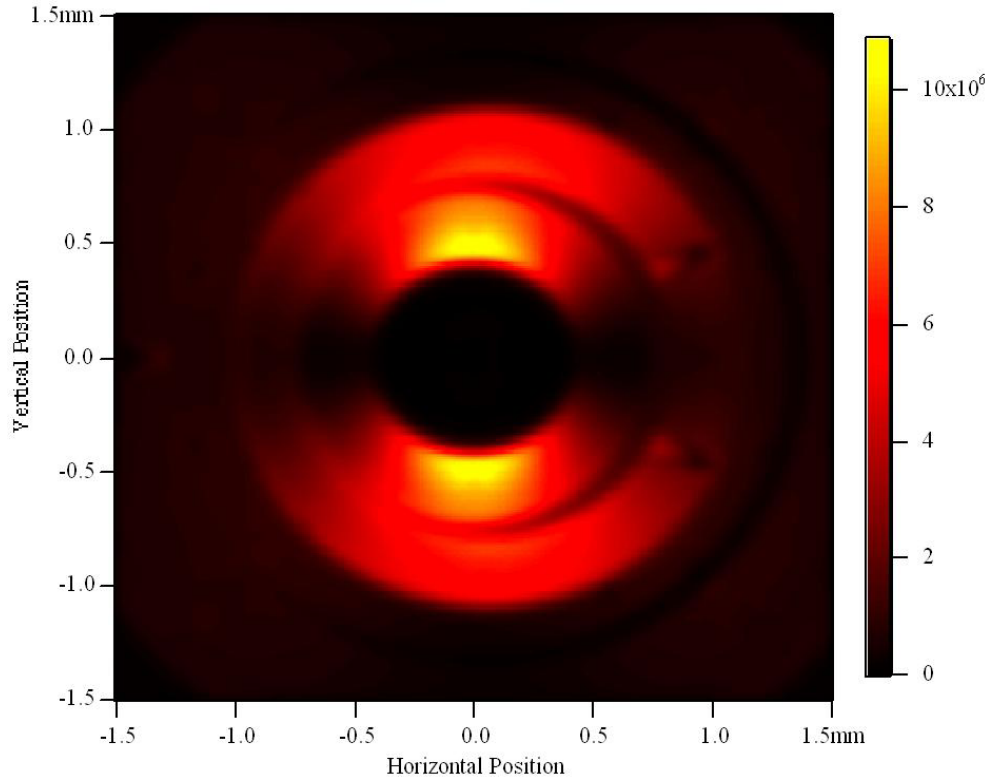


Figure 8.58 Calculated spatial distribution of the red-shifted radiation (at 4.25 keV) from two undulator segments, at 6 m from the undulator segments, and with a missteering angle θ_{mis} of 10 μ rad between the undulator segments.

8.13.5 Off-Axis X-Ray Diagnostics

The off-axis, “red-shifted” x-ray diagnostics is complementary to the on-axis diagnostics. The crystal monochromator in this case can have a small hole to let the electron beam go through unperturbed. This allows radiation to be observed from each undulator cell without any trajectory distortion. A similar technique was successfully implemented for the LEUTL diagnostics, where a mirror was used instead of the crystal.

For the “red-shifted” radiation at 4.25 keV, the crystal monochromator has a Bragg angle of 45 degrees and the angle between the CCD camera and the radiation is 90 degrees. The calculated spatial distribution of the undulator radiation at a distance of 6 m from two undulator segments is shown in **Figure 8.58**, and the horizontal profile in **Figure 8.59**. An intentional angular misalignment of $\theta_{mis} = 10 \mu$ rad has been introduced in the trajectory between the two undulator segments.

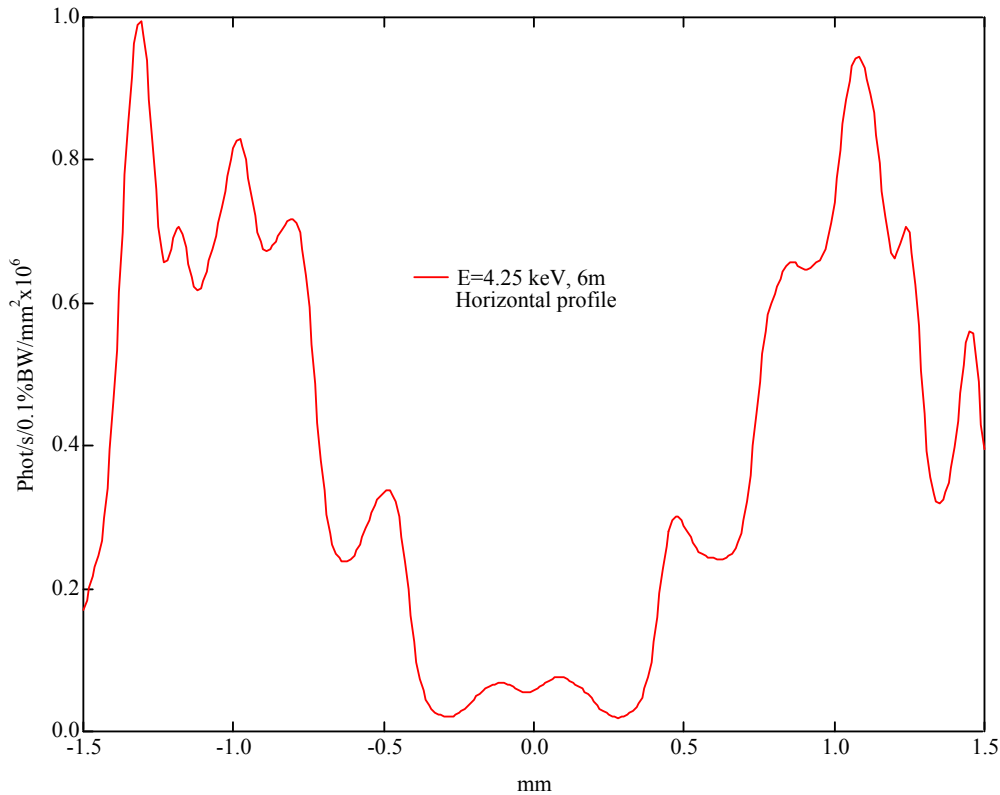


Figure 8.59 Calculated horizontal profile of the red-shifted radiation (at 4.25 keV) from two undulator segments, at 6 m from the undulator segments, and with a missteering angle θ_{mis} of 10 μrad between the undulator segments.

Calculation of the detection efficiency shows that the CCD camera will get $4 \cdot 10^2$ e^-/pixel per shot for the $20 \times 20 \mu\text{m}^2$ size pixel, which is again substantially above the CCD noise level.

8.13.6 Effects of the Electron Beam Emittance

The influence of the beam emittance on the spatial distribution of the radiation has been studied. **Figure 8.60** shows the calculated horizontal profiles of undulator radiation from two undulator segments with a missteering angle of 4 μrad between the undulator segments, for different values of the electron beam emittance.

Calculations were also done of the spatial intensity distribution and horizontal profile from a three-segment cell at 60 m from the undulator segments, with a missteering θ_{mis} of 10 μrad , and at a photon energy of 8.3 keV (detuned from the 8.27 keV fundamental to higher energy). The spatial intensity distribution for an electron beam emittance of 0.05 nm-rad is shown in **Figure 8.61**, and the horizontal profiles for three different beam emittances are shown in **Figure 8.62**. Differences between the 0.025, 0.05, and 0.1 nm-rad emittances are clearly observable.

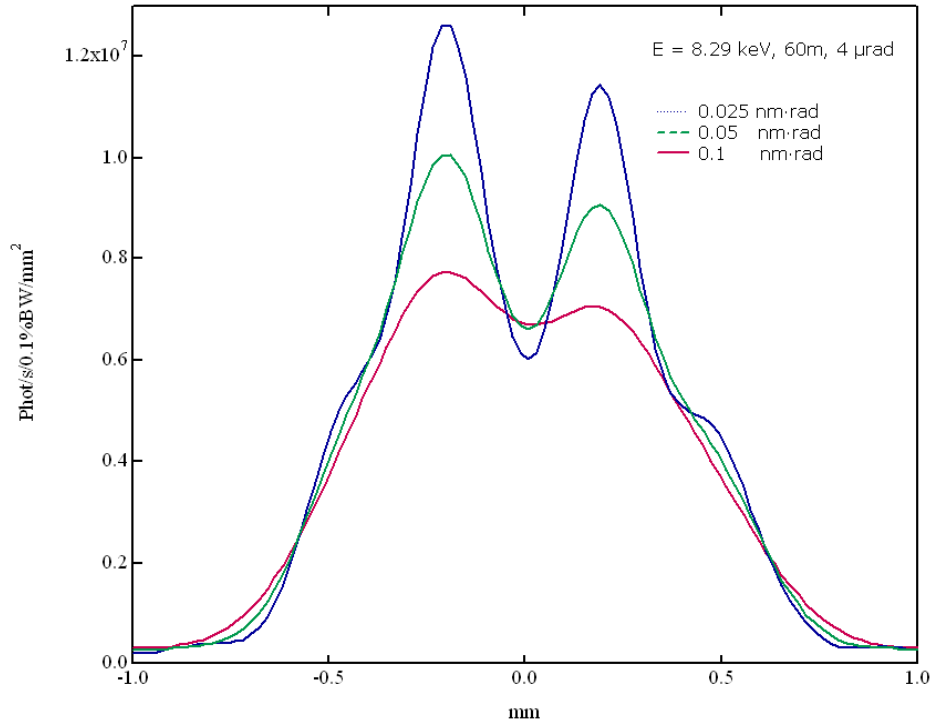


Figure 8.60 Calculated horizontal profile of the on-axis (8.29 keV) undulator radiation from two undulator segments with a missteering angle θ_{mis} of 4 μ rad between the undulator segments, at 60 m from the undulator segments. The different curves are for different electron beam emittances.

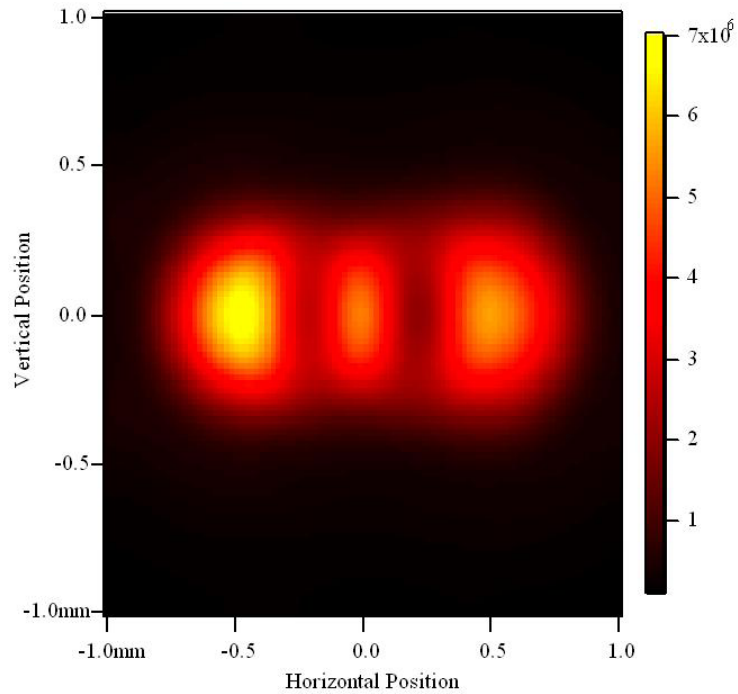


Figure 8.61 Calculated spatial distribution of the undulator radiation from a three-undulator cell with a missteering angle θ_{mis} of 10 μ rad, at 8.3 keV (slightly detuned from the 8.27 keV fundamental to higher energy), and with an electron beam emittance of 0.05 nm-rad, at 60 m from the undulator segments.

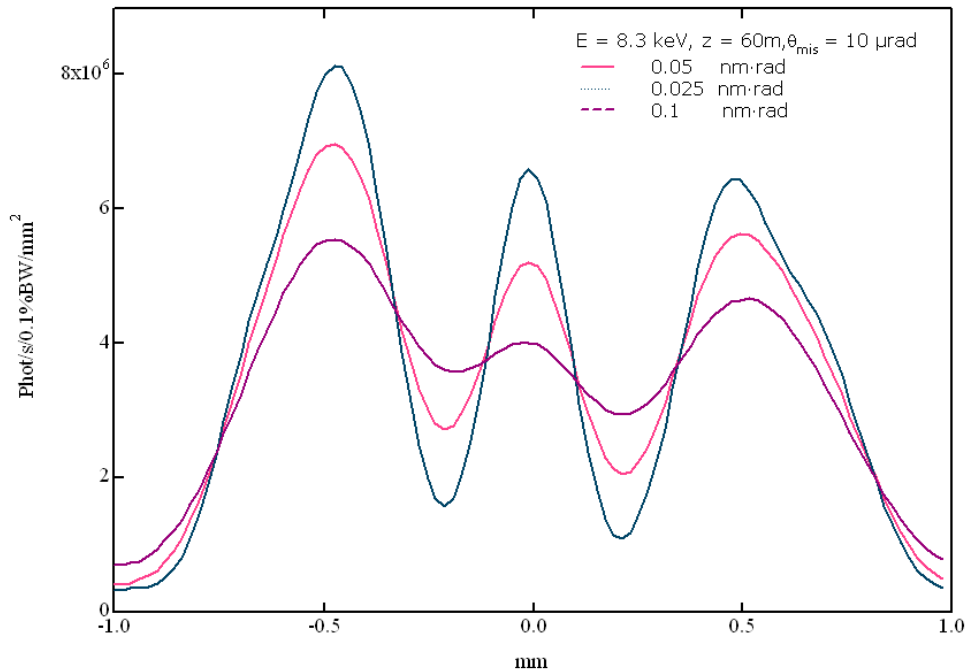


Figure 8.62 Calculated horizontal profiles of the undulator radiation from a three-segment cell with a missteering angle θ_{mis} of 10 μ rad, at 8.3 keV (slightly detuned from the 8.27 keV fundamental to higher energy), at 60 m from the undulator segments. Curves are shown for three different electron beam emittances: 0.05, 0.025, and 0.1 nm-rad.

8.14 References

- 1 R.J. Dejus, O.A. Shevchenko, and N.A. Vinokurov, *Nucl. Instrum. Methods A* **429** (1999) 225.
- 2 R.J. Dejus, O.A. Shevchenko, and N.A. Vinokurov, *Nucl. Instrum. Methods A* **445** (2000) 19.
- 3 K. Halbach, *J. de Physique* **44**, Colloque C1, supplement to #2 (1983), C1.
- 4 M. Xie, *IEEE Proceedings of the 1995 Particle Accelerator Conference, (IEEE, 1996)*, p. 183.
- 5 K.-J. Kim and M. Xie, *Nucl. Instrum. Methods A* **331** (1993) p. 359.
- 6 E. Gluskin, C. Benson, R. Dejus, P.K. Den Hartog, B.N. Deriy, O.A. Makarov, S.V. Milton, E.R. Moog, V.I. Ogurtsov, E.M. Trakhtenberg, K.E. Robinson, I.B. Vasserman, N.A. Vinokurov, and S. Xu, *Nucl. Instrum. Methods A* **429** (1999) p. 358.
- 7 P. Emma, R. Carr, and H.-D. Nuhn, *Nucl. Instrum. Methods A* **429** (1999) p. 407.
- 8 M. Xie, *Nucl. Instrum. Methods A* **445** (2000) p. 59.
- 9 J. Chavanne, P. Elleaume, and P. Van Vaerenbergh, "Partial Demagnetization of ID6 and Dose Measurements on Certain IDs," ESRF Machine Technical Note 1-1996/ID, (Jan. 1996).
- 10 P. Elleaume, personal communication.
- 11 T. Ikeda and S. Okuda, *Nucl. Instrum. Meth. Phys. Res. A* **407** (1998) 439.
- 12 R.D. Brown and J.R. Cost, *J. Appl. Phys.* **63**, 3537 (1988) and *IEEE Trans. Magn.* **25**, 3117 (1989).
- 13 Eckhart and Drake, "Analysis of Heat and Mass Transfer"
- 14 B. Rossi, High Energy Particles

- 15 K. Bane and P. Wilson, *Proceedings of the 11th Int. Conf. on High Energy Accelerators*, CERN (Birkhuser Verlag, Basel, 1980), p. 592.
- 16 A. Berman, "Vacuum Engineering, Calculations, Formulas, and Solved Exercises," Academic Press (1992).
- 17 D. Behne, "Outgassing Test Results from PEP-II Standard Straight Section Vacuum Chambers," (1997).
- 18 C. Forester, *et al.*, "Photon Stimulated Desorption (PSD) Measurements of Welded Copper Beam Chambers for the PEP-II Asymmetric B-Factory," *4th European Particle Accelerator Conference* (1994).
- 19 M. Sullivan, "A Method for Calculating Pressure Profiles in Vacuum Pipes," *PEP-II AP Note No. 6-94* (1994).
- 20 A. Chao, "Physics of Collective Beam Instabilities in High Energy Accelerators," John Wiley (1993).
- 21 K.L.F. Bane, M. Sands, "The Short-Range Resistive Wall Wakefields," Contributed to *Micro Bunches: A Workshop on the Production, Measurement and Applications of Short Bunches of Electrons and Positrons in Linacs and Storage Rings*, Upton, New York, September 28-30, 1995.
- 22 K. Bane and M. Sands, "Wakefields of Very Short Bunches in an Accelerating Cavity," *Particle Accelerators*, Vol. 25, pp. 73-05 (1990).
- 23 K. L. F. Bane, C. K. Ng, and A. W. Chao, *Estimate of the impedance due to wall surface roughness*, Report SLAC-PUB-7514, SLAC (1997).
- 24 G. V. Stupakov, *Phys. Rev. ST Accel. Beams* **1**, 064401 (1998).
- 25 G. Stupakov, R. E. Thomson, D. Walz, and R. Carr, *Phys. Rev. ST Accel. Beams* **2**, 060701 (1999).
- 26 A. Novokhatski and A. Mosnier, in *Proceedings of the 1997 Particle Accelerator Conference* (IEEE, Piscataway, NJ, 1997), pp. 1661–1663.
- 27 K. L. F. Bane and A. Novokhatskii, *The Resonator impedance model of surface roughness applied to the LCLS parameters*, Tech. Rep. SLAC-AP-117, SLAC (March 1999).
- 28 G. V. Stupakov, in T. Roser and S. Y. Zhang, eds., *Workshop on Instabilities of High Intensity Hadron Beams in Rings* (American Institute of Physics, New York, 1999), no. 496 in *AIP Conference Proceedings*, pp. 341–350.
- 29 D. J. Whitehouse, *Handbook of Surface Metrology* (IOP Publishing, 1994).
- 30 K. J. Stout, *Atlas of Machined Surfaces* (Chapman and Hall, 1990).
- 31 Chatard-Moulin and A. Papiernik, *IEEE Trans. Nucl. Sci.* **26**, 3523 (1979).
- 32 S. Krinsky, in W. S. Newman, ed., *Proc. International Conference on High-Energy Accelerators, Geneva, 1980*, CERN, European Lab. for Particle Physics (Birkhäuser Verlag, Basel, Switzerland, 1980), p. 576.
- 33 R. L. Warnock, *An Integro-Algebraic Equation for High Frequency Wake Fields in a Tube with Smoothly Varying Radius*, Report SLAC-PUB-6038, SLAC (1993).
- 34 K. L. F. Bane and G. V. Stupakov, *Wake of a rough beam wall surface*, Tech. Rep. SLAC-PUB-8023, SLAC (December 1998), presented at International Computational Accelerator Physics Conference (ICAP 98), Monterey, CA, 14-18 Sep 1998.
- 35 G. V. Stupakov, in *Physics of, and Science with, the X-ray Free-Electron Laser* (2000).
- 36 M. Dohlus, H. Schlarb, R. Wanzenberg, R. Lorenz, and T. Kamps, *Estimation of longitudinal wakefield effects in the TESLA-TTF FEL undulator beam pipe and diagnostic section*, Tech. Rep. DESY-TESLA-FEL-98-02, Deutsches Elektronen-Synchrotron, Hamburg, Germany (March 1998).

- 37 A. Novokhatsky, M. Timm, and T. Weiland, *Single bunch energy spread in the TESLA cryomodule*, Tech. Rep. DESY-TESLA-99-16, Deutsches Elektronen-Synchrotron, Hamburg, Germany (March 1999).
- 38 R. Tatchyn, *et al.*, "Research and Development Toward a 4.5-1.5 Å Linac Coherent Light Source (LCLS) at SLAC," *SLAC-PUB-95-6994* (1995).
- 39 D.E. Cullen *et al.*, "Tables and Graphs of Photon-Interaction Cross Sections from 10 eV to 100 GeV Derived from the LLNL Evaluated Photon Data Library (EPDL)," Lawrence Livermore National Laboratory, *UCRL-504000-Vol.6-Rev.4-Pt .A* (1989).
- 40 L.V. Keldysh, "Ionization in the field of a strong electromagnetic wave," *Soviet Physics JETP*, Vol. **20**, no. 5 (1965).
- 41 T.O. Raubenheimer, private communication (1997).
- 42 P. Chen, private communication (1997).
- 43 T.O. Raubenheimer and F. Zimmermann, "A Fast Beam-Ion Instability in Linear Accelerators and Storage Rings," *Physical Review E*, Vol. **52**, 5, pp. 5487-5498 and *SLAC-PUB-6740* (1995).
- 44 S.V. Milton, E. Gluskin, N.D. Arnold, C. Benson, W. Berg, S.G. Biedron, M. Borland, Y.-C. Chae, R.J. Dejus, P.K. Den Hartog, B. Deriy, M. Erdmann, Y.I. Eidelman, M.W. Hahne, Z. Huang, K.-J. Kim, J.W. Lewellen, Y. Li, A.H. Lumpkin, O. Makarov, E.R. Moog, A. Nassiri, V. Sajaev, R. Soliday, B.J. Tieman, E.M. Trakhtenberg, G. Travish, I.B. Vasserman, N.A. Vinokurov, G. Wiemerslage, and B.X. Yang, "Exponential Gain and Saturation of a Self-Amplified Spontaneous Emission Free-Electron Laser", *Science* **292**, 2037 (2001). Also published in Scienceexpress online at www.scienceexpress.org on 17 May 2001 as 10.1126/science.1059955.
- 45 S. Kim, "Calculating BPM Coefficients with Green's Reciprocation Theorem", Advanced Photon Source light source note LS-278, March 1999, URL
<http://www.aps.anl.gov/techpub/lsnotes/ls278/ls278.ps>.
- 46 R. Lorenz, "Cavity Beam Position Monitors", proceedings of the 1998 Beam Instrumentation Workshop, Stanford, USA, URL
<http://www.slac.stanford.edu/pubs/confproc/biw98/lorenz1.pdf>.
- 47 R.O. Hettel *et al.*, "Investigation of Beam Alignment Monitor Technologies for the LCLS FEL Undulator", proceedings of the 1998 Beam Instrumentation Workshop, Stanford, USA, URL:
<http://www.slac.stanford.edu/pubs/confproc/biw98/hettel.pdf>.
- 48 S. Smith, SLAC, private communication.
- 49 A.H. Lumpkin *et al.*, "Optical Techniques for Electron-Beam Characterizations on the APS SASE FEL Project", *Nucl. Instr. And Meth.* **A429**, 336 (1999).
- 50 J.-C. Denard *et al.*, "Experimental Diagnostics Using Optical Transition Radiation at CEBAF", *Proc. of the 1994 Beam Instrumentation Workshop*, *AIP Conf. Proc.* # 333, 224 (1995).
- 51 P. Catravas *et al.*, "Beam Profile Measurement at 30 GeV using Optical Transition Radiation", *Proc. of the 1999 Particle Accelerator Conference*, Vol. 3, 2111 (1999).
- 52 L. Wartski *et al.*, *IEEE Trans. Nucl. Sci.*, Vol **NS-22**, June 1975, p.15.
- 53 A. Fisher, "Instrumentation and Diagnostics for PEP-II", Proceedings of the 1998 Beam Instrumentation Workshop, Stanford, CA, (1998), URL:
<http://www.slac.stanford.edu/pubs/confproc/biw98/fisher1.pdf>.
- 54 A. Pietryla, "Design of the Cerenkov Radiation Detection System for the Advanced Photon Source Storage Ring", PAC01, June 18-22, 2001, Chicago, IL,

http://pacwebserver.fnal.gov/papers/Tuesday/AM_Poster/TPAH304.pdf

- 55 P. Emma, "Beam Based Alignment of Sector-1 of the SLC Linac", SLAC-PUB-5787, March 1992.
- 56 This technique was suggested by C. Adolphsen.
- 57 This misalignment component was suggested by C. Adolphsen.
- 58 LCLS Design Study Report, SLAC-R-521 and UC-414, Rev. Dec. 1998.
- 59 V. Shiltsev, "Space-Time Ground Diffusion: The ATL Law for Accelerators", 4th International Workshop on Accelerator Alignment (IWAA95), Tsukuba, Japan, 14-17 Nov. 1995.
- 60 R. Assmann, et. al., "Beamline Stability Measurements with a Stretched Wire System in the FFTB", 18th International Linac Conference (Linac 96), Geneva, Switzerland, 26-30 Aug. 1996.
- 61 P. Emma, "Electron Phase Slip in an Undulator with Dipole Field and BPM Errors", Proceedings of the 18th ICFA Beam Dynamics Workshop on Future Light Sources, "Physics of and Science with the X-Ray Free-Electron Laser", held 10-15 Sept. 2000, Arcidosso, Italy.
- 62 The diagnostics set up for the LCLS undulator line is, in principle, quite similar to that for the Low Energy Undulator Test Line (LEUTL) at the Advanced Photon Source [see E. Gluskin, et.al., "The magnetic and diagnostics systems for the APS SASE FEL", Nucl. Instrum. Methods A 429 (1999), pp.358-364]. The LEUTL diagnostics were developed for visible light, however, whereas the LCLS diagnostics are for X-rays.
- 63 O. Chubar and P. Elleaume, "Accurate and Efficient Computation of Synchrotron Radiation in the Near Field Region", *Proc. of the 1998 European Particle Accelerator Conference EPAC98*, 22-26 June 1998, p. 1177-1179.
- 64 W.-K.Lee, R. Iverson, P. Krejcik, D. McCormick, Summary of the diamond test with SLAC focused beam, October 2000.